JYU DISSERTATIONS 302

Visa Ruokolainen

Studying Factors that Contribute to Uncoating of Enteroviruses

UNIVERSITY OF JYVÄSKYLÄ
FACULTY OF MATHEMATICS
AND SCIENCE

JYU DISSERTATIONS 302

Visa Ruokolainen

Studying Factors that Contribute to Uncoating of Enteroviruses

Esitetään Jyväskylän yliopiston matemaattis-luonnontieteellisen tiedekunnan suostumuksella
julkisesti tarkastettavaksi lokakuun 30. päivänä 2020 kello 12.

Academic dissertation to be publicly discussed, by permission of
the Faculty of Mathematics and Science of the University of Jyväskylä,
on October 30, at 12 o'clock noon.

JYVÄSKYLÄN YLIOPISTO
UNIVERSITY OF JYVÄSKYLÄ

JYVÄSKYLÄ 2020

Editors
Varpu Marjomäki
Department of Biological and Environmental Science, University of Jyväskylä
Timo Hautala
Open Science Centre, University of Jyväskylä

.

Permanent link to this publication: http://urn.fi/URN:ISBN:978-951-39-8345-1

ISBN 978-951-39-8345-1 (PDF)
URN:ISBN:978-951-39-8345-1
ISSN 2489-9003

ABSTRACT

Ruokolainen, Visa
Studying factors that contribute to uncoating of enteroviruses
Jyväskylä: University of Jyväskylä, 2020, 61 p.
(JYU Dissertations
ISSN 2489-9003; 302)
ISBN 978-951-39-8345-1
Yhteenveto: Enterovirusten avautumiseen vaikuttavien tekijöiden tutkiminen
Diss.

Enteroviruses are small, non-enveloped viruses with a positive sense single stranded RNA genome. They cause different diseases in humans, usually with symptoms of common cold, but also more severe acute and chronic infections such as encephalitis and type 1 diabetes. Although the structure and infection pathway of many enteroviruses is rather well-known, many important details remain unresolved. For some enteroviruses receptor binding or low pH has been shown to convert them from an intact to an intermediate particle, which is needed for successful infection. However, B-species enteroviruses do not rely on the same factors e.g. low pH for efficient infection. Furthermore, the decisive factor releasing the enterovirus genome, is still unknown. Learning these missing factors is important for understanding the virus infection in more detail, that in turn provides basis for developing antiviral strategies. This study concentrates on two B-species enteroviruses, echovirus 1 and coxsackievirus A9, aiming to resolve if physiological factors, serum albumin and ion changes during the virus infection, trigger the virus transformation from intact to altered particles, and possibly further to genome release. We found that both factors contribute to formation of an intermediate particle of both viruses. Furthermore, specific changes in the ionic milieu led to the final genome release. The studied factors resulted in rather similar changes in their cryo-EM structures that are found for other enteroviruses primed using factors such as heat, low pH and receptor binding. However, we found that priming the coxsackievirus A9 using ion changes or albumin resulted in slightly different changes in virus capsid proteins: albumin resulted in more stable virus intermediate particle, whereas ions altered the virus capsid into a stage closer to the genome release. In the third part of this study, the aim was to develop a novel tool for live cell imaging of enterovirus entry and uncoating. We first solved the structure of intercalating RNA dye SYBR green II, modified it for better fluorescent properties and different binding capabilities, and finally verified its superiority in virus uncoating assays.

Keywords: Albumin; enterovirus uncoating; fluorescence measurement; genome release; intercalating fluorophore; intermediate particle; ions.

Visa Ruokolainen, University of Jyväskylä, Department of Biological and Environmental Science, P.O. Box 35, FI-40014 University of Jyväskylä, Finland

TIIVISTELMÄ

Ruokolainen, Visa
Enterovirusten avautumiseen vaikuttavien tekijöiden tutkiminen
Jyväskylä: Jyväskylän yliopisto, 2019, 61 s.
(JYU Dissertations
ISSN 2489-9003; 302)
ISBN 978-951-39-8345-1
Yhteenveto: Studying factors that contribute to uncoating of enteroviruses
Diss.

Enterovirukset ovat pieniä ja vaipattomia viruksia, joiden perimä on polaarisuudeltaan positiivista, yksijuosteista RNA:ta. Ne aiheuttavat sairauksia, joiden oireet ovat yleensä lieviä, mutta infektio voi johtaa myös vakavampiin akuutteihin ja kroonisiin tulehduksiin, kuten aivokuumeeseen ja ykköstyypin diabetekseen. Enteroviruksia on tutkittu pitkään ja esimerkiksi poliovirus on hyvin tunnettu enterovirus. Virusten rakenne ja infektion kulku tunnetaan pääpiirteissään tarkkaan, mutta silti moni tärkeä yksityiskohta on vielä selvittämättä. Reseptoriin sitoutuminen tai alhainen pH aloittaa useilla enteroviruksilla avautumisprosessin. Usea B-tyypin enterovirus ei kuitenkaan reagoi näihin tekijöihin ja molekyylejä, jotka vapauttavat perimän välimuotoisesta partikkelista, ei tunneta. Puuttuvien tekijöiden tunnistaminen on tärkeää, ei pelkästään virusten elinkaaren tuntemiseksi, vaan myös antiviraalihoitojen mahdollistamiseksi. Tämä väitöskirja keskittyy B-ryhmän enterovirusten, echovirus 1:n ja coxsackievirus A9:n avautumiseen johtavien tekijöiden määrittelyyn ja niiden aiheuttamien muutosten tutkimiseen. Löysimme kahden fysiologisen tekijän, albumiin ja infektion aikana muuttuvien ioniolosuhteiden, aiheuttavan muutoksen natiivista viruksesta välimuotoiseksi partikkeliksi. Lisäksi tietyt muutokset ioniolosuhteissa johtivat virusten perimän vapautumiseen. Tutkitut tekijät aiheuttivat viruksissa muutoksia, joita on havaittu myös toisten enterovirusten välimuotoisilla partikkeleilla. Lisäksi ionit ja albumiini saivat aikaan keskenään erilaisen muutoksen coxsackievirus A9:n rakenteessa siten, että albumiini aiheutti vakaamman välimuodon, kun taas ionit aiheuttivat lähempänä perimän vapautumista olevan muodon. Tutkimuksen kolmannessa osassa pyrimme kehittämään uusia elävien solujen infektiossa käytettäviä fluoresoivia merkkiaineita. Ratkaisimme paljon käytetyn kaupallisen SYBR green II:n merkkiaineen rakenteen, paransimme sen fluoresenssikykyä, kehitimme siitä eri kemiallisiin ryhmiin liitettäviä muotoja ja totesimme sen toimivuuden viruksen avautumiskokeissa.

Avainsanat: Albumiini; enterovirusten avautuminen; fluoresenssimittaus; ionit; interkaloituva fluorofori; perimän vapautuminen; viruksen välimuotopartikkeli.

Visa Ruokolainen, Jyväskylän yliopisto, Bio- ja ympäristötieteiden laitos PL 35, 40014 Jyväskylän yliopisto

Author

Visa Ruokolainen
Department of Biological and Environmental Science
P.O. Box 35
FI-40014 University of Jyväskylä
Finland
visa.ruokolainen@jyu.fi

Supervisor

Prof. Varpu Marjomäki, PhD
Department of Biological and Environmental Science
P.O. Box 35
FI-40014 University of Jyväskylä
Finland

Reviewers

Kari Airenne, PhD
Head of Vector Development
Kuopio Center for Gene and Cell Therapy
Microkatu 1
70210 Kuopio, Finland

Docent Kirsi Rilla, PhD
Institute of Biomedicine
University of Eastern Finland
P.O. Box 1627
FI-70211 Kuopio, Finland

Opponent

Docent Petri Susi, PhD
Institute of Biomedicine
University of Turku
Kiinamyllynkatu 10
20520 Turku, Finland

CONTENTS

LIST OF ORIGINAL PUBLICATIONS

The thesis is based on the following original papers, which will be referred to in the text by their Roman numerals I–III.

I Ruokolainen V.[1], Domanska A.[1], Laajala M., Pelliccia M., Butcher S. J., Marjomäki V. 2019. Extracellular Albumin and Endosomal Ions Prime Enterovirus Particles for Uncoating That Can Be Prevented by Fatty Acid Saturation. *Journal of Virology* 93 (17) e00599-19. Chosen for Spotlight. [1]Equal contribution

IA Ruokolainen V., Laajala M., Marjomäki V. 2020. Real-Time Fluorescence Measurement of Enterovirus Uncoating. *Bio-protocol* 10 (7) e3582. Invited publication.

II Domanska A.[1], Ruokolainen V.[1], Plavec Z., Löflund B., Soliymani R., Butcher S. J., Marjomäki V. Albumin and Cationic Ions Can Seperately Prime Coxsackievirus A9 for Uncoating. Manuscript. [1]Equal contribution

III Saarnio V. K., Salorinne K., Ruokolainen V., Nilsson J. R., Tero T-R., Oikarinen S., Wilhelmsson L. M., Lahtinen T. M., Marjomäki V. 2020. Development of Functionalized SYBR Green II Related Cyanine Dyes for Viral RNA Detection. *Dyes and Pigments*. 177, 108282.

RESPONSIBILITIES

Article I — Original idea of testing ions and different serum components on echovirus 1 intermediate particle formation was by Varpu Marjomäki. Planning the biochemical research was done by me, Mira Laajala and Varpu Marjomäki. Experiments were performed and analysed mainly by me with minor help of Maria Pelliccia and Mira Laajala. Electron density maps of the cryo-EM structures were done by me and the rest by Aušra Domanska. All authors participated in the writing process. I and Aušra Domanska contributed equally on the article.

Article IA — Invited protocol article was written by me with help of Mira Laajala and Varpu Marjomäki in planning and proofreading.

Aricle II — The original idea and design of the research was done by me, Varpu Marjomäki, Aušra Domanska and Sarah Butcher. The biochemical studies were planned by me and Varpu Marjomäki and performed and analysed by me. The cryo-EM was performed and analysed by Aušra Domanska, Zlatka Plavec and Benita Löflund. All the authors contributed in the writing. I and Aušra Domanska contributed equally on the article.

Article III — The original idea of design of the research was by Varpu Marjomäki, Ville Saarnio, Kirsi Salorinne and Tanja Lahtinen. The chemical synthesis was performed by Ville Saarnio and Kirsi Salorinne. I participated in designing the biological applications section and performed and analysed the experiments. All authors participated in writing.

1 INTRODUCTION

Enteroviruses (EVs) are a large group of viruses infecting animals and humans. Majority of the diseases caused by them are ones with symptoms of common cold. However, they are also associated with severe medical conditions, such as encephalitis, type I diabetes, celiac disease, asthma and allergies. The EVs are well-known, largely because of the members of C species EVs, the polioviruses (PVs). The earliest PV research articles can be found from the 1950´s and since many more have been published until today, even though the virus is nearly eradicated. Despite the long history of EV research many important details in the infection remains to be discovered, especially for some not so well-known EVs. For successful infection viruses need to find the right pathway inside cells. This pathway, starting with a binding to the virus specific receptor on a cell surface, has to include all the needed factors that leads the virus to the right place at the right time, resulting in a successful genome release. After releasing the genome at the right spatiotemporal timing, the virus replication, aiming to formation of progeny virus particles, can start. Even though one of the most important moments in a "life of a virus" takes place in the early infection, the definitive factors leading to the uncoating of many viruses remains to be resolved. This fundamental information about the virus lifecycle is crucial in understanding the infection in whole and designing antiviral strategies.

This thesis concentrates on the early infection phase of two of enterovirus B species viruses (EV-Bs), echovirus 1 (E1) and coxsackievirus A9 (CVA9). More exactly, we studied the factors that contribute to the virus stability and formation of metastable intermediate form of the virus ready for infection and genome release. We found that an extracellular factor albumin, abundant fatty-acid carrying protein in serum, can prime EVs for uncoating in a manner that is dependent on the albumin concentration. This priming can be prevented by fatty acids, that are found inside an intact virus capsid and is known to stabilize the capsid structure. Furthermore, we found that the changes in ion concentrations potentially occurring during the endocytosis of the virus, pushes the virus for genome release. In addition, we produced and characterized novel fluorescent probes, that can be utilized in the future in imaging the virus entry and genome uncoating in live cells.

2 REVIEW OF THE LITERATURE

2.1 Enteroviruses

Picornaviruses are very diverse and rapidly growing virus family causing wide range of diseases in a wide range of hosts (Zell 2018). Best studied picornaviruses are the large group of EVs (Tuthill *et al.* 2010). EVs include probably the best-known and almost eradicated polioviruses (PVs) causing poliomyelitis, as well as EV 71 causing hand, foot and mouth disease, and human rhinoviruses (HRVs) causing common colds, to mention only a few. According to the International Committee on Taxonomy of Viruses, in 2019, the EVs consisted 15 different species, EVs A-L and HRV A-C including more than 300 virus types.

Although the diseases and symptoms caused by the viral infections, and aim to prevent or cure those, are the main driving force of virus research, one has to appreciate also the vast amount of biological knowledge that has evolved from the virus research. Culture of human cells in 1955, development of recombinant DNA molecule in 1972, discovery of RNA splicing in 1977, discovery of nuclear localization signal in 1984 and discovery of gene silencing by double-stranded RNA in 1998 are only few examples of the contribution of virus research to the cell biology (Enquist and Editors of the Journal of Virology 2009). Also, the term "endosome", a very relevant concept in this PhD thesis, was introduced by a world-famous Finnish virus researcher Ari Helenius with his coworkers in 1983 (Helenius *et al.* 1983) emphasizing, that the viruses have been very useful tool in studying cellular aspects of endocytosis and many membrane processes (Helenius 2020). Moreover, many concepts in the field of molecular virology originates from the PV research (Baggen *et al.* 2018).

2.1.1 Critical steps in EV infection

Virus lifecycle has many critical steps that has to be accomplished for successful infection. One of the most important virus-cell-interaction, the receptor binding, takes place at the plasma membrane (Helenius 2018). In addition to the fact that the cell attachment mostly defines the virus tropism, this interaction can result

in complex signalling events inside cells leading to virus entry, and also changes in the virus capsid leading to genome release (Schneider-Schaulies 2000, Yamauchi and Greber 2016). The receptor binding does not always lead to a successful infection, as many other factors contribute on the infection route, however it is obvious, that without such binding a successful infection is highly unlikely (Helenius 2018).

Many of the needed steps depend on the virus type. For example, enveloped viruses use different kind of entry mechanisms than non-enveloped viruses, and replication of viral DNA genome takes place inside the cell nucleus while RNA genome is replicated in the cell cytoplasm. Because of these differences, I will next concentrate on the EVs, that all are about 30 nm in size, non-enveloped viruses, with positive sense single strand 7-7.5 kb RNA genome. Virus capsid, made from 60 copies of each capsid protein VP1-4, protects the genome inside. General scheme of EV replication is presented in more detail in Figure 1. First, the virus has to find a host cell that provides a suitable anchoring point, a receptor, that the virus capsid proteins attach to with very high specificity. Next, the entry into cells, in a case of these non-enveloped EVs, happens using endocytosis that leads into different types of endosomes, depending on the virus. From these endosomes, the virus has to uncoat and release its genome into the cytoplasm of the cell, where the genome serves as a messenger RNA starting viral protein synthesis, and a template for RNA-dependent RNA replication. Once the needed viral proteins are synthesized and genome replicated, new progeny viruses are assembled before egress from the cell.

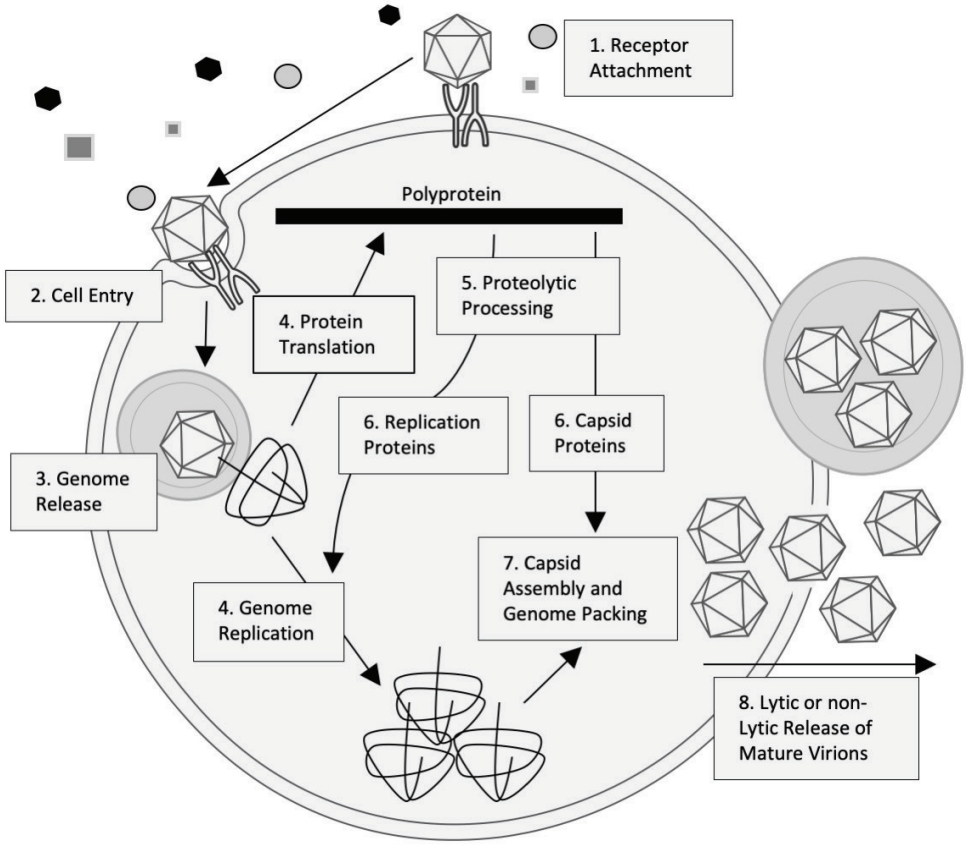

FIGURE 1 Overview of the EV infection cycle. The image was modified from a review by Baggen *et al*. 2018. On the cell surface the virus attaches to its specific receptor (1). Different virus stability affecting factors may reside on the extracellular space and be potentially endocytosed with the virus. The virus internalises the cell by triggering a specific endocytic route, depending on the virus-receptor interaction (2). The endocytosed virus uncoats and releases the genome when still inside the endosomal vesicle (3). The empty capsids presumably remain inside the vesicles and are ultimately degraded. After getting the genome into the cellular cytoplasm, the genome replication and protein translation can begin (4). These events occur at the same time, as the genome is used as a messenger RNA by cellular ribosomes, and also being replicated by the viral RNA-dependent RNA polymerase as soon as the first viral proteins are translated. Starting from only the successfully released viral genomes, many more are replicated and viral proteins translated that then provide a source and tools for even further replication and translation, as the infection proceeds. The viral genome is first translated into one polyprotein, which is then co- and post-translationally cleaved into individual viral proteins (5). The mature viral non-structural proteins participate in the genome replication, as well as in other tasks needed for the virus infection, while the structural proteins accumulate into the replication organelle (6). In the replication organelle, the structural proteins start to assemble into protomers and pentamers which, with the replicated genomes, assemble into new progeny virions (7). The new virions are released in lytic manner by killing the cell, or in non-lytic manner via exosomes (8). Figure was made using images of Smart Servier Medical Art (smart.servier.com).

The three first steps, attachment, entry and genome uncoating are infection determining factors before the virus replication can start in the first place. Thus, they are very attractive targets for different antiviral strategies as well as important research topics to fully understand the virus life cycle.

2.1.2 Cell attachment, entry and genome uncoating of EVs

As the EVs are a large group of viruses, they also have diverse ways for cellular attachment and entry, as well as for uncoating. Many of the steps are well known, and yet many important details remain to be resolved (Baggen *et al.* 2018). EVs use wide array of cellular molecules as receptors. For example, PVs use poliovirus receptor (Mendelsohn *et al.* 1989), major group HRVs use intercellular adhesion molecule-1 (Greve *et al.* 1989, Staunton *et al.* 1989), minor group HRVs use low density lipoprotein receptor family proteins (Hofer *et al.* 1994) and EV A71 as well as another hand, foot and mouth disease causing virus, coxsackievirus A-16, use mainly scavenger receptor class B, member 2 (Yamayoshi *et al.* 2009). From the EV-Bs, coxsackieviruses B1, B3 and B5 use decay accelerating factor for cell attachment (Shafren *et al.* 1995) and subsequently coxsackie and adenovirus receptor for cell entry, as does also all the other coxsackie B-viruses (Bergelson *et al.* 1997). Important group of EV receptors are also integrins (Merilahti *et al.* 2012). E1 use α2β1 integrin for cell attachment (Bergelson *et al.* 1992), whereas CVA9 is shown to attach both αvβ3 and αvβ6 via an RGD motif (Roivainen *et al.* 1994, Williams *et al.* 2004).

In addition to mere cell attachment, the receptor binding usually provides also other signals for both the virus and the cell. For example, the receptor binding can induce alterations in virus capsid protein conformation and stability, as well as cellular signalling leading to endocytosis (Tuthill *et al.* 2010). For PV, receptor binding leads to virus priming from an intact into an intermediate particle (De Sena and Mandel 1977) and internalization into the cell using noncanonical endosomal pathway (Brandenburg *et al.* 2007). The virus stays attached to the vesicle membrane and translocate the genome to cell cytoplasm from the capsid through a membrane pore formed by the capsid proteins (Groppelli *et al.* 2017).

For both PVs and major group HRVs, as well as many other EVs, the receptor binds into a groove that circulates around the five-fold axis of the virus, usually called as the canyon (Tuthill *et al.* 2010) and expels the capsid stabilizing lipid factor (Rossmann *et al.* 2002, Wang *et al.* 2012). Nevertheless, this binding does not lead to similar entry and uncoating events for HRVs and PVs. Depending on the HRV serotype, binding to the ICAM-1 may cause some alterations in the capsid stability, but also a low pH is needed for the genome release (Fuchs and Blaas 2010). For minor group HRVs the receptor does not bind the canyon and the binding does not alter the capsid stability (Tuthill *et al.* 2010). For these viruses a low pH is found the be the key factor leading to the virus uncoating (Prchla *et al.* 1994). Recently, a neonatal Fc receptor (FcRn) was found to act as a pan-echovirus receptor (Morosky *et al.* 2019). Morover, the FcRn was found to uncoat echovirus 6 in acidic condition, and knocking out the protein blocked

the infection of 14 different EV-B serotypes including E1 and CVA9 (Zhao *et al.* 2019).

The route for early infection of PVs and HRVs are amongst the most detailed described for all the EVs, and the pathways are known in much more detail than described here. In fact, it is often extrapolated, that EV attachment, entry, priming and uncoating are a result of a receptor binding (as with PVs) or lowered pH (as with HRVs). However, we now begin to appreciate that this is not always the case (Marjomaki *et al.* 2015).

2.2 Entry and uncoating of the EV-Bs

Amongst the EVs, the EV-Bs consists over 30 serotypes of echoviruses, coxsackievirus A9 and B1-6 and over 20 serotypes of enterovirus Bs (Marjomaki *et al.* 2015). The primary infection of EV-Bs takes place in the fecal-oral route. Normally, they cause a number of infections with symptoms seen with common cold (Marjomaki *et al.* 2015). However, they are also associated with more severe secondary infections such as myocardial infarction (Roivainen *et al.* 1998, Roivainen 1999, Marjomaki *et al.* 2015) and type I diabetes (Hober and Sauter 2010, Hyoty 2016). Especially the coxsackievirus B1 has been shown to participate in beta-cell autoimmunity leading to type 1 diabetes (Laitinen *et al.* 2014). Recently, EV-B infection was also associated with the onset of coeliac disease (Kahrs *et al.* 2019)

Within the EV-Bs, some virus serotypes remain stable in a presence of the factors that typically triggers the conversion of intact PVs and HRVs into intermediate particles, namely receptor binding and low pH. For example, E1 and CVA9 remain stable when bound to the receptor and their uncoating takes place in neutral pH endosomal structures after uptake (Xing *et al.* 2004, Karjalainen *et al.* 2011, Shakeel *et al.* 2013, Huttunen *et al.* 2014). In fact, E1 is rather stabilized when globally bound with the binding receptor I-domain (Myllynen *et al.* 2016). As the knockout of FcRn was shown to block also the infection of these two acid stabile viruses (Zhao *et al.* 2019), the mechanism behind this action remains to be better studied. The overall scheme of EV-Bs early infection is presented in Figure 2.

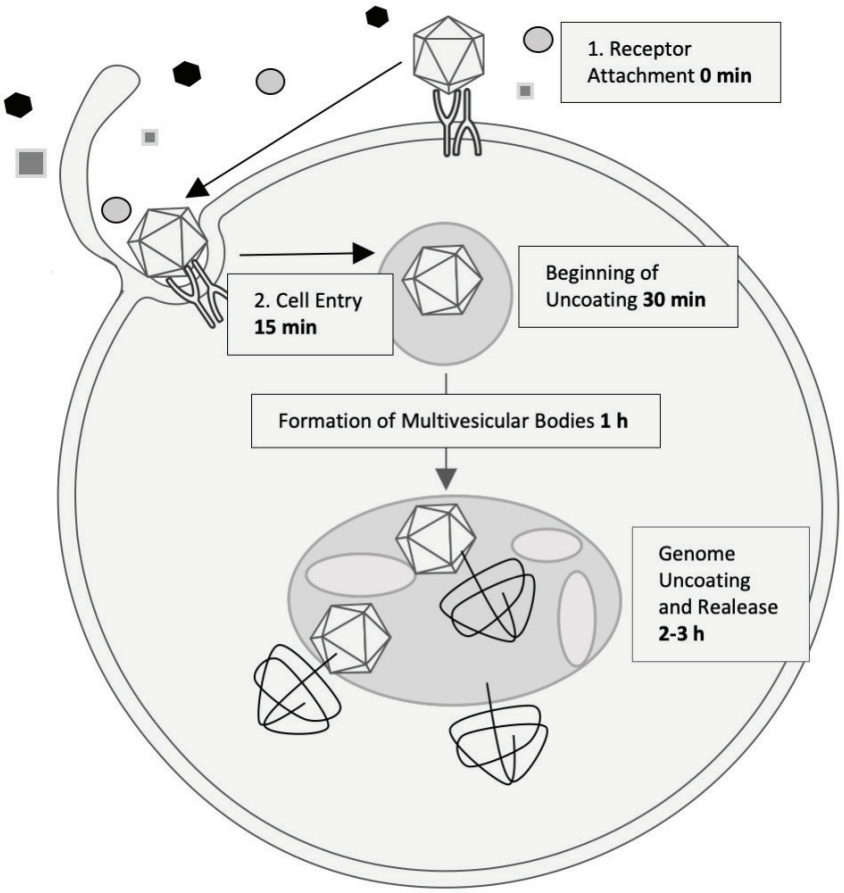

FIGURE 2 Early infection of EV-Bs. The image was modified from a review by Marjomäki *et al.* 2015. There can also be other modes of entry in the EV-Bs, but E1 and CVA9 are shown to follow the route and schedule provided in here. The virus attaches to the receptor on the cell surface (1). The binding causes receptor clustering with series of other events leading to macropinocytic entry of the virus inside endosomes within 15 minutes from the receptor binding (2). The uncoating inside the neutral pH endosomal vesicles starts as early as 30 post infections, while the majority of the viral genome is released after 2 hours of infection. In between the early uncoating and final RNA release from the endosomes, the virus containing endosomes transform into multivesicular bodies (MVBs). The exact spatiotemporal details of the genome release remain unclear. However, the genome needs to access the cytoplasm before starting the replication and translation. Figure was made using images of Smart Servier Medical Art (smart.servier.com)

Entry of E1 initiates with binding to a non-active form of $\alpha_2\beta_1$ integrin (Jokinen *et al.* 2010). The binding cause receptors to cluster on a cholesterol dependent lipid raft domains (Upla *et al.* 2004, Siljamaki *et al.* 2013). The virus enters with the receptor (Marjomaki *et al.* 2002) into novel, nonrecycling endosomal pathway (Rintanen *et al.* 2012) that leads to neutral MVBs (Karjalainen *et al.* 2011). After accumulation into these structures, the virus uncoats and releases its genome into the cytoplasm to start viral replication (Marjomaki *et al.* 2002, Karjalainen *et al.* 2008).

In the case of CVA9, the binding to the receptor, $\alpha_v\beta_3$ or $\alpha_v\beta_6$ integrin, leads the virus to similar neutral MVBs (Huttunen *et al.* 2014). The caveolin and clathrin independent entry is mediated by Arf6, dynamin and β2-microglobulin (Heikkila *et al.* 2010). While binding $\alpha_v\beta_6$ with higher affinity than $\alpha_v\beta_3$, the virus is able to utilize several infection routes and receptors for a wider tropism (Heikkila *et al.* 2009). The virus uncoating initiates around 30 minutes post infection, while majority of the genome release occurs around 2 hours when the virus still resides inside the MVBs (Huttunen *et al.* 2014).

Both of these viruses trigger a unique route for endocytosis. Usually, the endosomal sorting complex required for transport (ESCRT) facilitated formation of MVBs have been connected with low pH degradation and exocytosis (Frankel and Audhya 2018). Interestingly, the formation of E1 and CVA9 induced MVBs also require the ESCRT machinery, but do not lead to lysosomal degradation pathway (Karjalainen *et al.* 2011, Huttunen *et al.* 2014). Although, the route for entry and the site of uncoating are defined for E1 and CVA9, the definitive factor(s) leading to the uncoating of the genome and its egress to the cytoplasm remains to be defined.

2.2.1 Albumin

EVs cause severe illnesses mainly due to the secondary infections in organs, such as the pancreas and the heart. To get to the organs, they need to travel from the site of primary infection to the site of the secondary infection through the circulatory system, i.e., through the blood and interstitial fluids. Because of this it is highly relevant to consider the encountered molecules and conditions, and their effect on the viruses.

Albumin is an abundant protein in serum binding and transporting variety molecules from natural ligands to nanoparticles in living organisms (Karimi *et al.* 2016). Furthermore, albumin carries and provides free fatty acids to cells as an important source of different metabolic reactions (van der Vusse, G J 2009). Importantly, albumin has been shown to directly interact with cell surface albumin binding sites to deliver the cargo inside cells (Trigatti and Gerber 1995) and it has a very high affinity for the same fatty acids that are found inside the pockets of the EVs (Smyth *et al.* 2003, van der Vusse, G J 2009). Intriguingly, the recycling of endocytosed albumin back to the cell surface is very closely connected to the recently found pan-enterovirus uncoating receptor, the FcRn (Toh *et al.* 2019, Morosky *et al.* 2019, Zhao *et al.* 2019). As the uncoating of CVA9 or E1 is not triggered by acidity as with echovirus 6, the explanation for the infection blockage by FcRn knockout could possibly be related to the connection of FcRn and albumin recycling.

First clues of albumin interacting with, or influencing the infectivity of, EVs were provided by Ward and co-workers approximately 20 years ago (Ward *et al.* 1999, Ward *et al.* 2000). They showed that, during infection, albumin could inhibit the uncoating of echovirus 7 (Ward *et al.* 1999). In addition, fatty acid free bovine serum albumin (faf-BSA) primed echovirus 12 from intact into altered particles *in vitro*, while normal bovine serum albumin (BSA) was not

found to have similar effect (Ward *et al.* 2000). However, after these early reports, nothing more was since published on albumin and EVs.

2.2.2 Ions

Another interesting factor in the lifecycle of viruses is the surrounding ionic milieu. The EVs are assembled in the cytoplasm of a cell, that have a specific ionic environment (Fig. 3). After egress from the cells, they enter very different ionic environment of the extracellular space (Fig. 3), where they need to stay stable to be able to reach the site of the secondary infection. During early infection, whether in the primary or the secondary infection site, the virus meets again a changing ionic milieu, the one existing inside the endosomes. Whether the milieu is acidic or not, depends on the entry route of the virus, and the pH (H^+ concentration) probably also affects the concentration of other ions. The ionic conditions inside the endosomal vesicles are hard to define, not only because of wide variety of different kinds of endosomes, but also because of the small size of the vesicles. However, some measurements have been made from the acidifying endosomal route, and those are provided in the Figure 3.

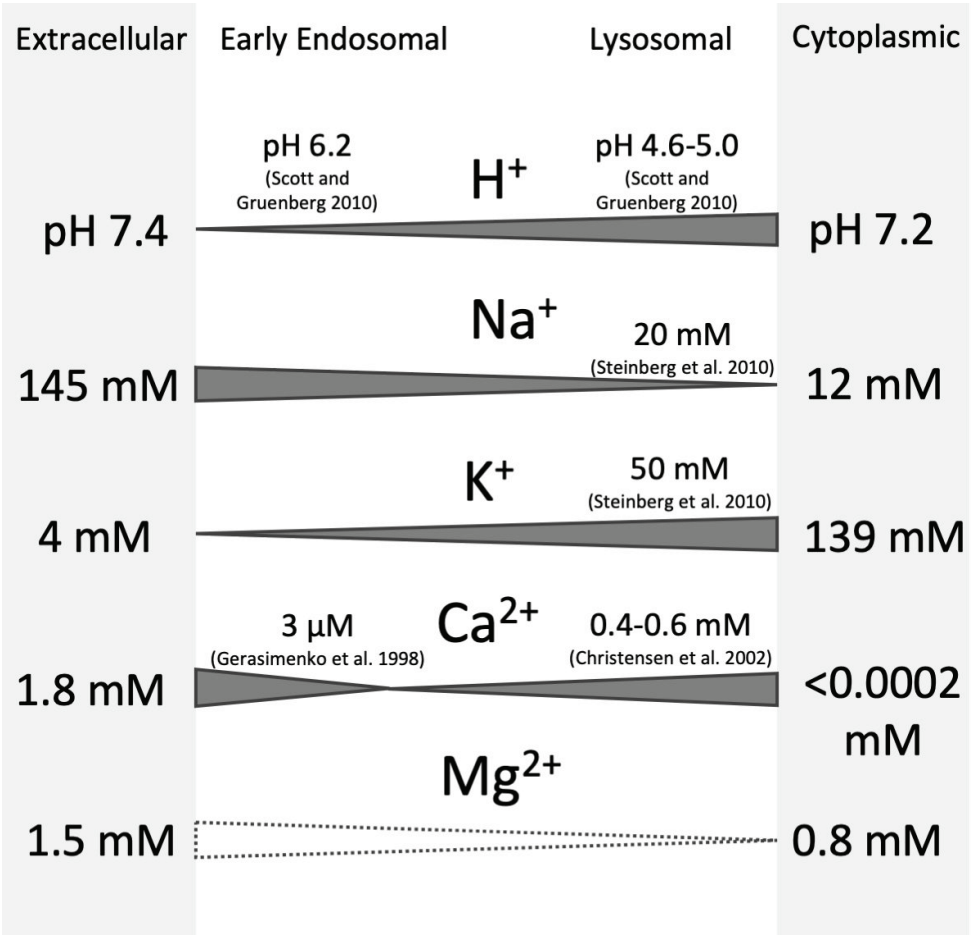

FIGURE 3 The pH and ion concentrations in extracellular space, cytoplasm and endosomes. The image was modified from a review by Scott and Gruenberg 2010. The concentration of sodium and potassium change drastically between the extracellular and intracellular space. The measured values of these ions inside lysosomes has moved towards the cytoplasmic values from the extracellular conditions, that is the source of ions for the forming endosomes during uptake. The concentration of calcium is shown to quickly decrease close to the cytoplasmic values and then, while the vesicle matures into lysosome, increase again closer to the extracellular value. Measurements about the concentrations of magnesium has not been made according to my best knowledge.

Endosomes are a heterogenous population of vesicles. New vesicles are forming, existing vesicles are moving between cellular compartments, fusing and forming intraluminal vesicles. The intraluminal conditions of the vesicles vary significantly depending on the type of the vesicle (Scott and Gruenberg 2011). Studies made so far have described the ion conditions in the acidifying endosomal route (Gerasimenko *et al.* 1998, Christensen *et al.* 2002, Sonawane *et al.* 2002, Hara-Chikuma *et al.* 2005, Steinberg *et al.* 2010). However, as it has become clear that ion flux in and out of endosomal vesicles is about more than just adjusting the pH (Scott and Gruenberg 2011), the knowledge about luminal conditions in non-acidifying endosomes remains to be better characterized. Specific

microdomains and microenvironments within an endosome may steeply affect the composition of the membrane proteins, such as ion channels or pumps, or intraluminal conditions, and a change of only few ions has profound effect in such a small volume (Raiborg *et al.* 2002, Scott and Gruenberg 2011). Besides the information provided for PV, there is very little information about into which compartment viruses actually release the genome. In principle, the release can happen into the lumen of the endosomal vesicle, or straight to the cytoplasm as shown with PV (Groppelli *et al.* 2017). In a case of E1 and CVA9, that accumulate in MVBs before the genome release, there is also an option that the genome is ejected into intraluminal vesicle. Recently, more knowledge has accumulated of the endo-lysosomal intraluminal vesicles and their intraluminal milieu (Gruenberg 2020). Different populations of intraluminal vesicles are found, both ESCRT dependent and ESCRT independent (Babst 2011). Furthermore, even the vesicles that form into acidic MVBs are found to remain neutral up to 20 minutes after formation (Falguieres *et al.* 2008).

Already early on, low ionic strength and divalent cations were found to have a profound effect on several EVs. Low ion conditions detached VP4 of coxsackievirus A13 and, as a result, the cellular adsorption of the virus was blocked (Cords *et al.* 1975). The attachment of HRV 2 to the cells was found to be inhibited by chelating divalent cations from the infection medium, and it was suggested, that the receptor binding required divalent cations (Lonberg-Holm and Korant 1972, Noble-Harvey and Lonberg-Holm 1974). Furthermore, low ionic conditions were shown to convert PV type 2 into an altered particle (Lonberg-Holm *et al.* 1976) and the process appeared to be enhanced when serum was present. PV was also found to convert into an empty particle in very low salt conditions, and could be rescued to an altered particle with 2 mM $CaCl_2$ (Wetz and Kucinski 1991). Divalent cations, Ca^{2+} and Mg^{2+}, were shown to stabilize capsids of other plant and animal viruses as well (Pfeiffer *et al.* 1976, Hull 1978, Sherman *et al.* 2006). The number of Ca^{2+} and Mg^{2+} ions in a red clover necrotic mosaic virus was determined and moreover, it was shown, that their depletion resulted in significant reorganisation of the capsid, including 11-13 Å channels extending through the capsid (Sherman *et al.* 2006). On the other hand, it has also been shown, that while calcium enhanced the cell binding of hepatitis A-virus, it also destabilized the virus capsid (Bishop and Anderson 1997).

There are further observations, where a specific change in ions is needed for virus infection in cells. Influenza A-virus, an enveloped virus, was shown to require both lowered pH and elevated potassium concentration, in the respective order, for efficient virus priming before uncoating and genome release (Stauffer *et al.* 2014). Also, another enveloped virus, bunyavirus, was recently observed to require high potassium concentration inside endosomes for efficient and timely genome release (Hover *et al.* 2018). The elevated potassium concentration was shown to substantially alter the conformation of the virus spike protein allowing it to interact with the endosomal membrane (Punch *et al.* 2018). The increase in potassium concentration inside endosomes was dependent on a normal presence of cellular cholesterol (Charlton *et al.* 2019). Interestingly, the infection of many EV-Bs are also found to rely on the presence of cho-

lesterol (Marjomaki *et al.* 2015). For example, the endosomes used for internalization by E1 are found to be rich in cholesterol, and interference in its normal amount and localization halted the infection inside the internalizing endosomes (Siljamaki *et al.* 2013).

Already more than 40 years ago, Pfeiffer and co-workers suggested, that Mg^{2+} affected not only the virus capsid, but also the localization of viral RNA genome inside it (Pfeiffer *et al.* 1976). Indeed, today the ions are known to play a major role in RNA structure and stability (Draper 2004). Ions can stabilize the RNA structure in two different equally important ways. Either by directly binding within the structure, or freely moving in close proximity of the structure but not being connected to it (Draper 2004). Especially potassium and magnesium are important RNA stabilizing ions that can both bind and surround the structure (Draper 2004).

2.3 Cryo-EM and virus structure

Cryo-EM and particle reconstruction has gone through big developments over the past ten years through advances in computation and the used detectors, and it is increasingly popular in determining particle structure at molecular resolution (Benjin and Ling 2020). Also, the interest of EV capsid opening and reconstruction of intermediate particles has grown and a vast number of new structures has been discovered in the recent years (Pickl-Herk *et al.* 2013, Shingler *et al.* 2013, Organtini *et al.* 2014, Butan *et al.* 2014, Strauss *et al.* 2015, Ren *et al.* 2015, Lee *et al.* 2016, Strauss *et al.* 2017, Liu *et al.* 2018, Buchta *et al.* 2019). Furthermore, the resolution of Cryo-EM technique has improved from approximately 10 Å down to around 2-3 Å over the last one and half decades (Bubeck *et al.* 2005, Liu *et al.* 2018), thus providing more accurate details.

The challenge in pushing the resolution boundaries in Cryo-EM is that, while the rigid areas are well-defined and seen in more detail, at the same time, the more flexible areas provide much lower resolution as the structure is a result of high amount of averaging (Benjin and Ling 2020). Sometimes the areas that are more motile or flexible, and perhaps more biologically active and thus offer a lower resolution structure, are the ones of most interest (personal communication with Sarah Butcher, University of Helsinki). Another challenge in a perspective of virus research is that in sample preparation, the usual way is to treat the virus containing sample in a solution containing the molecules or other conditions of interest. In this way, the effect to the virus is global, while in cell context the effect might be local. For example, receptor binding on a cell surface occurs asymmetrically on one side of the capsid only resulting in a different kind of structural changes than when stimulated globally with the receptor (Lee *et al.* 2016). The interaction of ions with the capsid occurs around the virus while the interaction with albumin could in principle be global or local at different stages.

2.3.1 Different EV forms

During its lifecycle, the EVs may be found in three different forms: mature intact particle sedimenting at approximately 160S, altered A-particle sedimenting at approximately 135S and empty particle, which has released their genome, sedimenting at approximately 80S (Tuthill *et al.* 2010). The A-particles, also called 135 S- or intermediate particle, have features that are thought to be more or less universal for all EVs (Tuthill *et al.* 2010). These particles have lost all or part of their VP4 capsid proteins (Crowell and Philipson 1971, Fricks and Hogle 1990, Greve *et al.* 1991, Hewat and Blaas 2004). Also, the VP1 amino terminus, normally residing on the capsid inner surface, has externalised, thus changing the virus from hydrophilic to more hydrophobic (Fricks and Hogle 1990, Danthi *et al.* 2003).

The first found A-particles of coxsackievirus B3 (CVB3) and PV were observed to have lost their infectivity (Crowell and Philipson 1971, Lonberg-Holm *et al.* 1975). A-particles were found to form during infection in cells (Lonberg-Holm *et al.* 1975, Fricks and Hogle 1990) and thus were suggested to be an important intermediate form of virus, needed for successful infection before releasing the genome and turning into 80S empty particle (Fricks and Hogle 1990, Curry *et al.* 1996, Huang *et al.* 2000). Later, the PV A-particle was found to be infectious, although 3-5 orders of magnitude less than the native virus (Curry *et al.* 1996). The low infectivity was due to inefficient binding to cells (Huang *et al.* 2000).

A different kind of intermediate EV particle was detected in our lab (Myllynen *et al.* 2016). Importantly, this intermediate E1 particle was found from cells during infection and it contained all the VP4 (Myllynen *et al.* 2016). Furthermore, the particle was found to be stable, capable for receptor binding and nearly as infective as the native virus (Myllynen *et al.* 2016). Thus, it was observed to be different in many aspects from the "classical" A-particle.

2.3.2 Changes in the capsid structure of intermediate EV particle

Different means to convert intact particles into 135S *in vitro* were found in the 1990`s. These include receptor binding for PV and HRV (Kaplan *et al.* 1990, Casasnovas and Springer 1994), low pH for HRV (Casasnovas and Springer 1994, Prchla *et al.* 1994), and high temperatures for PV (Curry *et al.* 1996). In addition, BSA was found to convert intact EV 12 into 135S (Ward *et al.* 2000). A-particles were also found to exist as contaminants in purified virus preparation of intact coxsackievirus A16 (Ren *et al.* 2013).

Until now, a number of high-resolution X-ray or cryo-EM structures has been defined for A-particles of different EVs using the means described above (Bubeck *et al.* 2005, Pickl-Herk *et al.* 2013, Ren *et al.* 2013, Shingler *et al.* 2013, Butan *et al.* 2014, Organtini *et al.* 2014, Strauss *et al.* 2015, Lee *et al.* 2016, Liu *et al.* 2018, Buchta *et al.* 2019). The resolved structures revealed many detailed characteristics for the A-particles that include, but are not limited to, about 4% expansion of the virus particle (Ren *et al.* 2013, Butan *et al.* 2014, Organtini *et al.* 2014, Liu *et al.* 2018), externalised VP1 N-terminus (Bubeck *et al.* 2005, Ren *et al.* 2013,

Shingler *et al.* 2013, Butan *et al.* 2014, Liu *et al.* 2018), loss of pocket factor (Ren *et al.* 2013, Strauss *et al.* 2015), rearrangements of the capsid proteins resulting in changed contacts with the genome (Pickl-Herk *et al.* 2013, Shingler *et al.* 2013, Organtini *et al.* 2014, Strauss *et al.* 2015) and formation of enlarged openings at the 2-fold axis through which the genome is suggested to exit (Ren *et al.* 2013, Shingler *et al.* 2013, Organtini *et al.* 2014, Liu *et al.* 2018). Furthermore, the area occupied by VP4 in intact virus particles became disordered in A-particle structures and thus impossible to assign amino acids. Because of this, the amount of VP4 within the A-particle capsid was found to decrease using other approaches (Ren *et al.* 2013, Liu *et al.* 2018). However, CVB3 binding locally into nanodisc attached coxsackie and adenovirus receptor resulted in a different kind of A-particle, where the capsid expansion was also local (Lee *et al.* 2016). In addition, the pocket factor and disordered VP4 and VP1 N-terminus could also be modelled, although their density was weaker than other parts of the capsid (Lee *et al.* 2016). Treating echovirus 18 and 30 in low pH produced more radical changes as whole pentamers expelled from the virions in a progress leading to genome release (Buchta *et al.* 2019).

Originally the different A-particles were thought to be nearly identical and the heated ones being indistinguishable from the ones that were produced by receptor binding (Tuthill *et al.* 2010). The described A-particles do share many of the A-particle hallmarks mentioned above, but with increasing amount of structures and improved resolution it has become clear that they actually differ in several details. This might not only be because of different studied viral strains, but also because of different strategies to generate altered particles. Indeed, different PV A-particles were detected depending on the method used to prime the particles (Shah et al 2020). Furthermore, a single virus serotype has several different intermediate forms even if induced in a same way, some more stable than others, as shown with EV D68 and PV (Strauss *et al.* 2017, Liu *et al.* 2018).

2.4 Observing of virus opening *in vitro* and infection *in vivo*

Virus opening can be followed with and without the cell context. Both ways need different methods, as well as powerful and well-defined virus labelling. The observed events are small, such as formation of nanoscale opening in the virus capsid, and thus need careful analysis to determine. In cell context, the method of choice for live-cell imaging of virus infection is light microscopy with its numerous applications (Witte *et al.* 2018). When studying different factors affecting the EVs without the cell context, there are many different methods to choose from. However, regardless of the method, it is important to isolate different variables to determine their individual effect. Furthermore, one needs to be able to distinguish between the different virus forms: 80S/empty, 135S/intermediate and 160S/intact.

2.4.1 Measuring and detecting the virus opening *in vitro*

The state of the virus capsid can be observed by many means. One of the first and still often used methods was to detect the sedimentation of a radiolabelled virus after a gradient centrifugation (Fenwick and Cooper 1962). Transmission electron microscopy (TEM) is also widely applied for this purpose and for example to study purity of a virus preparation. Data from different methods can be combined to gain more complete view on the virus features. As an example, TEM in a combination with gradient centrifugation and cell attachment assays were used to estimate if the virus binds to the cell as native virus or if the binding capability was compromised (Korant *et al.* 1972). More recently, a thermal assay called PaSTRy, where the virus is heated in a presence of a genome intercalating dye, was developed and it is widely used to determine a temperature where the virus opens and the genome becomes accessible for the dye (Walter *et al.* 2012). Also, Cryo-EM and other high-resolution structural methods can be used to observe the state of the virus. However, the latter methods are very laborious and expensive and not suitable for quick and versatile day-to-day measurements.

Most of the methods mentioned above do not provide information that could be monitored over time. Using the PaSTRy assay, one can observe the fluorescence throughout the measurement and analyse the data at different time points and temperatures better providing real-time information. However, when considering the assay in terms of physiological relevance, heating the virus far beyond 40°C is not optimal.

2.4.2 Imaging the virus entry and uncoating in cells

Live cell imaging of virus infection is an invaluable tool to reveal the spatiotemporal events during the process. However, there are many challenges in the imaging. When tracing the virus in cell context using light microscopy, one needs to be able to clearly distinguish the signal of interest from the background signal. For reliable data, the imaging has to be performed under circumstances not disturbing the natural processes of the cell. For example, phototoxicity is an important aspect especially in long time-lapse imaging. Furthermore, the virus needs to be brightly and specifically labelled in a way not to disturb the infectivity. Also, one needs to be able to distinguish between productive and non-productive infection pathways. Numerous strategies and tools for imaging can be used, and depending on the phase of the infection that is of interest, one has to choose and design the experiment according to the specific needs (Witte *et al.* 2018). In general, the detected signalling molecule can reside chemically or biologically associated to the virus proteins or genome, and the means to detect and to follow the signal needs to be selected accordingly.

There are very few articles describing the early events of EV infection using live cell imaging. Entry of E1 was imaged using chemically bound fluorescent molecules on the surface of virus capsid (Pietiainen *et al.* 2005). Combining the capsid labelling and genome labelling using intercalating dye inside mature virus, both the internalization and genome release of PV were described (Bran-

denburg *et al.* 2007). Despite of these successful experiments, the imaging of the early infection processes is not a trivial thing to do. Tracking of a labelled capsid can be rather straightforward, but the visualization of the gene-delivery process still lacks in more robust tools.

3 AIMS OF THE STUDY

I. To study if albumin and ions have an effect to the uncoating of E1, and to characterize these effects using biochemical methods and cryo-EM derived structural information. To develop and test an easy assay to measure the state of virus opening.

II. To study in more detail the differential effect of albumin and ions to CVA9 uncoating, and to observe changes in the virus capsid proteins during the uncoating process.

III. To develop and test a novel intercalating fluorescent dye for multipurpose live-cell imaging of viral RNA.

4 SUMMARY OF THE METHODS

The methods that were used during the thesis are summarized in Table 1. More detailed information of the methods is found in the original papers.

TABLE 1 Summary of the methods used in the publications included in this thesis. Each publication is indicated by the Roman numeral as presented in the list of original publications.

Method	Publication
Spectroscopic measurement of virus opening	I, II, III
Cell Culture	I, II, III
Virus production and purification	I, II, III
Isotopic labelling	I, II
Gradient centrifugation and scintillation analysis	I, II
Virus infectivity assays	I
TEM	I
TEM image analysis	I
Western blotting	II
SDS Page and silver staining	II
Autoradiography	I, II
Cryo-EM imaging	I, II
Cryo-EM data processing and structure building	I, II
Mass spectrometry	III
RNA annealing assay	III
Thermal stability assay	III

5 RESULTS AND DISCUSSION

5.1 E1 uncoating

Many details of E1 entry and uncoating have earlier been investigated in our and other labs. Despite the number of reported details including cellular receptor (Bergelson *et al.* 1992, Jokinen *et al.* 2010), the mode of entry (Marjomaki *et al.* 2002, Upla *et al.* 2004, Rintanen *et al.* 2012, Siljamaki *et al.* 2013) and spatiotemporal events of uncoating and replication (Marjomaki *et al.* 2002, Karjalainen *et al.* 2008, Karjalainen *et al.* 2011), the factor(s) needed for the start of capsid uncoating and genome release have remained a mystery (Marjomaki *et al.* 2015). Inspired by this challenge, we engaged ourselves into the largely unknown world of endosomal ions and extracellular albumin, with an ambition to solve if one or both of these factors would contribute in the priming of E1, i.e. trigger the formation if intermediate particle before capsid uncoating and genome release. Furthermore, we wanted to study if these factors would lead to the genome release. When starting this thesis, a novel uncoating intermediate of E1 was discovered in our lab (Myllynen *et al.* 2016). This intermediate form was porous and allowed small fluorescent SYBR Green II dye (SGII) to enter the capsid and intercalate the genome, but protected the RNA from a degradation by a larger RNAse A molecule (Myllynen *et al.* 2016). By exploiting these newly found features of intermediate uncoating form of E1, we established a fast and simple assay, where different molecular factors could be easily investigated and the formation of both primed and empty EV particles could be separately detected during the measured period of time (IA).

5.1.1 Measuring the virus priming and opening

Detecting the different stages of virus opening is challenging *in vitro*, especially in real time. One can visualise the viruses using TEM, but this offers information only from one point of an assay. The same limitation remains with gradient separation of different virus particle forms. Only assay providing more real time information, a PaSTRy assay, also called a thermal assay or melting

point measurement, provides information about the stability of the virus capsid in high temperatures. However, whereas heating the virus far beyond 40°C can reveal important insights about the capsid dynamics, it does not necessarily provide very relevant information in the physiological sense.

From the above-mentioned techniques, only gradient separation has been considered to distinguish between the altered and empty particles. However, the gradient separation lacks the possibility to visualize the change during a treatment. Making a treatment in various time points and running the resulting samples into different gradients, as was done in paper I Fig. 1E, one can have snapshots from several points of time, but this does not correspond to an assay where the results can be red minute-by-minute. Also, many of the used techniques are rather time consuming and laborious, and because of this not very useful for fast characterisation of wide range of factors possibly affecting the virus stability.

During the study I, we established and optimized an assay, that effectively provides several replicates from up to seven different conditions in cost-effective and quick manner, manageable in a day (IA). The assay was performed in a 96-well plate, using a heated fluorescence plate reader, intercalating SGII and RNAse A nuclease. For each condition of interest, parallel wells were prepared containing 1 µg of virus, 10X dilution of SGII with or without RNAse. From these parallel samples, replicates could be done: we usually used three replicates for each condition with and without RNAse A. Furthermore, for each condition, a blank well was also measured to distinguish the fluorescence originating from the buffer or reagents to the one that originated from the primed or opened virus (I Fig. 1D). EVs are found in three different forms: intact, primed, also known as intermediate or A-particles, and empty. Intact virus did not allow the dye to intercalate with the genome and thus no fluorescence was observed. To distinguish between the last two forms, open and primed, we compared the results with and without RNAse. With RNAse we saw the fluorescence originating from the primed particles, that allow SGII to enter, but protect the RNA genome from RNAse degradation. If the sample without RNAse contained higher fluorescence, it originated from "empty capsids" i.e. the egressed genome that could be degraded by the RNAse. For overall scheme and interpretation of the results of the developed method, see Figures 4 and 5.

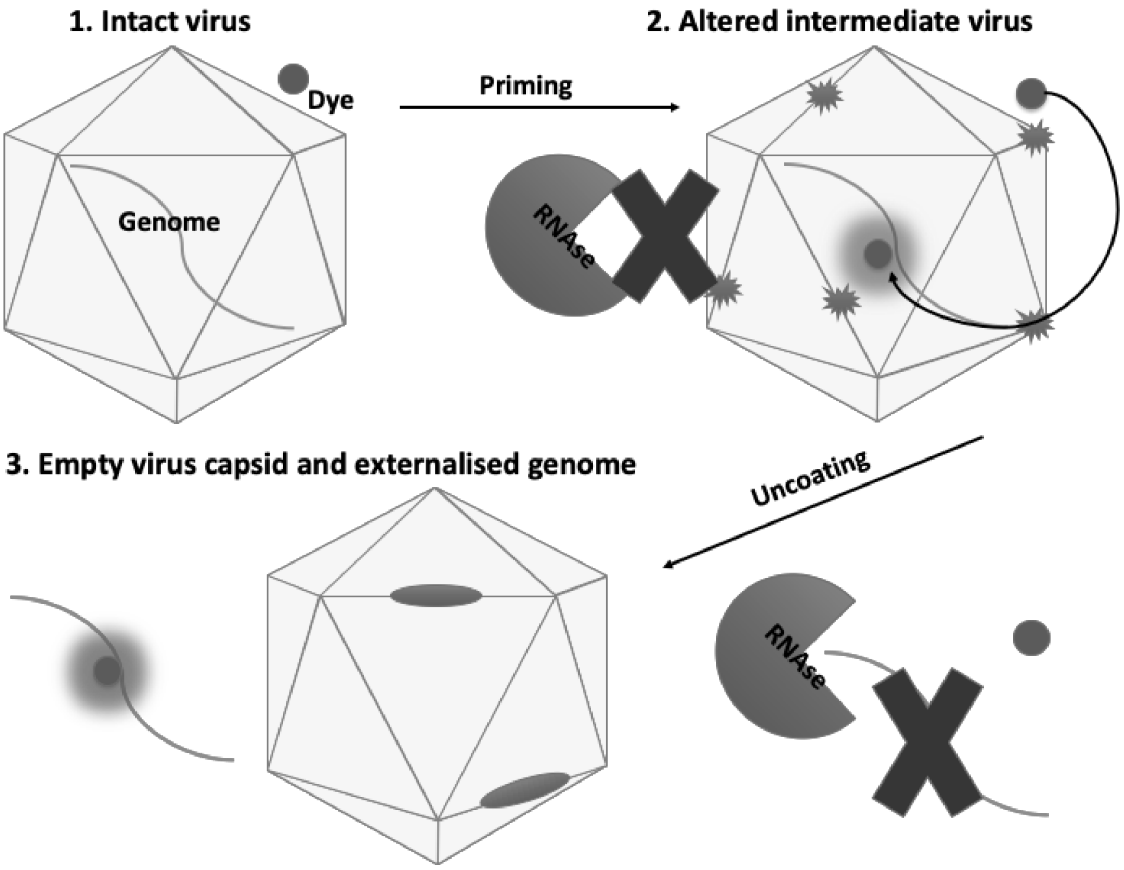

FIGURE 4 Overall scheme of the method. We used SGII intercalating dye to detect the virus opening. (1) In the case of an intact particle, the dye cannot get in contact with the RNA genome and no fluorescence is observed. (2) After priming the virus into an altered, intermediate particle, the particle becomes porous thus letting the dye inside the capsid to intercalate with the genome. This is observed as an increase of fluorescence. As the genome is still inside the capsid, the amount of observed fluorescence is not altered in the presence of RNAse that is too large molecule to get inside the altered virus capsid. (3) The externalised genome is also observed as an increase in the fluorescence as the dye can freely intercalate in the solution. However, in this case, the fluorescence disappears in the presence of the RNAse as the unprotected RNA genome becomes quickly degraded.

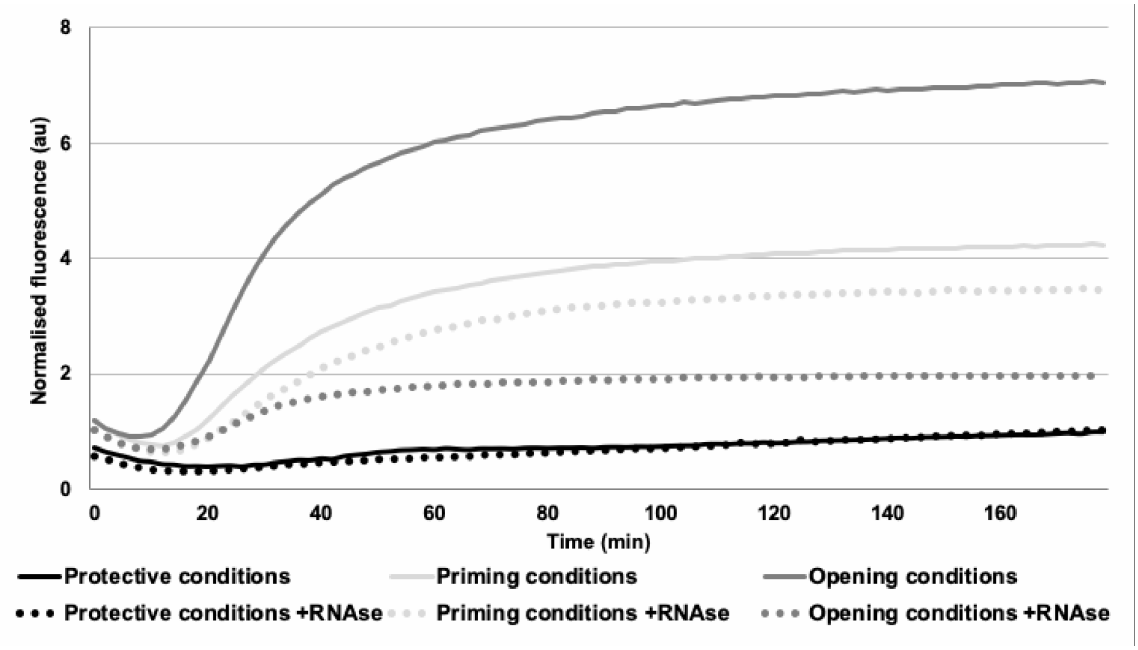

FIGURE 5 Interpretation of the results of an example fluorescence measurement. Three different scenarios are provided. First, in protective conditions (black) the capsid stays intact and the fluorescence with and without RNAse remains low throughout the measurement. Second, in priming conditions (light grey) the fluorescence rises notably during the measurement. As the majority of the fluorescence originates from the altered, primed particles, no difference or only a small difference in the fluorescence with (dotted line) and without (solid line) RNAse can be observed. Fluorescence that is not observed in the presence of RNAse originates from the released genome. Third, in fully opened conditions the fluorescence is high without RNAse, but significantly lower with RNAse as most of the fluorescence originates from the released genome that is degraded in the presence of RNAse.

5.1.2 Serum and ions prime E1 for uncoating

Lonberg-Holm and co-workers in 1976 reported, that PV was stable in 0.1 M NaCl and in serum containing cell culture medium (Lonberg-Holm *et al.* 1976). In 0.01 M NaCl they observed a slow alteration from intact to A particles that could be enhanced by adding cell culture media that included 5 % of inactivated fetal calf serum. They also found that the virus was stable in 5 % serum containing media and the formation of A particles could be induced by diluting it with 0.01 M sodium phosphate buffer. Thus, they showed, that low ion strength could alone induce A-particle formation and this process was enhanced in a presence of serum. Based on these findings, we wanted to further investigate the individual and combined effect of ion changes and serum on the stability of E1.

Using the assay described above, we first observed that the E1 was very stable in physiological ion solutions even at 37 °C, as only minor increase in the fluorescence was observed (I Fig. 1B). In 2 mM $MgCl_2$-PBS, a virus storage buffer used in our lab, small amount of empty virus formation was observed as the

RNAse treatment showed lower fluorescence than without RNAse (I Fig. 1B) This was further confirmed with sucrose gradient separation of ^{35}S labelled virus where small amount of virus located in fraction 7, i.e. 80S empty form of the virus (I Fig. 1B-C). Next, we wanted to see how the virus stability is changed in a cell culture media supplemented with 1% serum (1% S-MEM), a combination normally used in our lab for virus infection experiments. Surprisingly quite fast, within 40 minutes, the fluorescence increased to a high level and reached a plateau (I Fig. 1D). In addition, a clear difference in the amount of fluorescence with and without RNAse was observed suggesting that while majority of the fluorescence originated from primed intermediate virus capsids, also some empty capsids emerged (I Fig. 1D). The process of virus priming was also seen with ^{35}S labelled virus in a 5-20 % sucrose gradient, in an assay where the virus was treated in the 1% S-MEM for 0, 20, 40 and 60 minutes before separation: the amount of primed particles rapidly increased until 40 minutes as the peak at fraction 15, containing intact particles, moved to fraction 13, containing intermediate particles (I Fig. 1E). In addition, formation of empty capsids was also observed as an increase of signal in fractions 7 and 8 while the amount of intact capsids decreased (I Fig. 1E inset). Importantly, the formation of intermediate virus particles was observed to be temperature dependent. In the developed assay, the SGII fluorescence stayed low at room temperature, and after heating the sample to 37°C the fluorescence quickly increased, showing formation of mainly primed particles (I Fig. 1G). Earlier, PV was shown to be stable in physiological ionic strength of cell culture medium supplemented with 5 % serum whereas here, we saw E1 priming in a bit lower serum concentration 1%-S MEM (Lonberg-Holm 1976). This finding suggests, that different EVs showed variability in their response to serum.

Next, in order to examine the effect of altered ion concentrations in virus stability, we made a literature-based estimation of the ionic milieu inside the endosomes where the virus uncoating finally occurs. The measurements found in the literature were done at different stages during the endosome maturation and thus were considered only as guidelines in assessing the conditions inside the neutral MVBs, where the uncoating of E1 and CVA9 takes place (Gerasimenko *et al.* 1998, Christensen *et al.* 2002, Hara-Chikuma *et al.* 2005, Weinert *et al.* 2010, Steinberg *et al.* 2010). The estimated phosphate buffered solution was named NKMC according to the ions it contained (N for sodium, K for potassium, M for magnesium and C for calcium) (I Table 1). Interestingly, this combination of ions only was also found to effectively prime the virus into intermediate form (I Fig. 2A) supporting the earlier finding of low salt buffer inducing the A-particle formation (Lonberg-Holm *et al.* 1976).

5.1.2.1 Different ions have different effects

We wanted to investigate in more detail how different combinations of ions affected the virus state, and moreover, what was the contribution of each type of ion particularly. The concentration of potassium inside cytoplasm is around 140 mM and it is shown to elevate at least to 50 mM in lysosomes (Steinberg *et al.* 2010). Thus, we tested what effect would the double amount of potassium compared to the endosomal estimation have on the virus. Elevated 60 mM potassi-

um pushed the virus more into fully opened form, as more of the fluorescence was sensitive to RNAse treatment (I Fig. 2A).

On the other hand, it has been shown that the divalent cations are important for the virus capsid integrity (Pfeiffer *et al.* 1976, Hull 1978, Sherman *et al.* 2006). Thus, we tested an extreme condition, where we had only sodium chloride and potassium phosphate of NKMC without any Mg^{2+} and Ca^{2+} (I Table 1, NK solution). This combination, as was expected, opened the virus very efficiently (I Fig. 2A). The calcium concentration is suspected to decline quickly, within 10-20 minutes after endosome formation, from 1.8 mM to approximately 3 μM before elevating back up to 0.6 mM during the maturation into lysosomes (Gerasimenko *et al.* 1998, Christensen *et al.* 2002). Unfortunately, data about magnesium concentration is lacking. However, endosomes can provide very local microenvironments, where a change of just few ions can have a large effect on the surrounding ion concentrations (Raiborg *et al.* 2002, Scott and Gruenberg 2011). Thus, it remains unclear if both Mg^{2+} and Ca^{2+} would reach these extreme values inside the endosomes.

Next, we added magnesium or calcium to the NK solution in a concentration used in NKMC, 0.5 mM or 0.2 mM, respectively. Both could independently alter the buffer to be more protective, mainly priming the virus to intermediate form, similarly as the full NKMC (I Fig. 2B). However, the same protective effect was not seen when using ten times less of either of the divalent cations (I Fig. 2B-C). These results support the earlier findings of the capsid stabilizing effect of divalent cations (Pfeiffer *et al.* 1976, Hull 1978, Wetz and Kucinski 1991, Sherman *et al.* 2006). Furthermore, according to these findings, an estimation can be made about the minimally needed divalent cation concentration for the protective effect: 50 μM magnesium did not provide the stabilizing effect whereas 200 μM calcium did. Thus, the borderline for the stabilizing effect of divalent cations lies somewhere in between 50 μM and 200 μM, and the exact needed concentration can also depend on the used ion.

To define more exactly the effect of Na^+ and K^+ concentrations, we kept the Ca^{2+} and Mg^{2+} concentrations in the NKMC estimated values and changed the Na^+ and K^+ concentrations between their extracellular, 140 mM Na^+ and 5 mM K^+, and intracellular, 5 mM Na^+ and 140 mM K^+, values in six steps in a way that the combined Na^+ and K^+ osmolarity stayed the same (I Fig. 2D-F). In this assay, similar observation was made as described above (I Fig. 2A), where high K^+ concentration resulted in higher amount of opened virus. Although, the total osmolarity stayed physiological, the highest K^+ in a combination with the lowest Na^+ concentration resulted in more opened capsids than the concentrations other way around (I Fig. 2D). Furthermore, the additional four measurements with the medium concentrations suggested, that the ion environment alters to more virus opening as the K^+ concentration elevates step-by-step (I Fig. 2E-F).

Previously, a number of studies have been made about different ions affecting the state of viruses (Cords *et al.* 1975, Lonberg-Holm *et al.* 1976, Pfeiffer *et al.* 1976, Hull 1978, Wetz and Kucinski 1991, Bishop and Anderson 1997, Sherman *et al.* 2006). The varying conditions in these studies in terms of ions have mostly been either physiological, such as that in cell culture media, or then

very extreme low ion conditions, such as 20 mM Tris-HCl (Wetz and Kucinski 1991). The effects of low salt buffer and divalent cations in these papers were found to be very similar than what we describe here. In addition, here we provided a more thorough set of experiments about effects of different ions in different concentrations.

Despite very early findings about ions affecting EV stability, no virus uncoating studies has been made in estimated endosomal ion conditions earlier. This might be due to the difficulty in estimating the ion milieu inside the uncoating endosomes, as not too many measurements are available in the literature. The ions have profound effects in cells and living organisms due to osmotic balance and maintaining the membrane potential. Thus, very exact ion homeostasis has to be sustained. However, in a smaller scale, for example within an endosome, specific microenvironments can reside that differ considerably from the surrounding ion concentrations (Scott and Gruenberg 2011). This fact enables viruses to "learn" to use these changes as a part of their uncoating and priming strategies. As shown by us and others, the ions take part in many biological processes, such as virus uncoating. The susceptibility of each virus on different ion concentrations might vary considerably, and this is now easy and convenient to study with the novel assay we published (IA).

5.1.2.2 Albumin is the main priming factor in serum

Next, we wanted to further investigate the observed virus priming effect of 1% serum in cell culture medium. Without added serum, the cell culture medium was only very mildly effective on E1 (I Fig. 3A). When serum was added into NKMC, an ion solution that was already priming the virus without any additives, we observed roughly the same amount of primed particles forming, but much faster (I Fig. 3B). Without serum, the maximal amount of primed particles was formed only at the end of the 3 h measurement period, whereas in the presence of albumin, maximal amount of primed particles was present already after approximately 30 minutes of incubation at 37°C (I Fig. 3B). It is worth noting, that the uncoating of E1 was shown to start after around 30 minutes post infection (Soonsawad *et al.* 2014). This timing goes well together with our *in vitro* observations here.

Earlier, Ward and co-workers showed that faf-BSA induced a formation of echovirus 12 A particles (Ward *et al.* 2000). This provided us a clue, that albumin could be the decisive factor in serum that caused the virus priming in here. Indeed, we saw 0.01% of both BSA as well as faf-BSA providing very similar results as 1% serum in MEM and NKMC (I Fig 3C-D). The amount of 0.01% albumin roughly corresponds to the albumin amount in 1% serum (van der Vusse, G J 2009). With echovirus 12, similar priming effect was not seen using normal BSA as with faf-BSA (Ward *et al.* 2000). This is rather unexpected, since both BSA and faf-BSA contain a high reserve for fatty acid binding (Penn *et al.* 2017). However, there might be some differences in the albumin purification procedures after 20 years, and the different batches of purified albumin might not be totally comparable. Nevertheless, echovirus 12 might act differently than E1 in a presence of albumin.

After determining the albumin as the factor in serum, that mainly contribute to the virus priming, we next wanted to define the mechanism behind this interaction. The lipid factor inside the pocket of EV capsid is strongly connected to the capsid stability (Tuthill *et al.* 2010). On the other hand, the albumin is known to be a strong fatty acid binder and in normal purified form contains reserves for further binding (Penn *et al.* 2017). Thus, we hypothesized, that albumin induce E1 priming by sequestering the fatty acid from the pocket of the virion. To test this, we first measured the amount of faf-BSA in DPBS, that is needed for efficient virus priming, and found it to be 10-20 faf-BSA molecules per one pocket of the virus (I Fig 3G). This indicates, that rather high number of faf-BSA molecules, approximately 600-1200, is needed per virus particle. This might be due to the fact, that the pocket factor binding is shown to be a dynamic process with pocket factors going in and out of the pocket (Martikainen *et al.* 2015). Thus, high enough amount of faf-BSA is needed for it to be able to "steal" enough lipids from the virus, so that the virus particle alteration can start. In a way, the 60 pocket factors per virus acts as a fatty acid reserve, buffering the conversion into A particles until a critical point. Next we added palmitate, the most prevalent fatty acid found from a pocket of bovine enterovirus (Smyth *et al.* 2003), in a solution with 20-fold molar excess of faf-BSA:virus pockets. While unimolar ratio of palmitate:faf-BSA showed no protection from virus priming, 10:1 showed small, 20:1 increased, and 50:1 ratio full protection from the faf-BSA induced virus priming (I Fig. 3G, 1:1 and 10:1 ratio data not shown). Thus, a high amount of palmitate was needed to block the effect of faf-BSA. In this process, the faf-BSA could in turn act as a buffer, primarily binding the added fatty acids until the concentration grows high enough for a substantial binding into the pocket of a virion. Altogether, a physiological faf-BSA concentration could prime the E1, and at least 10:1 excess of palmitate was needed to protect from the priming. The prevalent ratio of fatty acids and albumin in serum is approximately 1:1 (van der Vusse, G J 2009, Abdelmagid *et al.* 2015) suggesting, that the virus particles can be in a primed intermediate state already outside cells. However, as echovirus 12 was found to alter into A-particle in a presence of faf-BSA but not BSA, different viruses may have higher affinity pocket for the fatty acids than E1, thus not releasing the pocket factor as easily. The effect of albumin in triggering uncoating of EVs was shown earlier (Ward *et al.* 2000), but to the best of our knowledge, no direct connection of albumin and fatty acids has been shown before linked to EV priming.

In summary, using biochemical methods, we showed that both albumin and ions can contribute to the virus priming, and that extreme changes in the ion concentrations push the virus to uncoat and release the genome. However, with this data, we cannot determine the definitive factor(s) that ultimately push, or pull, the genome out from the virus capsid. Furthermore, it is highly probable, that different factors act jointly in an event cascade leading to efficient EV priming and uncoating. For example, influenza A virus is shown to require first priming with lowered pH, after which elevated potassium can further alter the capsid formation that is needed for genome uncoating (Stauffer *et al.* 2014). Thus, only one factor would not lead to efficient uncoating, but the total effect of several factors, that can be molecular and cellular, would be enough. This en-

sures, that the genome uncoating happens in a right cellular compartment with a right timing, to increase the possibility for productive infection.

Depending on the virus type, rather high multiplicity of infection is often used in experiments to achieve efficient infection and some of the viruses might end up on a route where they do not meet all, or any, of the factors needed for efficient uncoating. On the other hand, sometimes viruses might end up infecting "by accident", for example cells not having receptor for the virus, but getting inside by some non-specific route. One can speculate that extracellular albumin together with endosomal ion changes could prime the virus ready for cellular proteins, such as PLA2G16, beta 2 microglobulin and FcRn to be involved in the uncoating process (Heikkila *et al.* 2010, Staring *et al.* 2017, Morosky *et al.* 2019, Zhao *et al.* 2019). Furthermore, in a case, where the genome egress takes place from the endosomal membrane bound capsid, through a capsid protein induced hole in the endosomal limiting membrane as suggested earlier (Groppelli *et al.* 2017), the resulting influx of potassium ions through the hole from cytoplasm into the capsid and/or endosome, could act as a final trigger for a final genome egress. Such cation permeating pH independent virus-lipid layer -interaction has previously shown for PV and could take place also in a case of E1 (Tosteson and Chow 1997).

5.1.3 Cryo-EM resolved changes in the primed virus structure

We wanted to define the structural changes of a virus particle that was treated with a combination of ions estimated for lumen of uncoating endosomes, and albumin that the virus potentially meets already in the extracellular space. To be able to define the structure using cryoEM, we needed a notably higher virus concentration than what was used in the fluorescence measurements. This resulted in a slightly different concentration of ions and faf-BSA when compared to the 0.01% faf-BSA in NKMC (I Table 1, EM buffer). However, the difference between the buffers was small, and it was confirmed that the EM buffer provided similar results to NKMC (I Fig. 3E).

Interestingly, after learning how to produce and confirm the formation of E1 primed particles in a reproducible way, we noticed that they had a different appearance after negative staining in TEM. The intermediate particles were darker than the intact particles and yet clearly distinguishable from the empty particles (I Fig. 4A). Thus, the intermediate particles of also other EVs could possibly be distinguished from the intact particles by this method. Previously, the darker appearance of some virus particles was considered to be a result of normal variance in negative staining, but after this observation, intermediate particles were recognised also from other TEM data of our lab. The intact and intermediate particles could not be clearly distinguished in the cryo-EM micrographs due to the typically low contrast of the micrographs without any stain, but the 2D averages showed clear differences between the different virus states (I Fig. 4B-C).

We reconstructed the intact and primed particle with a resolution of 3.5 Å and 3.6 Å, respectively (I Fig. 4D-E). Altogether, the non-treated intact particle was similar to the earlier published X-ray structure of E1 (1EV1) (Filman *et al.*

1998) and almost all amino acids could be modelled into the structure (I Table 2). In addition, the intact particle contained the pocket factor (I Fig. 5A-C). The treated particle was found to be somewhat different to the crystal structure and thus resulted in gaps in the modelled amino acids within VP1-3, whereas VP4 could not be modelled at all (I Table 2). However, partial presence of the VP4 was confirmed using autoradiography (I Fig. 7). The fatty acid pocket was collapsed and the pocket factor could not be reconstructed (I Fig 5D-F). The treated particle was expanded about 4 %, as usually observed with enteroviral A particles. In addition to the ordered capsid proteins, also the genome nearest to the capsid was highly ordered in both particles (I Fig. 4H and K), and connected to the capsid VP2 protein at the 2-fold axis (I Fig. 5A) similarly as shown earlier for HRV (Pickl-Herk *et al.* 2013). This connection was maintained in the treated particle (I Fig. 5D). Interestingly, the treated particle contained enlarged opening of the 2-fold axis as well as protrusions spanning across the capsid, probably formed by the N-terminal amino acids of the VP1(I Fig. 6). Similar VP1 N-terminus protrusions were earlier found for other EV A-particles (Ren *et al.* 2013, Butan *et al.* 2014, Liu *et al.* 2018). Although left unconfirmed, it seems possible that the remaining VP4 could contribute to the poorly ordered density, both inside the capsid and traversing through the capsid, in the altered particle (I Fig. 6C-D).

In this study, we provided novel structural information about intermediate EV, E1 particle. Importantly, we demonstrated that the molecular factors, ions and albumin, efficiently primed E1 into a form that had many similar features as earlier resolved A particle structures of other viruses primed by heating, receptor binding or low pH. In addition, we showed that two other members of EV-Bs, CVA9 and CVB3, provided very similar results in our fluorescence assay in 1% S-MEM at 37°C suggesting that, also other EVs might have similar tendency for priming and uncoating under physiological albumin and altered endosomal ion concentrations (I Fig. 1F).

5.2 Priming of CVA9 separately with faf-BSA or ions reveals their differential effects leading to virus opening

Similar to E1, many details of CVA9 entry and uncoating are already resolved (Marjomaki *et al.* 2015). However, the same unresolved question remains: what makes the virus to transform into an altered intermediate particle and finally release its genome (Marjomaki *et al.* 2015)? With E1, we studied the combined effect of ion changes and faf-BSA to the structure of the virus capsid. Here, we wanted to study if the same factors, faf-BSA and ion changes, affected similarly to the CVA9. Furthermore, we wanted to resolve their separate effects on the virus structure.

5.2.1 Ions and faf-BSA prime CVA9

To begin with, we tested the stability of the virus in physiological ion buffer, DPBS, using the fluorescence assay developed during the previous study (IA). The fluorescence remained low throughout the measurement implying, that the virus remained rather stabile in DPBS at 37 °C (II Fig. 1A). However, small amount of empty particles were formed during the first 60 min of the measurement whereas, in comparison, no empty particles were observed in a case of E1 (II Fig. 1A, I Fig 1B).

Next, we composed a literature-based ion-buffer mimicking the ion conditions potentially residing inside the uncoating MVBs (Gerasimenko *et al.* 1998, Christensen *et al.* 2002, Hara-Chikuma *et al.* 2005, Steinberg *et al.* 2010, Weinert *et al.* 2010,). CVA9 was found to be more prone to release its genome due to changes in ion concentrations than E1 (data not shown). Thus, to achieve higher amount of intermediate particle formation, the CVA9 ion-treatment buffer required a higher, 0.45 mM, concentration of protective calcium than the NKMC buffer used for E1 (0.2 mM). The resulting phosphate buffered saline used for ion-treatment of CVA9 contained 20 mM NaCl, 30 mM K^+, 0.5 mM $MgCl_2$ and 0.45 mM $CaCl_2$. With this buffer, we observed formation of both intermediate and empty particles (II Fig. 1A). The formation of intermediate and empty particles was also observed using gradient separation of metabolically labelled CVA9 (II Fig. 1C).

Although CVA9 was observed to be more fragile than E1 in low salt buffer, the effect of faf-BSA was highly similar for both viruses. In a presence of 0.01 % faf-BSA in DPBS the virus was efficiently, within 40 minutes, primed into intermediate particles with only minor formation of empty particles (II Fig. 1B-C). Interestingly, when faf-BSA was added into the ion-treatment buffer, the priming happened faster, within 20 minutes, after which the virus particles remained similarly stabile as in a presence of faf-BSA in physiological salt buffer DPBS (II Fig. 1B). Thus, the combination treatment resulted in faster formation of stable intermediate particles in comparison to the factors individually.

The virus priming was observed to be similarly dependent on the concentration of faf-BSA and added fatty acid palmitate, as with E1. Per one virus pocket factor, 10 faf-BSA molecules were needed for efficient intermediate particle formation, and 20 palmitate molecules per faf-BSA could rescue the virus from the transition (II Fig. 1D). Interestingly, we found, that majority of the ion-treatment caused transition to intermediate particles could also be blocked with the same amount of palmitate (II Fig. 1E).

Altogether, although CVA9 was observed to be somewhat more fragile in low-salt buffer than E1, faf-BSA had a very similar effect to it. The effect of faf-BSA to CVA9 was, in fact, already suggested by our data in the paper I, as 1% S-MEM could similarly prime both E1 and CVA9 (I Fig. 1F). Furthermore, the priming by faf-BSA was found to be concentration dependent and preventable with palmitate, as with E1. In addition, we observed that the intermediate particle formation induced by low-ion buffer could also be blocked with palmitate suggesting that the ion induced priming was also, at least partly, dependent on the pocket factor release.

As discussed in a case of E1, the approximate ratio of albumin and fatty acids in serum could result in primed virus particles outside cells. Our results here show, that this could be the case also for CVA9. Albumin was found to prime also another EV-B, CVB3 (Carson and Cole 2020). Thus, it seems possible, that albumin acts as a factor triggering a change from intact to intermediate particle for a larger group of enteroviruses.

We used 30 mM potassium concentration in our endosomal ion estimations. However, the concentration is shown to increase up to 50 mM in lysosomes (Steinberg *et al.* 2010) and the normal accumulation of potassium in maturing endosomes was recently shown to be dependent on the normal appearance of cellular cholesterol (Charlton *et al.* 2019). Interestingly, E1 enter cells inside cholesterol rich endosomal structures and furthermore, its infection was dependent on the presence of cholesterol (Siljamaki *et al.* 2013). This could indicate a high potassium concentration inside the MVBs where both E1 and CVA9 uncoat and release genome. Herein, we showed CVA9 to easily release its genome in a presence of altered ions including elevated potassium. Furthermore, in paper I we showed that even E1 was more resistant for ionic changes, elevated potassium induced its genome release. Thus, we propose that altered ionic conditions including elevated potassium concentration might act as a final trigger for genome release for some enteroviruses, such as E1 and CVA9.

5.2.2 Ions and faf-BSA induce formation of novel capsid protein clusters

To study in more detail the possible changes in capsid protein connections caused by ion-treatment and 0.01 % faf-BSA in DPBS, we used reducing and non-reducing SDS-Page approaches: western blotting, silver staining and autoradiography. Western blots using antibodies against VP1, VP2 and VP3 revealed the anticipated bands for each protein in reduced and non-reduced samples of both treatments (II Fig. 2A-C). Interestingly, using non-reducing sample preparation, additional fainter bands were seen with all used antibodies. With VP1 antibody, the faf-BSA in DPBS showed two additional bands around 50-75 kDa (II Fig. 2A). VP2 antibody revealed bands, or areas, around 75 kDa in both ion-treated and faf-BSA in DPBS treated samples (II Fig. 2B) as did also VP3 antibody for faf-BSA in DPBS treated sample. These findings suggested that new connections between capsid proteins, detected only after non-reducing sample preparation, were formed. With silver staining also a band around 75 kDa was observed in ion-treated non-reduced but not in reduced sample or in the control samples (II Fig. 2D). Similar band could not be observed in samples treated with faf-BSA in DPBS or with a combination of faf-BSA in ion-treatment because the possible band was masked by faf-BSA originating silver stain signal (II Fig. 2E). However, autoradiography revealing only radioactive capsid proteins and not albumin confirmed the formation of similar bands around 75 kDa for all three treatments in non-reduced samples (II Fig. 2F, white rectangle).

Another surprising observation could also be made from the autoradiography: by visual estimation a clear difference in the amount of VP4 protein between the samples was seen. About 8 kDa VP4 band was clearly fainter in the

ion-treated sample regardless of the same amount of ^{35}S labelled CVA9 used in all samples (II Fig. 2F black rectangle). The protein could not simply disappear from the sample suggesting that, especially during the ion treatment part of VP4 relocated to another molecular weight position in the gel probably due to novel connections with other capsid proteins. This was very interesting observation to us. The existence of VP4 in the altered particle structure has remained a bit of a mystery. In early studies it was found to be lost from the A-particles of PV, HRV and CVB3 resulting in loss of infectivity (Crowell and Philipson 1971, Lonberg-Holm and Korant 1972, Fricks and Hogle 1990, Greve *et al.* 1991). Furthermore, a clear VP4 occupied density has been missing in thus far published, globally induced, A-particle structures. However, cryo-EM maps also contain less well resolved areas that may be occupied by disordered or partly missing proteins, such as VP4. Thus, additional approaches are needed for more precise interpretation of the existence of VP4 in the altered capsid, as was used earlier (Ren *et al.* 2013, Liu *et al.* 2018) and by us (I Fig. 7).

Herein, we decided to perform quantified analysis of VP4 that was either relocated in the gel, i.e. not found at 8 kDa band due to novel connections with other capsid proteins, or detached from the capsid during the treatments using silver staining of SDS-Page gels. First, in reducing conditions, we detected approximately all the VP4 at its expected position after all treatments (II materials and methods). Thus, by dialyzing the samples before the reducing sample preparation, we could determine the amount of VP4 that was detached from the capsid during the treatment. Furthermore, as suggested by the western blots and autoradiography, using non-reducing SDS-Page the novel higher molecular weight complexes were retained, revealing the part of VP4 that was potentially connected to these complexes and thus not found at 8 kDa band.

Our results showed that during the ion treatment 70 % of VP4 was detached from the capsid and no VP4 was relocated into higher molecular weight complexes (II Fig. 3A). This was surprising after the visual interpretation of the autoradiography described above. The observed lighter 8 kDa VP4 band in the non-reduced ion-treated autoradiography sample suggested more relocation than detachment as detached VP4 would have located at the expected 8 kDa position in the non-dialysed sample resulting in a darker band (II Fig. 2F). Thus, we also analysed the non-dialysed sample, which surprisingly showed that 46 % of VP4 was relocated (II Table 1). The difference between the dialysed and non-dialysed samples suggests that VP4 forms novel but weak interactions or connections with capsid proteins that break during the dialysis and release the VP4 through the dialysis membrane. The release from the complexes is understandable as the VP4 itself does not contain any cysteines needed for sulphide bridge formation. Thus, it is probably more loosely bound in complexes formed by other capsid proteins by sulphide bridge formation. In combination treatment, faf-BSA with ions, 72 % of VP4 was detached and in addition 15 % was relocated (II Fig. 3A). Also in this case, analysis of the non-dialysed sample showed more, 34 %, of VP4 to be relocated (II Table 1). When treated with 0.01 % faf-BSA in DPBS less, 46 %, of VP4 was detached and 18 % relocated (II Fig. 3A). In this treatment, the amount of relocated VP4 in non-dialysed sample was also somewhat higher, 30 %, confirming that part of the VP4 was released from

the complexes during the dialysis. However, importantly, when albumin was present in the treatment, less VP4 was released in the dialysis. The results suggest that the ion-treatment triggers more radical change in VP4, whereas faf-BSA has a milder effect, keeping more of the VP4 tightly associated with other capsid proteins. In the combination treatment, less of the relocated VP4 was detached during the dialysis than in the ion-treatment, implying that the formed connections were stronger in a presence of albumin as suggested also by stabilized intermediate particle in the fluorescence measurement (II Fig. 1B).

The presence of VP4 in the 75 kDa band of both ion-treatment and 0.01 % faf-BSA in DPBS was confirmed using mass spectrometry. The amino acid coverage was highest for VP4 and the presence of all other capsid proteins was also confirmed at the 75 kDa band (II Table 1). It is unlikely that the found band would contain full protomers, as the combined molecular weight of the capsid proteins is around 95 kDa. Therefore, the proteins presumably form different aggregates around the same molecular weight, and, in fact, the observed band could instead be called 75 kDa "area" because of the wide and unsharp nature of the observed silver stain or autoradiography signal.

Altogether, when thinking of the secondary infection route of the virus, the different effects of these factors are sensible. Interaction with albumin outside cells results in primed but stable virus particle that still contain majority of VP4, needed for retained infectivity and ability for genome release into the cytoplasm for many EVs (Fuchs and Blaas 2010, Groppelli *et al.* 2017). After entry, and upon changes in the endosomal ions, more VP4 is released enabling secure escort of the genome from the capsid to the cytoplasm, as proposed for poliovirus (Groppelli *et al.* 2017).

5.2.3 Cryo-EM of ion- and faf-BSA treatments probably show different states of A-particles

Finally, we solved cryo-EM structures of intact, faf-BSA- and ion-treated viruses to 3.1, 3.9 and 3.4 Å resolution respectively. The high-resolution map of non-treated CVA9 accommodated all four capsid proteins (II Table 2), showed density of the lipid factor (II Fig. 7) and connection between viral genome and Trp38 of VP2 close to the 2-fold axis (II Fig. 6). Both structures of the treated viruses showed 4-5 % capsid expansion and release of the lipid factor, characteristics that are generally thought as hallmarks of the A-particle (II Fig. 5 and 7). Most of the VP1-3 but not VP4 could be modelled in the reconstructions of the primed particles (II Table 2). In addition, interesting differences between the structures were observed. In the ion-treated virus structure, poorly defined density was seen on the outside surface of the virus, above the 2-fold opening (II Fig. 8B). This density could be structural proteins or viral genome exiting the capsid interior, but at the low local resolution it could not be defined. In the faf-BSA treated virus structure poorly defined area was also detected near the 2-fold axis, but on the inside of the virus (II Fig. 8C). These findings suggest that the structures show two different states during the virus uncoating.

Recently, also other studies have shown structures of different states of A-particles of the same virus (Strauss *et al.* 2017, Shah *et al.* 2020). Thus, it seems

that depending on the priming factor, different semi-stable forms of a virus can exist showing different characteristics and degree of uncoating. Herein, we show that albumin retains more VP4 within the intermediate particle resulting in a more stable and potentially infectious particle with different structural features in comparison to ions primed particle, having less VP4, being more prone to open and showing more prominent structural changes towards the genome release.

5.3 Detecting the viral genome *in vitro* and *in vivo* – development of new tools

Visualising an infection of very small, approximately 30 nm sized, virus is not an easy task. For fusion protein techniques, only very limited number of nucleotides can be incorporated into such small and tightly packed viral genome. In addition, fusion proteins can be detected only after the genome translation, and for visualising the early infection they need to be fused with the capsid proteins that could in turn easily affect the infectivity of the virus. Fluorophores can also be attached to the capsid surface using different chemically reactive groups. Also in this case, the small size of the capsid becomes a challenge, as not too many fluorophores fit the surface and the brightness of the fluorescent signal may become a problem. Even if one is able to visualise and track the virus inside a cell, simply following virus capsids does not necessarily provide very meaningful information as the destiny of a virus can be hard to determine. A combination of dyes can be used to overcome this problem and achieve more accurate information.

In this thesis, we focused on developing and characterizing a functionalized RNA sensing dye as a tool for imaging virus genome uncoating. To our best knowledge, no such functionalized intercalating dyes are available, at least commercially. The long-term aim of the dye development is that the genome sensing dye could be incorporated to the surface proteins the virus capsid, where it could intercalate with the egressed genome. The capsid could be stained in combination with another fluorescent dye to follow the virus entry. Another strategy would be to attach the dye into a hydrophilic particle, for example nanoparticle that would enhance the fluorescence signal. This particle, with multiple dyes bound on its surface, could be fed during the infection into the same structures with the virus where it could potentially report the genome egress.

5.3.1 SGII, MeS and conjugates

SYBR-family nucleic acid intercalating dyes are widely used in different fluorescent staining, visualising and measurement strategies. The intercalating dye binds to the double stranded nucleic acid resulting up to 1000-fold enhancement in the molecule´s fluorescence as result of a restriction in its torsional motion (Ihmels *et al.* 2005, Karunakaran *et al.* 2006). The structure of many widely

used intercalating fluorophores are still unknown. While the structure of a DNA binding SYBR Green I was previously resolved (Zipper *et al.* 2004), the structure of RNA binding SGII has remained unresolved. Defining the binding properties of the missing fluorescent dyes and understanding the factors that contribute to the interaction with RNA or DNA is crucial for development of new versatile dyes.

Herein, we first defined the crystal structure of SGII dye (III Fig. 2 C-D). After this, we developed a scheme for synthesis of SGII related dyes (III Scheme 1) resulting in 5 new molecules. The first molecule MeS, very similar to the SGII (III Fig. 1), was used as a backbone to produce four different functionalized version of it: OH, COOH, NHS and COOMe. The crystal structure of MeS was also determined (III Fig. 2 A-B), whereas the other molecules did not crystallize probably due to the long alkyl chains present in the dyes. The reason for having this 11-carbon chain in between was to minimalize steric hindrance post conjugation. The only difference in the structure of SGII and MeS was in the pendant arm of the molecule. In lowered pH, the longer, N-2-(dimethylamino)-ethylthiolate arm of SGII can protonate the amino group thus taking on an additional positive charge resulting in significantly improved water solubility over the MeS dye.

The absorption spectra of the novel dyes were similar to that of the SGII showing absorption maxima at 479 nm (III Fig. 3, Table 1). The emission maxima were also similar for all at 505 nm. The synthesized dyes exhibited negligible fluorescence in the absence of nucleic acid and when bound to nucleic acid they showed similar, over 1000-fold, increase in the fluorescence as shown earlier for other intercalating dyes (Ihmels *et al.* 2005, Karunakaran *et al.* 2006). The MeS showed higher fluorescence than the other synthesized dyes and importantly also higher than SGII with all of the tested double stranded nucleic acids (III Fig. 9). None of the fluorophores showed noticeable fluorescence with single stranded linear DNA (III Fig. 9).

Several binding parameters for each dye were defined. The SGII had a higher binding constant over MeS, whereas MeS occupied fewer base pairs when bound, and showed a higher fluorescence quantum yield (III Table 2). Altogether, a longer arm in a case of SGI and SGII resulted in stronger binding than MeS but required more space. The higher quantum yield and lower requirement of binding sites of MeS resulted in higher obtained fluorescence than SGII. Apparently, the adjacent MeS fluorophores were not bound too close to each other, as it could result in fluorescence quenching. Whereas MeS was observed to have superior fluorescence over the SGII, the stronger binding of SGII over MeS could be profitable in more complex systems, including for example cellular environment. However, this remains to be examined. In a case of OH and NHS reactive groups, the longer arm resulted in weaker binding probably because of a partial negative charge of the arm that hindered the binding to the nucleic acid groove.

5.3.2 Biological applications

After defining the chemical details of the newly synthesized dyes, we wanted to characterize some of them in several *in vitro* assays to confirm their usability, and also to see if novel information could be gained by using them.

First, we used MeS in a PaSTRy assay in parallel with SGII that has been used also earlier in the assay. The resulting melting curve profiles were highly similar (III Fig. 10). As expected according to the dye characterisations, the MeS provided a higher fluorescence peak than the SGII. Importantly, we detected the genome release also using the NHS-conjugated dye that was bound to free lysine residues of the viral capsid (III Fig. 10 inset). Although the amount of detected fluorescence was only a fraction from that of MeS or SGII, the peak was evident. The lower fluorescence was expected, as the dye characterization suggested lower fluorescence capabilities, probably due to the long alkyl chain between the dye and the NHS conjugation. Also, the amount of capsid bound dye was remarkably lower than the amount freely diffusing dye in the solution.

Next, we tested the dyes in the assay we developed in the paper I. Again, MeS showed similar fluorescence profile and somewhat higher fluorescence as observed in the paper I (III Fig. 11). As in the PaSTRy assay, the virus opening was detected with the capsid bound NHS dye with lower fluorescence than with the free dye (III Fig. 11). It is, however, worth noting that although the fluorescence amount of NHS-conjugated dye remains lower, it is highly localised. Thus, inside a cell, the fluorescence could still be detectable because of several dyes emitting fluorescence from very exactly localised area.

After confirming that the MeS worked very similar as SGII in the biological applications described above, we wanted to test it in a novel assay, where we estimated the amount of double stranded secondary structures in the single stranded viral RNA genome. Earlier, some calculation-based estimations have been done about the amount of secondary structures in enteroviral genome (Simmonds *et al.* 2004, Davis *et al.* 2008). Especially the non-translational regions are known to include important secondary structures (Mirmomeni *et al.* 1997, Witwer *et al.* 2001). Also, a commercial PicoGreen dye has been previously used to evaluate the single-to-double-strand ratio by defining fluorescence lifetime of the dye, when bound to target nucleic acids (Cosa *et al.* 2001, Beach *et al.* 2003). Here, we evaluated the part of the virus genome that spontaneously formed double stranded structures by simply observing the amount of fluorescence. To be able to do this, we first studied how much fluorescence MeS showed in a presence of 300 ng of RNA which was 30, 60 or 90 % double stranded. 300 ng approximately corresponds to the amount of RNA genome contained by 1 µg of E1. To compare the features of the different dyes, we made the same measurement using also SGI and SGII. First of all, we earlier showed, that all of these dyes showed negligible amount of fluorescence in a presence of linear single stranded DNA (III Fig. 9). With this knowledge, we assumed that the detected fluorescence originated from the double stranded RNA regions. We measured the fluorescence in H_2O and were able to show a linear dependence with MeS but not with SGI or SGII (III Fig. 12). Then we measured the fluorescence in an ion combination that was observed to fully open E1 in paper 1 (I Table 1 and

Fig. 2A, solution NK). In this environment, the double stranded dependence of MeS fluorescence was not linear all the way to 90 % (III Fig. 13). Nevertheless, we were able to determine the amount of double stranded genome of E1 to around 51 %. This result provides experimental based estimation of the secondary structure in addition to the previously published calculation-based predictions (Simmonds *et al.* 2004, Davis *et al.* 2008). Furthermore, the finding suggests that in addition to the well described secondary and tertiary structures mainly in the untranslated regions of EVs (Mirmomeni *et al.* 1997, Witwer *et al.* 2001), also other regions of the viral genome forms secondary structures.

In summary, the challenge in using the intercalating DNA and RNA sensing dyes in live cell imaging is that the dyes are hydrophobic, and thus can penetrate through the cellular membranes. As a result, when added on cells, they stain all the DNA and RNA inside cells. Here we described a synthesis of a SGII like cyanine dye that can be used as a better alternative for SGII. In addition, its functionalised forms can be incorporated into a virus capsid or other solid support to be internalised into cells with the virus. In the future, by using this dye, we can hopefully provide novel information about the viral uncoating and genome egress. Furthermore, the dye can be attached in principle to any reactive group of any molecule meaning that further applications can be developed according to one´s needs. Finally, we provided important characterization of dye properties that affect the binding and brightness.

6 CONCLUDING REMARKS

The main conclusions of this thesis are:

I Two physiological factors, albumin in the extracellular space, and ion conditions estimated to prevail inside uncoating endosomes, were found to trigger the formation of primed, intermediate E1 particle. Combination of these two triggered a faster change in the particle, and this particle structure shared many characteristics with the earlier described intermediate particles for other viruses such as the enlarged opening in the 2-fold axis. The priming by albumin was dependent on the albumin concentration and could be blocked in concentration dependent manner with the fatty acid palmitate.

II The same factors, albumin and combination of ions were found to prime also CVA9. However, CVA9 was found to be more prone to opening due to changes in ions. Both biochemical and structural data suggested that albumin and ions had different effects on the virus particle. Albumin resulted in a more stable intermediate particle, whereas ion changes resulted in more fragile particle presumably closer to the actual genome release.

III A novel intercalating fluorescent dye, closely resembling SGII, was developed. This dye was found to be superior in terms of fluorescence but more loosely bound to double stranded nucleic acid than SGII. Using the novel dye, the amount of double stranded regions in E1 genome could be estimated. Furthermore, different functionalised versions of the dye were synthesised, from which the NHS-modified version, bound to virus capsid, was confirmed to detect virus opening in vitro.

Acknowledgements

This work was carried out at the University of Jyväskylä, at the Department of Biological and Environmental Sciences and Nano Science Center, Division of Cell and Molecular Biology during the years 2015-2020. The thesis was funded by University of Jyväskylä Graduate School for Doctoral Studies, Kordelin foundation and Jane and Aatos Erkko foundation.

I would like to acknowledge all the people involved in my expedition to the PhD. To begin with, I would like to express my deepest gratitude to my supervisor, Professor Varpu Marjomäki. You offered all the help I needed and shared your enthusiasm and kindness during the struggles. I am grateful for all the possibilities you provided, for example to meet other scientists in conferences and work trips. I think that you give a right amount of responsibility and independents, and gently push your students out from the comfort zone. Thank you for everything!

Next, I want to thank the reviewers of my thesis, Docent Kirsi Rilla and Docent Kari Airenne. Your thorough work and valuable comments on my thesis really made it to the next level. I would also like to thank Docent Petri Susi, who kindly accepted our invitation to act as my opponent. In addition, I have had two thesis committee members, who have provided me support, expertise and invaluable comments throughout the journey. Thank you, Dr. Olli Laitinen and Prof. Musa Mhlanga.

I also want to thank all the co-authors in the papers. Especially Dr. Aušra Domanska and Prof. Sarah Butcher from University of Helsinki, who have been not only providing their expertise on cryoEM in our joint papers, but also helping me developing in scientific writing and reporting results. I am also very grateful for Dr. Dieter Blaas for inviting me to Vienna to learn from him and use his excellent laboratory, as well as his wonderful group members who made me feel at home during my research visit.

Next, I would like to thank the best colleagues one could hope for. First, the wonderful Marjomäki group. Thank you, Paula, Mari, Mira, Dhanik, Ville, Sailee and Helena. We have had an excellent atmosphere in the group, we help each other and share knowledge and support. Paula and Mari, already working elsewhere, you were really big role models to me on how to do things in efficient and professional way. Mira, we started the PhD rather close by to each other. You were already a senior in the group, and I feel you provided me invaluable help and support during the years. Thank you so much! Ville, we have a joint paper included in my (and your) thesis, but besides your professional contribution, I have enjoyed our conversations on any topic, especially beer brewing. Dhanik and Sailee, you two are the most polite and nicest people I know. Your passion to do science can be seen every day, and I am sure you will be very successful on your PhD and beyond! Thank you, Helena, for cheering our group with your presence during your several visits in Jyväskylä. I also want to acknowledge all the students and trainees who have worked in the group over the years and helped me in many ways. Especially Tino, at some

point I think you were a “virus production machine”, and still I managed to spend it all.

Then, I would like to thank all the colleagues outside our group. Alli, Laura and Petri, I am grateful for your assistance on technical issue. You are really easy to work with and always willing to help! Pilvi, Kati, Lina, Leena, Ele, Vesa and Jori. I want to thank you for all the important moments in and out the university. Lunch breaks, conversations, Christmas parties and whatnot. It has been really important to be able to open and share things with peers, and we´ve had many discussions over the years that I am very grateful of. I especially want to thank Jori. I think that your example and confidence in doing science made me consider to do the PhD in the first place.

Next, I want to thank my family and friends. Most of you probably have not known more, than that I have been doing a PhD about viruses. I know that I have not been sharing too much details, but still all of your contribution in my work has been major. As the work has been rather stressful from time to time, it has been important to be with people with whom I can think and do totally different things. So, thank you Mom, Dad, Vilja, Pirkka and Touko, and of course all the spouses. I also want to thank my wife´s, Elina´s family for everything. Thank you also Panu and Mikko, our yearly “A-class” meetings have always been worth the wait! Finally, I want to thank my bandmates Jani, Olli, Atte, Touko again and Marko. Few gigs every now and then have been a perfect balance for the academic work.

Most importantly, thank you, Elina. We´ve had a ride. Ups, downs and busy years. Two amazing and wonderful children on the way, Leino and Taimi. I cannot come up with any other words than thank you so much for being there, I love you.

YHTEENVETO (RÉSUMÉ IN FINNISH)

Enterovirusten avautumiseen vaikuttavien tekijöiden tutkiminen

Virukset ovat erittäin pieniä partikkeleita, joiden perimää ympäröi proteiinikuori ja lisäksi niitä voi suojata myös lipidivaippa. Mittakaavaltaan virukset ovat noin 100-1000 kertaa ihmisen soluja pienempiä. Virukset ovat monesta syystä erittäin mielenkiintoisia biologisia partikkeleita. Niillä ei ole omaa aineenvaihduntaa, eivätkä ne siten pysty elollisiin toimintoihin, vaan tarvitsevat isäntäsolun ”elääkseen”, eli käytännössä monistuakseen. Monistuttuaan virukset poistuvat isäntäsolusta usein tappamalla sen, jonka jälkeen niiden toiminta on jälleen täysin riippuvaisia ympäristöstä. Ne eivät esimerkiksi liiku itse, vaan ne ajelehtivat ympäristönsä mukana. Virusten ”toiminta” on siis täysin riippuvaista isäntäsolun aineenvaihdunnasta ja ympäristön muutoksista.
Tästä huolimatta, tai ehkä juuri tästä syystä, virukset ovat ”oppineet” käyttämään hyväkseen monia solujen omia mekanismeja: ne muun muassa pääsevät solujen sisään, monistavat proteiininsa ja kasaavat uudet virukset käyttäen hyväksi solun omia mekanismeja. Virusten perimä koodaa toki muitakin kuin uusien virusten kokoamiseen tarvittavia proteiineja, jotka muokkaavat isäntäsolun toimintaa virukselle suotuisaan suuntaan. Virukset ovat siis oppineet miljoonien tai jopa miljardien vuosien kuluessa paitsi käyttämään hyväksi solujen toimintoja, myös muokkaamaan niitä itselleen hyödylliseen suuntaan, vaikka ne eivät ole edes eläviä! Nykykäsityksen mukaan virukset eivät missään nimessä ole olleet ihmiselle, tai elämälle yleensä, pelkästään haitallisia, vaan ne ovat kulkeneet pitkän evoluution solujen kanssa antaen niille paljon hyödyllisiä ominaisuuksia, joita ilman nykyisen kaltainen elämä ei olisi todennäköisesti edes mahdollista. Merkittävä osa ihmisen perimästä onkin alun perin peräisin viruksilta!

Virusinfektion pääpiirteet riippuvat muutamasta tärkeästä ominaisuudesta: onko viruksen perimä DNA:ta vai RNA:ta, ja onko perimää ympäröivän proteiinikapsidin ympärillä lisäksi lipidivaippa? Nämä tekijät määrittävät sen, miten virus pääsee solun sisälle ja minne sen perimän täytyy solun sisällä päästä pystyäkseen monistumaan ja tuottamaan proteiineja. Vaipalliset virukset pystyvät sulauttamaan oman vaippansa solun vaippaan, jolloin viruksen sisäänpääsy on melko yksinkertaista. Vaipattomilla viruksilla ei ole tällaista mahdollisuutta, vaan niiden täytyy käynnistää endosytoosi-mekanismi, jota solu käyttää normaalisti hyödyllisten aineiden sisäänottoon, ja siirtyä solun sisään sen avulla. Solussa DNA:n kanssa työskentelyyn tarvittavat proteiinit löytyvät tumasta, kun taas RNA:han tarvittavat työkalut sijaitsevat sen solulimassa. Siten viruksen perimä määrittää sen, pystyykö virus aloittamaan monistumisen solulimassa vai täytyykö sen päästä tuman sisään. Usein virus tarvitsee tiettyihin asioihin myös sen omasta perimästä tehtyjä proteiineja. Esimerkiksi, solu ei osaa monistaa RNA:ta mallina olevasta RNA-juosteesta, vaan tarvitsee aina mallikseen DNA-juosteen. Toisin sanoen solu ei osaa monistaa RNA-viruksen perimää, vaan tähän tärkeään tehtävään tarvitaan aina viruksen omasta perimästä muodostettu proteiini.

Vaipattomat enterovirukset pääsevät solujen sisään käyttäen solun endosytoosijärjestelmää ja niiden RNA-perimä monistuu ja tuottaa proteiineja solun sytoplasmassa. Sisäänpääsyn sekä RNA:n monistamisen ja proteiinien tuottamisen välissä on kuitenkin yksi elintärkeä askel: normaalisti hyvin vakaan ja perimää suojaavan viruksen on pystyttävä avautumaan ja vapauttamaan perimä oikeassa paikassa oikeaan aikaan. Vain tällöin viruksen perimä pääsee viruksen soluun tuoman vesikkelin sisältä sytoplasmaan, jossa infektio voi varsinaisesti alkaa.

Tämä väitöskirja koostuu kolmesta osatyöstä. Kahdessa niistä tutkittiin B-ryhmän enterovirusten, echovirus 1 ja coxsackievirus A9, avautumiseen ja perimän vapauttamiseen johtavia tekijöitä: mikä tai mitkä tekijät saavat perimää suojaavan vakaan viruksen avautumaan niin, että se luovuttaa perimänsä oikealla hetkellä. Kolmannessa osatyössä kehitimme valomikroskopiassa käytettäviä uusia fluoresoivia värimolekyylejä, joiden avulla virusinfektion alku ja perimän vapautuminen voidaan tulevaisuudessa kuvantaa elävissä soluissa.

Ensimmäisessä osatyössä löysimme, että kaksi erillistä fysiologista tekijää, albumiini ja ionimuutokset, molemmat muuttavat echovirus 1:n natiivista perusmuotoisesta viruksesta niin kutsutuksi välimuotopartikkeliksi. Näistä tekijöistä albumiini sijaitsee pääosin solujen ulkopuolella, kun taas ionimuutokset oletettavasti tapahtuvat viruksen solun sisään vieneissä vesikkeleissä. Muodostunut, infektioon tarvittava, välimuotoinen virus on valmistautunut aukeamaan, mutta edelleen riittävän vakaa suojatakseen perimää sisällään. Löysimme myös, että riittävän suuret muutokset ympäröivissä ioniolosuhteissa saivat viruksen kokonaan aukeamaan ja perimän vapautumaan. Toisaalta, yhtenä luonnollisena tehtävänään rasvoja sitovan albumiinin aiheuttama välimuotoisen partikkelin muodostuminen pystyttiin estämään rasvahapoilla, joita löydetään myös natiivissa viruskapsidissa sijaitsevasta rasvahappotaskusta. Ratkaisimme myös välimuotoisen viruksen rakenteen ja näimme siinä vastaavanlaisia muutoksia, joita on aiemmin havaittu toisten enterovirusten välimuotopartikkeleilla. Esimerkiksi havaitsimme viruksen proteiinikuoressa tapahtuvan muutoksen, jonka kautta perimän on epäilty poistuvan kapsidin sisältä.

Toisessa osatyössä havaitsimme edellä esiteltyjen tekijöiden, albumiinin ja ionimuutosten, aiheuttavan myös coxsackievirus A9 välimuotoisen partikkelin synnyn. Myös tämä tapahtuma voitiin estää ylimäärällä viruksesta löytyviä rasvahappoja. Lisäksi tutkimme albumiinin ja muuttuneiden ionien erillisiä vaikutuksia tarkemmin. Havaitsimmekin, että tekijät aiheuttivat erilaisen virusrakenteen. Käyttäen sekä rakenteellista että biokemiallista tutkimustietoa arvioimme, että albumiinin aiheuttama rakenne oli kestävämpi, suojaten paremmin viruksen perimää kuin ionien aiheuttama rakenne, joka oli epävakaampi ja lähempänä lopullista perimän vapautumista. Tämä havainto vahvisti hypoteesiamme, jonka mukaan virus voi muuttua välimuotopartikkeliksi jo solun ulkopuolella kohdatessaan albumiinimolekyylejä. Tämän rakenteen pitää kuitenkin olla edelleen hyvin kestävä, ja vasta solun sisällä vesikkeleissä tapahtuvat ionimuutokset saavat viruskapsidin yhä epävakaammaksi mahdollisten perimän vapauttamisen.

Kolmannessa osatyössä ratkaisimme paljon käytetyn fluoresoivan merkkiaineen, SYBR green II rakenteen. Rakenteen avulla kehitimme uuden merkkiai-

neen, MeS:in, jonka fluoresoivat ominaisuudet tutkia viruksen avautumista koeputkessa olivat edeltäjäänsä paremmat. Tämän lisäksi lisäsimme MeS:iin erilaisia kemiallisia ryhmiä, joiden MeS voidaan kiinnittää esimerkiksi viruksen proteiinikuoren pintaan, jonka jälkeen viruksen avautumisen kuvantaminen soluissa on mahdollista.

REFERENCES

Abdelmagid S.A., Clarke S.E., Nielsen D.E., Badawi A., El-Sohemy A., Mutch D.M. & Ma D.W. 2015. Comprehensive profiling of plasma fatty acid concentrations in young healthy Canadian adults. *PLoS One* 10, e0116195.

Babst M. 2011. MVB vesicle formation: ESCRT-dependent, ESCRT-independent and everything in between. *Curr. Opin. Cell Biol.* 23: 452-457.

Baggen J., Thibaut H.J., Strating, J R P M & van Kuppeveld, F J M. 2018. The life cycle of non-polio enteroviruses and how to target it. *Nat. Rev. Microbiol.* 16: 368-381.

Beach L., Schweitzer C. & Scaiano J.C. 2003. Direct determination of single-to-double stranded DNA ratio in solution using steady-state fluorescence measurements. *Org. Biomol. Chem.* 1: 450-451.

Benjin X. & Ling L. 2020. Developments, applications, and prospects of cryo-electron microscopy. *Protein Sci.* 29: 872-882.

Bergelson J.M., Shepley M.P., Chan B.M., Hemler M.E. & Finberg R.W. 1992. Identification of the integrin VLA-2 as a receptor for echovirus 1. *Science* 255: 1718-1720.

Bergelson J.M., Cunningham J.A., Droguett G., Kurt-Jones E.A., Krithivas A., Hong J.S., Horwitz M.S., Crowell R.L. & Finberg R.W. 1997. Isolation of a common receptor for Coxsackie B viruses and adenoviruses 2 and 5. *Science* 275: 1320-1323.

Bishop N.E. & Anderson D.A. 1997. Early interactions of hepatitis A virus with cultured cells: viral elution and the effect of pH and calcium ions. *Arch. Virol.* 142: 2161-2178.

Brandenburg B., Lee L.Y., Lakadamyali M., Rust M.J., Zhuang X. & Hogle J.M. 2007. Imaging poliovirus entry in live cells. *PLoS Biol.* 5, e183.

Bubeck D., Filman D.J., Cheng N., Steven A.C., Hogle J.M. & Belnap D.M. 2005. The structure of the poliovirus 135S cell entry intermediate at 10-angstrom resolution reveals the location of an externalized polypeptide that binds to membranes. *J. Virol.* 79: 7745-7755.

Buchta D., Fuzik T., Hrebik D., Levdansky Y., Sukenik L., Mukhamedova L., Moravcova J., Vacha R. & Plevka P. 2019. Enterovirus particles expel capsid pentamers to enable genome release. *Nat. Commun.* 10: 1138-019.

Butan C., Filman D.J. & Hogle J.M. 2014. Cryo-electron microscopy reconstruction shows poliovirus 135S particles poised for membrane interaction and RNA release. *J. Virol.* 88: 1758-1770.

Carson S.D. & Cole A.J. 2020. Albumin Enhances the Rate at Which Coxsackievirus B3 Strain 28 Converts to A-Particles. *J. Virol.* 94: 10.1128/JVI.01962-19.

Casasnovas J.M. & Springer T.A. 1994. Pathway of rhinovirus disruption by soluble intercellular adhesion molecule 1 (ICAM-1): an intermediate in which ICAM-1 is bound and RNA is released. *J. Virol.* 68: 5882-5889.

Charlton F.W., Hover S., Fuller J., Hewson R., Fontana J., Barr J.N. & Mankouri J. 2019. Cellular cholesterol abundance regulates potassium accumulation

within endosomes and is an important determinant in bunyavirus entry. *J Biol. Chem.* 294: 7335-7347.
Christensen K.A., Myers J.T. & Swanson J.A. 2002. pH-dependent regulation of lysosomal calcium in macrophages. *J. Cell Sci.* 115: 599-607.
Cords C.E., James C.G. & McLaren L.C. 1975. Alteration of capsid proteins of coxsackievirus A13 by low ionic concentrations. *J. Virol.* 15: 244-252.
Cosa G., Focsaneanu K.S., McLean J.R., McNamee J.P. & Scaiano J.C. 2001. Photophysical properties of fluorescent DNA-dyes bound to single- and double-stranded DNA in aqueous buffered solution. *Photochem. Photobiol.* 73: 585-599.
Crowell R.L. & Philipson L. 1971. Specific alterations of coxsackievirus B3 eluted from HeLa cells. *J. Virol.* 8: 509-515.
Curry S., Chow M. & Hogle J.M. 1996. The poliovirus 135S particle is infectious. *J. Virol.* 70: 7125-7131.
Danthi P., Tosteson M., Li Q.H. & Chow M. 2003. Genome delivery and ion channel properties are altered in VP4 mutants of poliovirus. *J. Virol.* 77: 5266-5274.
Davis M., Sagan S.M., Pezacki J.P., Evans D.J. & Simmonds P. 2008. Bioinformatic and physical characterizations of genome-scale ordered RNA structure in mammalian RNA viruses. *J. Virol.* 82: 11824-11836.
De Sena J. & Mandel B. 1977. Studies on the in vitro uncoating of poliovirus. II. Characteristics of the membrane-modified particle. *Virology* 78: 554-566.
Draper D.E. 2004. A guide to ions and RNA structure. *RNA* 10: 335-343.
Enquist L.W. & Editors of the Journal of Virology. 2009. Virology in the 21st century. *J. Virol.* 83: 5296-5308.
Falguieres T., Luyet P.P., Bissig C., Scott C.C., Velluz M.C. & Gruenberg J. 2008. In vitro budding of intralumenal vesicles into late endosomes is regulated by Alix and Tsg101. *Mol. Biol. Cell* 19: 4942-4955.
Fenwick M.L. & Cooper P.D. 1962. Early interactions between poliovirus and ERK cells: some observations on the nature and significance of the rejected particles. *Virology* 18: 212-223.
Filman D.J., Wien M.W., Cunningham J.A., Bergelson J.M. & Hogle J.M. 1998. Structure determination of echovirus 1. *Acta Crystallogr. D Biol. Crystallogr.* 54: 1261-1272.
Frankel E.B. & Audhya A. 2018. ESCRT-dependent cargo sorting at multivesicular endosomes. *Semin. Cell Dev. Biol.* 74: 4-10.
Fricks C.E. & Hogle J.M. 1990. Cell-induced conformational change in poliovirus: externalization of the amino terminus of VP1 is responsible for liposome binding. *J. Virol.* 64: 1934-1945.
Fuchs R. & Blaas D. 2010. Uncoating of human rhinoviruses. *Rev. Med. Virol.* 20: 281-297.
Gerasimenko J.V., Tepikin A.V., Petersen O.H. & Gerasimenko O.V. 1998. Calcium uptake via endocytosis with rapid release from acidifying endosomes. *Curr. Biol.* 8: 1335-1338.
Greve J.M., Forte C.P., Marlor C.W., Meyer A.M., Hoover-Litty H., Wunderlich D. & McClelland A. 1991. Mechanisms of receptor-mediated rhinovirus

neutralization defined by two soluble forms of ICAM-1. *J. Virol.* 65: 6015-6023.
Greve J.M., Davis G., Meyer A.M., Forte C.P., Yost S.C., Marlor C.W., Kamarck M.E. & McClelland A. 1989. The major human rhinovirus receptor is ICAM-1. *Cell* 56: 839-847.
Groppelli E., Levy H.C., Sun E., Strauss M., Nicol C., Gold S., Zhuang X., Tuthill T.J., Hogle J.M. & Rowlands D.J. 2017. Picornavirus RNA is protected from cleavage by ribonuclease during virion uncoating and transfer across cellular and model membranes. *PLoS Pathog.* 13, e1006197.
Gruenberg J. 2020. Life in the lumen: The multivesicular endosome. *Traffic* 21: 76-93.
Hara-Chikuma M., Yang B., Sonawane N.D., Sasaki S., Uchida S. & Verkman A.S. 2005. ClC-3 chloride channels facilitate endosomal acidification and chloride accumulation. *J. Biol. Chem.* 280: 1241-1247.
Heikkila O., Susi P., Stanway G. & Hyypia T. 2009. Integrin alphaVbeta6 is a high-affinity receptor for coxsackievirus A9. *J. Gen. Virol.* 90: 197-204.
Heikkila O., Susi P., Tevaluoto T., Harma H., Marjomaki V., Hyypia T. & Kiljunen S. 2010. Internalization of coxsackievirus A9 is mediated by {beta}2-microglobulin, dynamin, and Arf6 but not by caveolin-1 or clathrin. *J. Virol.* 84: 3666-3681.
Helenius A. 2020. Standing on the Shoulders of Viruses. *Annu. Rev. Biochem.* 89: 21-43.
Helenius A. 2018. Virus Entry: Looking Back and Moving Forward. *J. Mol. Biol.* 430: 1853-1862.
Helenius A., Mellman I., Wall D. & Hubbard A. 1983. Endosomes. *Trends Biochem. Sci.* 8: 245.
Hewat E.A. & Blaas D. 2004. Cryoelectron microscopy analysis of the structural changes associated with human rhinovirus type 14 uncoating. *J. Virol.* 78: 2935-2942.
Hober D. & Sauter P. 2010. Pathogenesis of type 1 diabetes mellitus: interplay between enterovirus and host. *Nat. Rev. Endocrinol.* 6: 279-289.
Hofer F., Gruenberger M., Kowalski H., Machat H., Huettinger M., Kuechler E. & Blaas D. 1994. Members of the low density lipoprotein receptor family mediate cell entry of a minor-group common cold virus. *Proc. Natl. Acad. Sci. U S A* 91: 1839-1842.
Hover S., Foster B., Fontana J., Kohl A., Goldstein S.A.N., Barr J.N. & Mankouri J. 2018. Bunyavirus requirement for endosomal K+ reveals new roles of cellular ion channels during infection. *PLoS Pathog.* 14, e1006845.
Huang Y., Hogle J.M. & Chow M. 2000. Is the 135S poliovirus particle an intermediate during cell entry? *J. Virol.* 74: 8757-8761.
Hull R. 1978. The stabilization of the particles of turnip rosette virus. III. Divalent cations. *Virology* 89: 418-422.
Huttunen M., Waris M., Kajander R., Hyypia T. & Marjomaki V. 2014. Coxsackievirus A9 infects cells via nonacidic multivesicular bodies. *J. Virol.* 88: 5138-5151.
Hyoty H. 2016. Viruses in type 1 diabetes. *Pediatr. Diabetes* 17 Suppl 22: 56-64.

Ihmels H., Faulhaber K., Vedaldi D., Dall'Acqua F. & Viola G. 2005. Intercalation of organic dye molecules into double-stranded DNA. Part 2: the annelated quinolizinium ion as a structural motif in DNA intercalators. *Photochem. Photobiol.* 81: 1107-1115.

Jokinen J., White D.J., Salmela M., Huhtala M., Kapyla J., Sipila K., Puranen J.S., Nissinen L., Kankaanpaa P., Marjomaki V., Hyypia T., Johnson M.S. & Heino J. 2010. Molecular mechanism of alpha2beta1 integrin interaction with human echovirus 1. *EMBO J.* 29: 196-208.

Kahrs C.R., Chuda K., Tapia G., Stene L.C., Marild K., Rasmussen T., Ronningen K.S., Lundin K.E.A., Kramna L., Cinek O. & Stordal K. 2019. Enterovirus as trigger of coeliac disease: nested case-control study within prospective birth cohort. *BMJ.* 364: l231.

Kaplan G., Freistadt M.S. & Racaniello V.R. 1990. Neutralization of poliovirus by cell receptors expressed in insect cells. *J. Virol.* 64: 4697-4702.

Karimi M., Bahrami S., Ravari S.B., Zangabad P.S., Mirshekari H., Bozorgomid M., Shahreza S., Sori M. & Hamblin M.R. 2016. Albumin nanostructures as advanced drug delivery systems. *Expert Opin. Drug Deliv.* 13: 1609-1623.

Karjalainen M., Rintanen N., Lehkonen M., Kallio K., Maki A., Hellstrom K., Siljamaki V., Upla P. & Marjomaki V. 2011. Echovirus 1 infection depends on biogenesis of novel multivesicular bodies. *Cell Microbiol.* 13: 1975-1995.

Karjalainen M., Kakkonen E., Upla P., Paloranta H., Kankaanpaa P., Liberali P., Renkema G.H., Hyypia T., Heino J. & Marjomaki V. 2008. A Raft-derived, Pak1-regulated entry participates in alpha2beta1 integrin-dependent sorting to caveosomes. *Mol. Biol. Cell.* 19: 2857-2869.

Karunakaran V., Perez Lustres J.L., Zhao L., Ernsting N.P. & Seitz O. 2006. Large dynamic Stokes shift of DNA intercalation dye Thiazole Orange has contribution from a high-frequency mode. *J. Am. Chem. Soc.* 128: 2954-2962.

Korant B.D., Lonberg-Holm K., Noble J. & Stasny J.T. 1972. Naturally occurring and artificially produced components of three rhinoviruses. *Virology* 48: 71-86.

Laitinen O.H., Honkanen H., Pakkanen O., Oikarinen S., Hankaniemi M.M., Huhtala H., Ruokoranta T., Lecouturier V., Andre P., Harju R., Virtanen S.M., Lehtonen J., Almond J.W., Simell T., Simell O., Ilonen J., Veijola R., Knip M. & Hyoty H. 2014. Coxsackievirus B1 is associated with induction of beta-cell autoimmunity that portends type 1 diabetes. *Diabetes* 63: 446-455.

Lee H., Shingler K.L., Organtini L.J., Ashley R.E., Makhov A.M., Conway J.F. & Hafenstein S. 2016. The novel asymmetric entry intermediate of a picornavirus captured with nanodiscs. *Sci. Adv.* 2, e1501929.

Liu Y., Sheng J., van Vliet, A L W, Buda G., van Kuppeveld, F J M & Rossmann M.G. 2018. Molecular basis for the acid-initiated uncoating of human enterovirus D68. *Proc. Natl. Acad. Sci. U S A* 115, E12209-E12217.

Lonberg-Holm K. & Korant B.D. 1972. Early interaction of rhinoviruses with host cells. *J. Virol.* 9: 29-40.

Lonberg-Holm K., Gosser L.B. & Shimshick E.J. 1976. Interaction of liposomes with subviral particles of poliovirus type 2 and rhinovirus type 2. *J. Virol.* 19: 746-749.

Lonberg-Holm K., Gosser L.B. & Kauer J.C. 1975. Early alteration of poliovirus in infected cells and its specific inhibition. *J. Gen. Virol.* 27: 329-342.

Marjomaki V., Turkki P. & Huttunen M. 2015. Infectious Entry Pathway of Enterovirus B Species. *Viruses* 7: 6387-6399.

Marjomaki V., Pietiainen V., Matilainen H., Upla P., Ivaska J., Nissinen L., Reunanen H., Huttunen P., Hyypia T. & Heino J. 2002. Internalization of echovirus 1 in caveolae. *J. Virol.* 76: 1856-1865.

Martikainen M., Salorinne K., Lahtinen T., Malola S., Permi P., Hakkinen H. & Marjomaki V. 2015. Hydrophobic pocket targeting probes for enteroviruses. *Nanoscale* 7: 17457-17467.

Mendelsohn C.L., Wimmer E. & Racaniello V.R. 1989. Cellular receptor for poliovirus: molecular cloning, nucleotide sequence, and expression of a new member of the immunoglobulin superfamily. *Cell* 56: 855-865.

Merilahti P., Koskinen S., Heikkila O., Karelehto E. & Susi P. 2012. Endocytosis of integrin-binding human picornaviruses. *Adv. Virol.* 2012: 547530.

Mirmomeni M.H., Hughes P.J. & Stanway G. 1997. An RNA tertiary structure in the 3' untranslated region of enteroviruses is necessary for efficient replication. *J. Virol.* 71: 2363-2370.

Morosky S., Wells A.I., Lemon K., Evans A.S., Schamus S., Bakkenist C.J. & Coyne C.B. 2019. The neonatal Fc receptor is a pan-echovirus receptor. *Proc. Natl. Acad. Sci. U S A* 116: 3758-3763.

Myllynen M., Kazmertsuk A. & Marjomaki V. 2016. A Novel Open and Infectious Form of Echovirus 1. *J. Virol.* 90: 6759-6770.

Noble-Harvey J. & Lonberg-Holm K. 1974. Sequential steps in attachment of human rhinovirus type 2 to HeLa cells. *J. Gen. Virol.* 25: 83-91.

Organtini L.J., Makhov A.M., Conway J.F., Hafenstein S. & Carson S.D. 2014. Kinetic and structural analysis of coxsackievirus B3 receptor interactions and formation of the A-particle. *J. Virol.* 88: 5755-5765.

Penn A.H., Dubick M.A. & Torres Filho I.P. 2017. Fatty Acid Saturation of Albumin Used in Resuscitation Fluids Modulates Cell Damage in Shock: in vitro Results Using a Novel Technique to Measure Fatty Acid Binding Capacity. *Shock* 48: 449-458.

Pfeiffer P., Herzog M. & Hirth L. 1976. RNA viruses: stabilization of brome mosaic virus. *Philos. Trans. R Soc. Lond. B Biol. Sci.* 276: 99-107.

Pickl-Herk A., Luque D., Vives-Adrian L., Querol-Audi J., Garriga D., Trus B.L., Verdaguer N., Blaas D. & Caston J.R. 2013. Uncoating of common cold virus is preceded by RNA switching as determined by X-ray and cryo-EM analyses of the subviral A-particle. *Proc. Natl. Acad. Sci. U S A* 110: 20063-20068.

Pietiainen V.M., Marjomaki V., Heino J. & Hyypia T. 2005. Viral entry, lipid rafts and caveosomes. *Ann. Med.* 37: 394-403.

Prchla E., Kuechler E., Blaas D. & Fuchs R. 1994. Uncoating of human rhinovirus serotype 2 from late endosomes. *J. Virol.* 68: 3713-3723.

Punch E.K., Hover S., Blest H.T.W., Fuller J., Hewson R., Fontana J., Mankouri J. & Barr J.N. 2018. Potassium is a trigger for conformational change in the fusion spike of an enveloped RNA virus. *J. Biol. Chem.* 293: 9937-9944.

Raiborg C., Bache K.G., Gillooly D.J., Madshus I.H., Stang E. & Stenmark H. 2002. Hrs sorts ubiquitinated proteins into clathrin-coated microdomains of early endosomes. *Nat. Cell Biol.* 4: 394-398.

Ren J., Wang X., Zhu L., Hu Z., Gao Q., Yang P., Li X., Wang J., Shen X., Fry E.E., Rao Z. & Stuart D.I. 2015. Structures of Coxsackievirus A16 Capsids with Native Antigenicity: Implications for Particle Expansion, Receptor Binding, and Immunogenicity. *J. Virol.* 89: 10500-10511.

Ren J., Wang X., Hu Z., Gao Q., Sun Y., Li X., Porta C., Walter T.S., Gilbert R.J., Zhao Y., Axford D., Williams M., McAuley K., Rowlands D.J., Yin W., Wang J., Stuart D.I., Rao Z. & Fry E.E. 2013. Picornavirus uncoating intermediate captured in atomic detail. *Nat. Commun.* 4: 1929.

Rintanen N., Karjalainen M., Alanko J., Paavolainen L., Maki A., Nissinen L., Lehkonen M., Kallio K., Cheng R.H., Upla P., Ivaska J. & Marjomaki V. 2012. Calpains promote alpha2beta1 integrin turnover in nonrecycling integrin pathway. *Mol. Biol. Cell* 23: 448-463.

Roivainen M. 1999. Enteroviruses and myocardial infarction. *Am. Heart J.* 138: S479-83.

Roivainen M., Alfthan G., Jousilahti P., Kimpimaki M., Hovi T. & Tuomilehto J. 1998. Enterovirus infections as a possible risk factor for myocardial infarction. *Circulation* 98: 2534-2537.

Roivainen M., Piirainen L., Hovi T., Virtanen I., Riikonen T., Heino J. & Hyypia T. 1994. Entry of coxsackievirus A9 into host cells: specific interactions with alpha v beta 3 integrin, the vitronectin receptor. *Virology* 203: 357-365.

Rossmann M.G., He Y. & Kuhn R.J. 2002. Picornavirus-receptor interactions. *Trends Microbiol.* 10: 324-331.

Schneider-Schaulies J. 2000. Cellular receptors for viruses: links to tropism and pathogenesis. *J. Gen. Virol.* 81: 1413-1429.

Scott C.C. & Gruenberg J. 2011. Ion flux and the function of endosomes and lysosomes: pH is just the start: the flux of ions across endosomal membranes influences endosome function not only through regulation of the luminal pH. *Bioessays* 33: 103-110.

Shafren D.R., Bates R.C., Agrez M.V., Herd R.L., Burns G.F. & Barry R.D. 1995. Coxsackieviruses B1, B3, and B5 use decay accelerating factor as a receptor for cell attachment. *J. Virol.* 69: 3873-3877.

Shah P.N.M., Filman D.J., Karunatilaka K.S., Hesketh E.L., Groppelli E., Strauss M. & Hogle J.M. 2020. Cryo-EM structures reveal two distinct conformational states in a picornavirus cell entry intermediate. *bioRxiv* 2020.01.08.899112.

Shakeel S., Seitsonen J.J., Kajander T., Laurinmaki P., Hyypia T., Susi P. & Butcher S.J. 2013. Structural and functional analysis of coxsackievirus A9 integrin alphavbeta6 binding and uncoating. *J. Virol.* 87: 3943-3951.

Sherman M.B., Guenther R.H., Tama F., Sit T.L., Brooks C.L., Mikhailov A.M., Orlova E.V., Baker T.S. & Lommel S.A. 2006. Removal of divalent cations

induces structural transitions in red clover necrotic mosaic virus, revealing a potential mechanism for RNA release. *J. Virol.* 80: 10395-10406.

Shingler K.L., Yoder J.L., Carnegie M.S., Ashley R.E., Makhov A.M., Conway J.F. & Hafenstein S. 2013. The enterovirus 71 A-particle forms a gateway to allow genome release: a cryoEM study of picornavirus uncoating. *PLoS Pathog.* 9, e1003240.

Siljamaki E., Rintanen N., Kirsi M., Upla P., Wang W., Karjalainen M., Ikonen E. & Marjomaki V. 2013. Cholesterol dependence of collagen and echovirus 1 trafficking along the novel alpha2beta1 integrin internalization pathway. *PLoS One* 8, e55465.

Simmonds P., Tuplin A. & Evans D.J. 2004. Detection of genome-scale ordered RNA structure (GORS) in genomes of positive-stranded RNA viruses: Implications for virus evolution and host persistence. *RNA* 10: 1337-1351.

Smyth M., Pettitt T., Symonds A. & Martin J. 2003. Identification of the pocket factors in a picornavirus. *Arch. Virol.* 148: 1225-1233.

Sonawane N.D., Thiagarajah J.R. & Verkman A.S. 2002. Chloride concentration in endosomes measured using a ratioable fluorescent Cl- indicator: evidence for chloride accumulation during acidification. *J. Biol. Chem.* 277: 5506-5513.

Soonsawad P., Paavolainen L., Upla P., Weerachatyanukul W., Rintanen N., Espinoza J., McNerney G., Marjomaki V. & Cheng R.H. 2014. Permeability changes of integrin-containing multivesicular structures triggered by picornavirus entry. *PLoS One* 9, e108948.

Staring J., von Castelmur E., Blomen V.A., van den Hengel, L G, Brockmann M., Baggen J., Thibaut H.J., Nieuwenhuis J., Janssen H., van Kuppeveld F.J., Perrakis A., Carette J.E. & Brummelkamp T.R. 2017. PLA2G16 represents a switch between entry and clearance of Picornaviridae. *Nature* 541: 412-416.

Stauffer S., Feng Y., Nebioglu F., Heilig R., Picotti P. & Helenius A. 2014. Stepwise priming by acidic pH and a high K+ concentration is required for efficient uncoating of influenza A virus cores after penetration. *J. Virol.* 88: 13029-13046.

Staunton D.E., Merluzzi V.J., Rothlein R., Barton R., Marlin S.D. & Springer T.A. 1989. A cell adhesion molecule, ICAM-1, is the major surface receptor for rhinoviruses. *Cell* 56: 849-853.

Steinberg B.E., Huynh K.K., Brodovitch A., Jabs S., Stauber T., Jentsch T.J. & Grinstein S. 2010. A cation counterflux supports lysosomal acidification. *J. Cell Biol.* 189: 1171-1186.

Strauss M., Schotte L., Karunatilaka K.S., Filman D.J. & Hogle J.M. 2017. Cryo-electron Microscopy Structures of Expanded Poliovirus with VHHs Sample the Conformational Repertoire of the Expanded State. *J. Virol.* 91: 10.1128/JVI.01443-16.

Strauss M., Filman D.J., Belnap D.M., Cheng N., Noel R.T. & Hogle J.M. 2015. Nectin-like interactions between poliovirus and its receptor trigger conformational changes associated with cell entry. *J. Virol.* 89: 4143-4157.

Toh W.H., Louber J., Mahmoud I.S., Chia J., Bass G.T., Dower S.K., Verhagen A.M. & Gleeson P.A. 2019. FcRn mediates fast recycling of endocytosed

albumin and IgG from early macropinosomes in primary macrophages. *J. Cell Sci.* 133: 10.1242/jcs.235416.

Tosteson M.T. & Chow M. 1997. Characterization of the ion channels formed by poliovirus in planar lipid membranes. *J. Virol.* 71: 507-511.

Trigatti B.L. & Gerber G.E. 1995. A direct role for serum albumin in the cellular uptake of long-chain fatty acids. *Biochem. J.* 308 (Pt 1): 155-159.

Tuthill T.J., Groppelli E., Hogle J.M. & Rowlands D.J. 2010. Picornaviruses. *Curr. Top. Microbiol. Immunol.* 343: 43-89.

Upla P., Marjomaki V., Kankaanpaa P., Ivaska J., Hyypia T., Van Der Goot, F G & Heino J. 2004. Clustering induces a lateral redistribution of alpha 2 beta 1 integrin from membrane rafts to caveolae and subsequent protein kinase C-dependent internalization. *Mol. Biol. Cell* 15: 625-636.

van der Vusse, G J. 2009. Albumin as fatty acid transporter. *Drug Metab Pharmacokinet.* 24: 300-307.

Walter T.S., Ren J., Tuthill T.J., Rowlands D.J., Stuart D.I. & Fry E.E. 2012. A plate-based high-throughput assay for virus stability and vaccine formulation. *J. Virol. Methods* 185: 166-170.

Wang X., Peng W., Ren J., Hu Z., Xu J., Lou Z., Li X., Yin W., Shen X., Porta C., Walter T.S., Evans G., Axford D., Owen R., Rowlands D.J., Wang J., Stuart D.I., Fry E.E. & Rao Z. 2012. A sensor-adaptor mechanism for enterovirus uncoating from structures of EV71. *Nat. Struct. Mol. Biol.* 19: 424-429.

Ward T., Powell R.M., Evans D.J. & Almond J.W. 1999. Serum albumin inhibits echovirus 7 uncoating. *J. Gen. Virol.* 80 (Pt 2): 283-290.

Ward T., Powell R.M., Chaudhry Y., Meredith J., Almond J.W., Kraus W., Nelsen-Salz B., Eggers H.J. & Evans D.J. 2000. Fatty acid-depleted albumin induces the formation of echovirus A particles. *J. Virol.* 74: 3410-3412.

Weinert S., Jabs S., Supanchart C., Schweizer M., Gimber N., Richter M., Rademann J., Stauber T., Kornak U. & Jentsch T.J. 2010. Lysosomal pathology and osteopetrosis upon loss of H+-driven lysosomal Cl- accumulation. *Science* 328: 1401-1403.

Wetz K. & Kucinski T. 1991. Influence of different ionic and pH environments on structural alterations of poliovirus and their possible relation to virus uncoating. *J. Gen. Virol.* 72 (Pt 10): 2541-2544.

Williams C.H., Kajander T., Hyypia T., Jackson T., Sheppard D. & Stanway G. 2004. Integrin alpha v beta 6 is an RGD-dependent receptor for coxsackievirus A9. *J. Virol.* 78: 6967-6973.

Witte R., Andriasyan V., Georgi F., Yakimovich A. & Greber U.F. 2018. Concepts in Light Microscopy of Viruses. *Viruses* 10: 10.3390/v10040202.

Witwer C., Rauscher S., Hofacker I.L. & Stadler P.F. 2001. Conserved RNA secondary structures in Picornaviridae genomes. *Nucleic Acids Res.* 29: 5079-5089.

Xing L., Huhtala M., Pietiainen V., Kapyla J., Vuorinen K., Marjomaki V., Heino J., Johnson M.S., Hyypia T. & Cheng R.H. 2004. Structural and functional analysis of integrin alpha2I domain interaction with echovirus 1. *J. Biol. Chem.* 279: 11632-11638.

Yamauchi Y. & Greber U.F. 2016. Principles of Virus Uncoating: Cues and the Snooker Ball. *Traffic* 17: 569-592.

Yamayoshi S., Yamashita Y., Li J., Hanagata N., Minowa T., Takemura T. & Koike S. 2009. Scavenger receptor B2 is a cellular receptor for enterovirus 71. *Nat. Med.* 15: 798-801.

Zell R. 2018. Picornaviridae-the ever-growing virus family. *Arch. Virol.* 163: 299-317.

Zhao X., Zhang G., Liu S., Chen X., Peng R., Dai L., Qu X., Li S., Song H., Gao Z., Yuan P., Liu Z., Li C., Shang Z., Li Y., Zhang M., Qi J., Wang H., Du N., Wu Y., Bi Y., Gao S., Shi Y., Yan J., Zhang Y., Xie Z., Wei W. & Gao G.F. 2019. Human Neonatal Fc Receptor Is the Cellular Uncoating Receptor for Enterovirus B. *Cell* 177: 1553-1565.e16.

Zipper H., Brunner H., Bernhagen J. & Vitzthum F. 2004. Investigations on DNA intercalation and surface binding by SYBR Green I, its structure determination and methodological implications. *Nucleic Acids Res.* 32, e103.

ORIGINAL PAPERS

I

EXTRACELLULAR ALBUMIN AND ENDOSOMAL IONS PRIME ENTEROVIRUS PARTICLES FOR UNCOATING THAT CAN BE PREVENTED BY FATTY ACID SATURATION

by

Ruokolainen V., Domanska A., Laajala M., Pelliccia M.,
Butcher S. J. & Marjomäki V. 2019

Journal of Virology 93 (17) e00599-19

https://doi.org/10.1128/JVI.00599-19

AMERICAN SOCIETY FOR MICROBIOLOGY | Journal of Virology®

VIRUS-CELL INTERACTIONS

Extracellular Albumin and Endosomal Ions Prime Enterovirus Particles for Uncoating That Can Be Prevented by Fatty Acid Saturation

Visa Ruokolainen,[a] Aušra Domanska,[b] Mira Laajala,[a] Maria Pelliccia,[c] Sarah J. Butcher,[b] Varpu Marjomäki[a]

[a]Department of Biological and Environmental Science, Nanoscience Center, University of Jyväskylä, Jyväskylä, Finland

[b]Faculty of Biological and Environmental Sciences, Molecular and Integrative Bioscience Research Programme, and Helsinki Institute of Life Sciences, Institute of Biotechnology, University of Helsinki, Helsinki, Finland

[c]European School of Molecular Medicine (SEMM), IFOM-IEO-Campus, Milan, Italy

ABSTRACT There is limited information about the molecular triggers leading to the uncoating of enteroviruses under physiological conditions. Using real-time spectroscopy and sucrose gradients with radioactively labeled virus, we show at 37°C, the formation of albumin-triggered, metastable uncoating intermediate of echovirus 1 without receptor engagement. This conversion was blocked by saturating the albumin with fatty acids. High potassium but low sodium and calcium concentrations, mimicking the endosomal environment, also induced the formation of a metastable uncoating intermediate of echovirus 1. Together, these factors boosted the formation of the uncoating intermediate, and the infectivity of this intermediate was retained, as judged by end-point titration. Cryo-electron microscopy reconstruction of the virions treated with albumin and high potassium, low sodium, and low calcium concentrations resulted in a 3.6-Å resolution model revealing a fenestrated capsid showing 4% expansion and loss of the pocket factor, similarly to altered (A) particles described for other enteroviruses. The dimer interface between VP2 molecules was opened, the VP1 N termini disordered and most likely externalized. The RNA was clearly visible, anchored to the capsid. The results presented here suggest that extracellular albumin, partially saturated with fatty acids, likely leads to the formation of the infectious uncoating intermediate prior to the engagement with the cellular receptor. In addition, changes in mono- and divalent cations, likely occurring in endosomes, promote capsid opening and genome release.

IMPORTANCE There is limited information about the uncoating of enteroviruses under physiological conditions. Here, we focused on physiologically relevant factors that likely contribute to opening of echovirus 1 and other B-group enteroviruses. By combining biochemical and structural data, we show that, before entering cells, extracellular albumin is capable of priming the virus into a metastable yet infectious intermediate state. The ionic changes that are suggested to occur in endosomes can further contribute to uncoating and promote genome release, once the viral particle is endocytosed. Importantly, we provide a detailed high-resolution structure of a virion after treatment with albumin and a preset ion composition, showing pocket factor release, capsid expansion, and fenestration and the clearly visible genome still anchored to the capsid. This study provides valuable information about the physiological factors that contribute to the opening of B group enteroviruses.

KEYWORDS cryoEM structure, albumin, biochemistry, enterovirus, fatty acids, ions, uncoating, virology

Citation Ruokolainen V, Domanska A, Laajala M, Pelliccia M, Butcher SJ, Marjomäki V. 2019. Extracellular albumin and endosomal ions prime enterovirus particles for uncoating that can be prevented by fatty acid saturation. J Virol 93:e00599-19. https://doi.org/10.1128/JVI.00599-19.

Editor Susana López, Instituto de Biotecnologia/UNAM

Address correspondence to Varpu Marjomäki, varpu.s.marjomaki@jyu.fi.

V.R. and A.D. contributed equally to this article.

Received 10 April 2019
Accepted 31 May 2019
Accepted manuscript posted online 12 June 2019
Published 13 August 2019

The Enterovirus B species consists of tens of clinically relevant viruses, including over 30 serotypes of echoviruses and coxsackievirus B1 to B6 and A9. They can cause a wide variety of mild and severe infections, and many of them are also associated with the onset of type I diabetes and coeliac disease (1–4). These viruses infect primarily gut epithelial cells and are naturally stabile in an acidic environment. The latter important feature makes the enterovirus B (EV-B) group viruses different from, for example, rhinoviruses that are known to rely on acidification during virus uncoating (5, 6).

Earlier, we showed that echovirus 1 (E1) and coxsackievirus A9 trigger a clathrin-independent entry pathway (7–10). Within 15 min of entry, viruses are first localized in the endosomes that develop into pH-neutral multivesicular bodies. The genome uncoating continues for up to 2 h postinfection (8, 11, 12). A large number of host cell factors have been pinpointed as important regulators for the entry of enteroviruses (13). However, there is very little information on the possible extracellular and cointernalized soluble factors that potentially contribute to uncoating during infection.

Recently, we described a novel uncoating intermediate particle of E1 which formed during infection and could be isolated from the cells at early stages of infection (14). This particle proved to be stable, infectious, containing all of its capsid proteins, and still capable of receptor binding (14). Previously, several studies characterized uncoating intermediates for entero- and rhinoviruses that have been termed as A- or 135S-particles based on their altered conformation and lighter sedimentation in sucrose gradients (15). The formation of these particles has been suggested to be induced by receptor binding (16, 17), low pH (18), or by nonphysiological high temperatures (19). They have also been found to exist in purified virus preparations (20). One study showed that treatment with fatty acid-free bovine serum albumin (BSA) converts echovirus 12 into A-particles, but the mechanism of action was not investigated further (21). In addition, there are only few studies reporting what effects other physiological factors, such as changes in ionic conditions, may have on the virus particle (21–25). X-ray crystallography as well as cryo-electron microscopy (cryoEM) and single particle reconstruction have been used to gain structural information on picornavirus particles at different stages before genome release (20, 26–33). Due to methodological challenges, it has been difficult to exactly map the spatiotemporal events during the uncoating process and to link that to structural information. Furthermore, the physiological conditions in the tissues where virus infection takes place have not been carefully studied.

Here we show that albumin triggers the uncoating process of E1 at 37°C, in a manner dependent upon the balance between fatty acids and albumin present. We further show that changes in mono- and divalent cations, likely reflecting the endosomal concentrations, also trigger a slower uncoating process of E1, which is clearly boosted by albumin.

RESULTS

Serum at physiological temperature drives transformation from intact E1 virion to an uncoating intermediate. In this study, we investigated physiologically relevant factors that promote the uncoating process of E1. First, we noticed that in phosphate-buffered saline (PBS), E1 remained infectious up to 21 days at room temperature, and remarkably, at 37°C, still some virus stayed infectious under such conditions after 5 days (Fig. 1A). A 3-h incubation of E1 in PBS-$MgCl_2$ at 37°C resulted in only a minor formation of empty virus particles and no formation of the uncoating intermediate, as detected by real-time fluorescence measurement in the presence or absence of RNase (Fig. 1B). This finding was further confirmed by gradient centrifugation of ^{35}S-labeled E1 (Fig. 1C). The virus was even more stable in DPBS buffer (PBS containing also $CaCl_2$) (for buffer compositions see Table 1) throughout the 3-h treatment (Fig. 1B). If enteroviruses are so stable, what molecules efficiently trigger uncoating in the right location, i.e., endosomes? We observed that conversion of E1 virions to intermediate particles was significantly enhanced by treating the virus with cell culture medium containing 1% serum (1% S-MEM): the SYBR green II fluorescence increased considerably after a 10- to 15-min incubation at

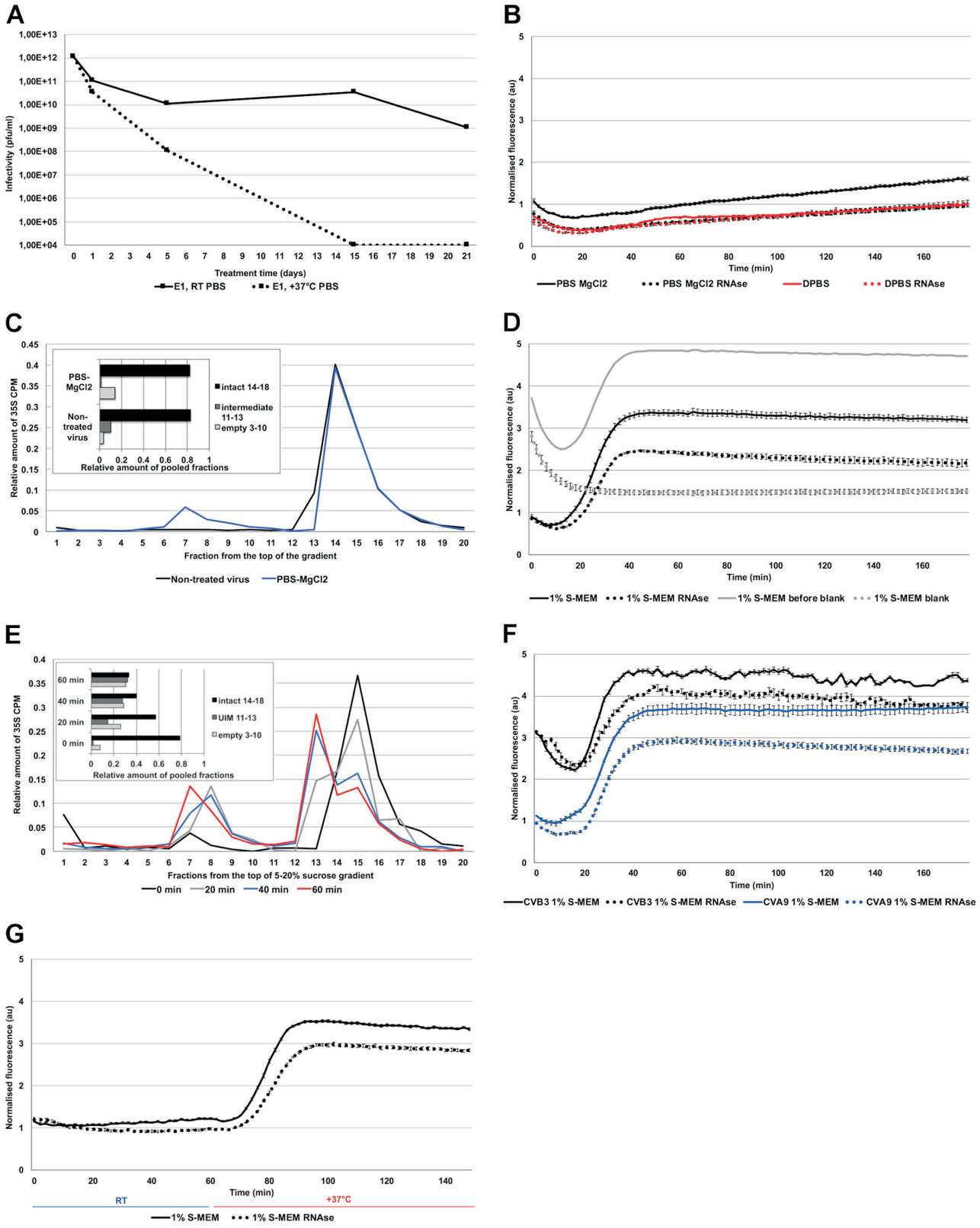

FIG 1 Echovirus 1 stability. (A) Infectivity of E1 after 1, 5, 15, or 21 days in PBS at 37°C or room temperature. (B) Fluorescence measurement of SYBR green II (SGII) dye in the presence of 1 μg E1 in PBS-$MgCl_2$ and DPBS with or without RNase during 3 h at 37°C. (C) Sucrose gradient (5% to 20%) separation of ^{35}S-labeled

(Continued on next page)

TABLE 1 Exact compositions of the buffers used in the paper

Buffer or compound	Concn (mM)										
	NaCl	Na_2HPO_4	Total Na	KCl	KH_2PO_4	K_2HPO_4	Total K	$MgCl_2$	$CaCl_2$	faf-BSA (%)	pH
PBS	137	8	145	3	2		5				7.34
PBS-$MgCl_2$	137	8	145	3	2		5	2			7.22
DPBS	138	8.1	146.1	2.7	1.5		4.2	0.5	0.9		7.25
NKMC	20		20		6	12	30	0.5	0.2		7.18
NK	20		20		6	12	30				7.25
EM buffer	29		29		5.6	11.2	28	0.145		0.0093	7.28

37°C, reaching maximal fluorescence around 40 to 50 min (Fig. 1D). At 45 min, approximately 68% of the intensity originated from intermediate particles and 32% from empty capsids (Fig. 1D). The increase of both forms was again confirmed by sucrose gradient centrifugation using ^{35}S E1 (Fig. 1E). A similar effect was also observed by fluorescence measurements of coxsackievirus B3 and coxsackievirus A9 (Fig. 1F), suggesting that this phenomenon was not restricted to E1. Virus conversion to the intermediate form was strictly temperature dependent, as 1% S-MEM did not induce changes in the virus capsid at room temperature but did induce the formation quickly after raising the temperature to 37°C (Fig. 1G). Altogether, these results show that while E1 is stable in physiological buffers, 1% bovine serum effectively induces formation of the uncoating intermediate and empty capsids at 37°C.

Ion composition mimicking endosomal conditions also triggers the E1 uncoating process. Uncoating of E1 and coxsackievirus A9 is known to be independent of endosome acidification (13), which suggests that ion concentrations other than H^+, such as K^+, Na^+, Mg^{2+}, and Ca^{2+}, might be more important for E1 uncoating inside the endosomes. We thus chose a combination of ion concentrations based on the measurements made from endosomes (34–38) and the information provided by Scott and Gruenberg in their review on endosomal ionic conditions (39) and tested their effect on promoting E1 uncoating. The "endosomal ionic solution" used in this study contained 20 mM NaCl, 30 mM K^+, 0.5 mM $MgCl_2$, and 0.2 mM $CaCl_2$ and is referred to as NKMC. The spectroscopy results showed that the hypotonic NKMC solution promoted a slow formation of the uncoating intermediate within a 3-h period at 37°C, as detected by the gradual increase of fluorescence to a roughly 4-times higher level when normalized to that of the DPBS treatment (Fig. 2A). Therefore, NKMC facilitates the formation of mainly porous particles, most of which still contain RNA. Increasing the concentration of K^+ (60 mM) in relation to Na^+ (20 mM) appeared to promote RNA release, suggesting that the increase of K^+ found in the endosomes may be an important factor to promote the final RNA release (Fig. 2A). We also found a larger amount of RNA released when we omitted the divalent cations from the buffer (i.e., NK solution containing 20 mM NaCl and 30 mM K^+ without Mg^{2+} or Ca^{2+}). Without Mg^{2+} or Ca^{2+}, the fluorescence signal mainly comprised released RNA, indicating the presence of mainly empty capsids (Fig. 2A). This is in line with the previously observed stabilizing effect of divalent cations on viral particles (24, 40–45). The stabilizing effect of divalent cations was further verified by complementing the NK solution with different concentrations of Ca^{2+} or Mg^{2+} ions.

FIG 1 Legend (Continued)
E1 when treated for 1 h at 37 °C in PBS-$MgCl_2$ versus nontreated virus at 4°C in PBS-$MgCl_2$. The amounts of different virus populations are shown in the inset. (D) Fluorescence measurement of SGII dye in the presence of 1 μg E1 in 1% S-MEM at 37°C. In gray, as an example, results of the same virus measurements before and subtracting the blank measurements. In the presented results of 1% S-MEM, and in all of the presented fluorescence results in this paper, the blank, which contains all other factors except the virus (gray dotted lines), is subtracted from the measurement with virus (gray solid lines). (E) Sucrose gradient (5% to 20%) separation of ^{35}S-labeled E1 when treated for 0 to 60 min at 37°C in 1% S-MEM. The amounts of different virus populations are shown in the inset. (F) Fluorescence measurements of SGII dye in the presence of 1 μg of CVB3 or CVA9 in 1% MEM at 37°C during 3 h. (G) Fluorescence measurements of SGII dye in the presence of 1 μg E1 in 1% S-MEM at room temperature (23°C) for 60 min after which the multilabel reader heater was turned to 37°C for 90 min. The transition from room temperature to 37°C lasted about 12 min. In all of the fluorescence measurements, in this and other figures, the *y* axes are normalized to the final fluorescence values of the control DPBS treatment (panel B, red solid line). Treatments in each buffer with and without RNase are marked with the same colors but with dotted and solid lines, respectively. All fluorescence measurements are averages from a minimum of five measurements and the presented error bars are ± standard errors of the means.

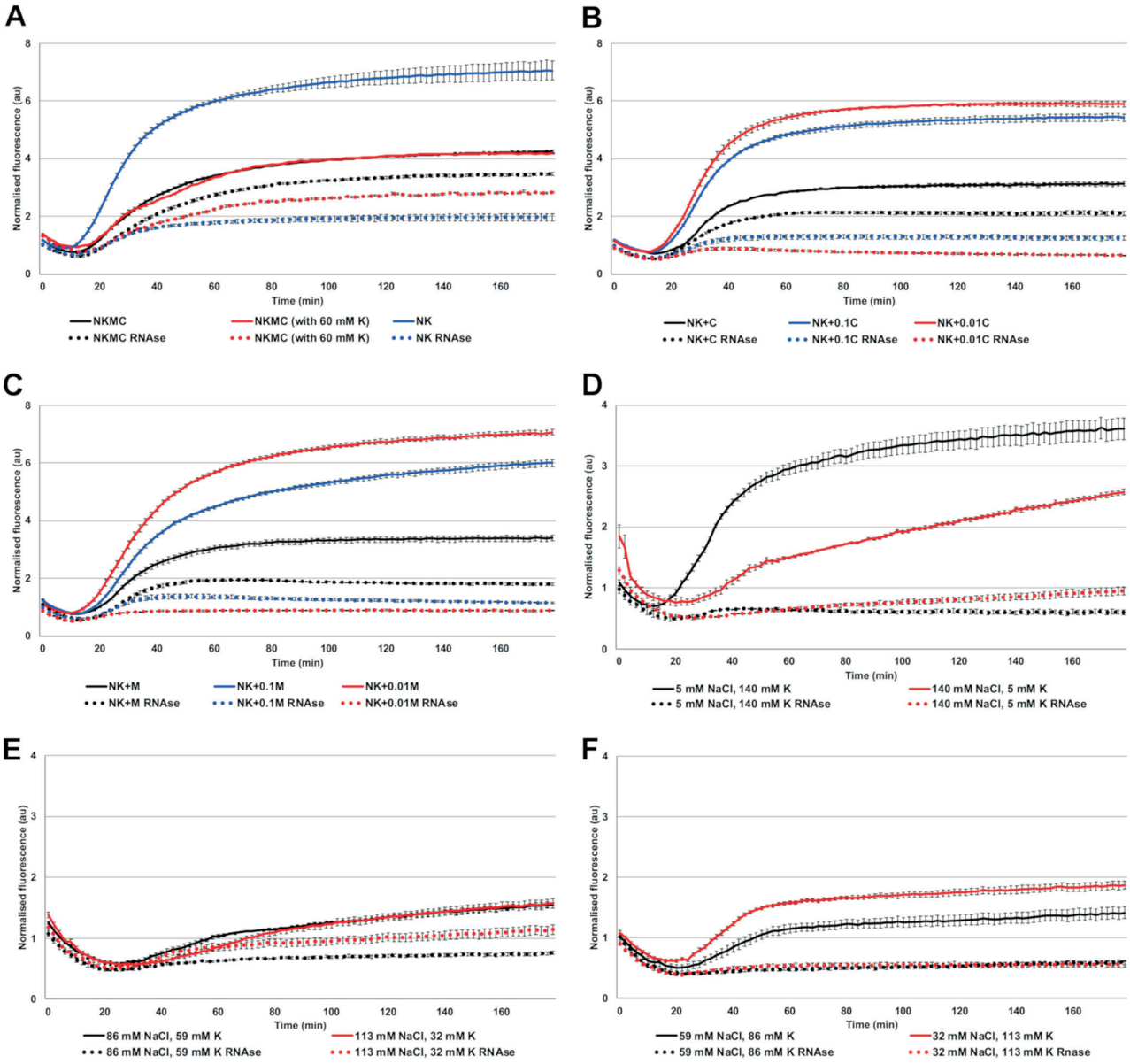

FIG 2 Virus stability in NK solution with different amounts of K^+, Mg^{2+} (M), and Ca^{2+} (C) at 37°C. (A) Fluorescence measurements of SGII dye in the presence of 1 μg E1 in NKMC, containing 30 mM K phosphate (black lines), NKMC with higher, 60 mM, K phosphate (red lines), and NK (i.e., without Mg^{2+} and Ca^{2+}, blue lines) solutions. (B) Fluorescence measurements of SGII dye in the presence of 1 μg E1 in NK solution with different amounts of $CaCl_2$ (C = 200 μM, 0.1C = 20 μM, 0.01C = 2 μM). (C) Fluorescence measurements of SGII dye in the presence of 1 μg E1 in NK solutions with different amounts of $MgCl_2$ (M = 500 μM, 0.1M = 50 μM, 0.01M = 5 μM). (D) Fluorescence measurements of SGII dye at 37°C in the presence of 1 μg E1 in either intra- and extracellular Na^+ and K^+ concentrations, combined with intracellular 800 μM $MgCl_2$ and 0.2 μM $CaCl_2$ concentrations. (E and F) Fluorescence measurements of SGII dye at 37°C in the presence of 1 μg E1 in various Na^+ and K^+ concentrations between intra- and extracellular values, but constant intracellular 800 μM $MgCl_2$ and 0.2 μM $CaCl_2$ concentrations.

Similarly to the NK solution without divalent cations, concentrations of 0.002 and 0.02 mM Ca^{2+}, 100-fold and 10-fold dilutions of Ca^{2+} compared to NKMC, respectively, as well as 0.005 and 0.05 mM Mg^{2+}, 100-fold and 10-fold dilutions of Mg^{2+} compared to NKMC, respectively, mainly caused the formation of empty virions (Fig. 2B and C). In contrast, the presence of 0.2 mM Ca^{2+} or 0.5 mM Mg^{2+} in NK solution prevented RNA release from a significant number of the virions (Fig. 2B and C, black lines).

We also tested different concentrations of sodium and potassium ranging between their extra- and intracellular values (extracellular concentrations roughly 140 mM Na^+

and 5 mM K^+ versus intracellular 5 mM Na^+ and 140 mM K^+). The concentrations of Mg^{2+} and Ca^{2+} were kept at their cytoplasmic values of 0.8 mM and 0.2 μM, respectively, while we changed Na^+ and K^+ concentrations step by step from 5 mM to 140 mM and 140 mM to 5 mM, respectively. The results showed that at 37°C, cytoplasmic ionic concentrations caused a clear increase in the number of empty virus particles: RNA release started already within 15 min (Fig. 2D). This suggests that the intracellular ion concentrations, 140 mM K^+, 5 mM Na^+, 0.5 mM $MgCl_2$, and 0.2 μM Ca^{2+}, are effective in promoting RNA release. Notably, the extracellular concentrations of Na^+ (high) and K^+ (low) resulted in the formation of empty particles in the presence of intracellular Mg^{2+} (0.5 mM) and Ca^{2+} (0.2 μM) concentrations (Fig. 2D). The concentrations of K^+ and Na^+ between the extremes were less effective at promoting RNA release (Fig. 2E and F).

In summary, the ionic conditions found in endosomes, with lowered Na^+ and Ca^{2+} and higher K^+ concentrations compared to that in the extracellular space, trigger a slow uncoating process. Even further reduction in the Ca^{2+} concentration and increase in K^+ concentration, as may happen in the endosomes, facilitates also the RNA release from the virions.

Albumin triggers the E1 uncoating process. Comparison of 1% S-MEM and MEM without serum clearly showed that serum triggered the uncoating process, resulting in increases of both the uncoating intermediate and empty virus (Fig. 3A). We then tested if serum would have any additive effect when administered in the NKMC solution. We observed a clear increase in the rate of the fluorescence signal appearance: with NKMC, the maximal fluorescence signal was reached only at the end of the 3-h measurement, whereas in the presence of 1% serum, this time was shortened to approximately 30 min (Fig. 3B). Interestingly, with 1% serum, the amount of RNA released from the virions decreased and the intermediate particles remained stable throughout the measurement.

In order to narrow down the serum components responsible for the boosting effect, we focused on albumin, as it is the most abundant protein in serum (46). As 1% serum corresponds to approximately 0.04% albumin solution, we decided to use 0.01% to 0.1% BSA concentrations to see if albumin was responsible for the changes that we observed with 1% S-MEM. As it is known that albumin is a high-affinity fatty acid carrier in the blood (46) and the lipid moiety, typically palmitate (47), present in the hydrophobic pocket of many enteroviruses is important for the virion stability (15), we tested also fatty acid-free BSA (faf-BSA) in our experiments.

The spectroscopy measurements showed that both BSA and faf-BSA triggered the uncoating process in MEM in a similar manner to 1% S-MEM (Fig. 3A and C), suggesting that the major factor in serum initiating the uncoating process is indeed the serum albumin. Moreover, both albumin forms promoted serum-like effects in NKMC (Fig. 3D). After observing that BSA and faf-BSA resulted in similar results as serum in both isotonic MEM and hypotonic NKMC, we tested faf-BSA in DPBS and saw that it induced the uncoating process similarly to MEM (Fig. 3E). Spectroscopy analysis of the virus treated with EM buffer prepared for cryoEM imaging showed a large amount of the uncoating intermediate particles (Fig. 3E).

Since albumin appeared to be the major factor inducing and boosting the virus priming, we tested if the addition of fatty acids would prevent the observed effect. We started with conditions that most efficiently caused RNA release: we treated the ^{35}S-labeled E1 with NK solution supplemented with 0.1% faf-BSA (Fig. 3F, red curve peak fractions 4 to 9). The presence of approximately 100-fold molar excess of palmitate (400 μM) with respect to the amount of albumin in the assay fully protected the E1 virions from the structural changes as detected by sucrose gradient analysis (Fig. 3F, blue curve).

We next explored in more detail the molar ratio between BSA and virus required for efficient triggering of the uncoating process. We found that an albumin-to-virion ratio of 1,200:1 (comparable to 0.01% faf-BSA solution with 1 μg of E1 used in spectroscopy

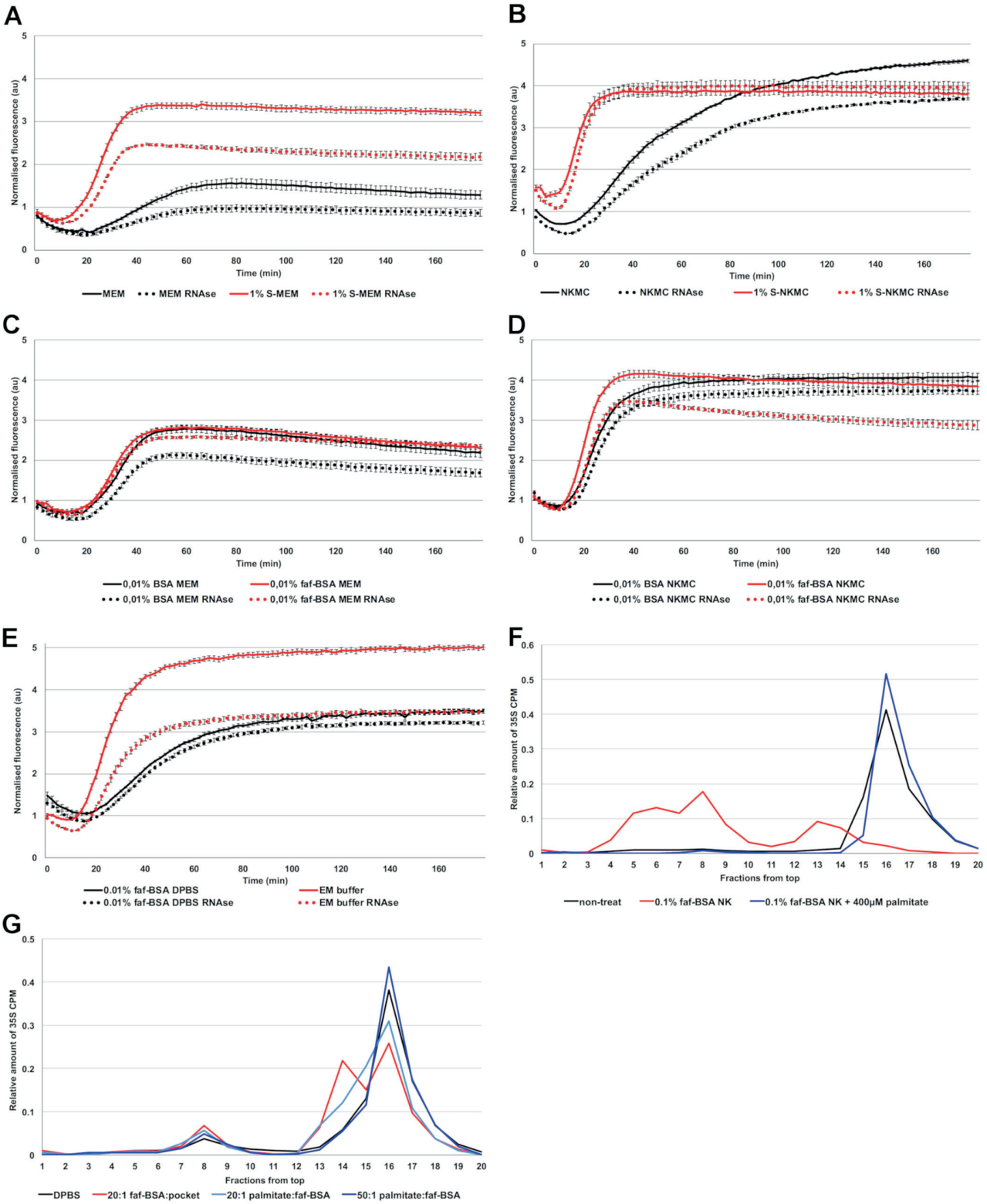

FIG 3 Serum and albumin promote virus opening at 37°C. (A) Fluorescence measurements of SGII dye in the presence of 1 μg E1 in MEM and 1% S-MEM. (B) Fluorescence measurements of SGII dye in the presence of 1 μg E1 in NKMC and 1% S-NKMC. (C) Fluorescence measurements of SGII dye in the presence of 1 μg E1 in MEM supplemented with 0.01% BSA or faf-BSA. (D) Fluorescence measurements of SGII dye in the presence of 1 μg E1 in NKMC solution supplemented with 0.01% BSA or faf-BSA. (E) Fluorescence measurements of SGII dye in the presence of 1 μg E1 in DPBS supplemented with 0.01% faf-BSA

(Continued on next page)

assays), which corresponds to an albumin-to-hydrophobic pocket ratio of 20:1, efficiently triggered the formation of the uncoating intermediate (Fig. 3G). In contrast, an albumin-to-virion ratio of 120:1 showed only a mild effect, and a ratio of 17:1 induced no changes compared to the control condition (data not shown). The virus treatment with albumin did not significantly increase the amount of empty viruses.

Then we tested the concentration of free fatty acids needed to prevent the uncoating process. Adding increasing amounts of palmitate to the faf-BSA virus mixture reduced the formation of uncoating intermediate and concomitantly increased the amount of intact virions (Fig. 3G). Full protection against uncoating was gained by adding a 50-fold molar excess of palmitate with respect to the faf-BSA molecules, whereas a 20-fold excess showed an intermediate effect (Fig. 3G). The effect of a 10-fold excess was still notable, but an equimolar ratio showed no protection (data not shown).

These results show that albumin is the major component of the serum that triggers the uncoating process. It further stresses the fact that the net balance between fatty acids and albumin is important in enterovirus particle uncoating.

Structural details of the treated virion. Having ascertained the physiological factors that could reproducibly start the uncoating process, we studied the treated virions by negative staining as well as by cryoEM and single particle reconstruction. Negatively stained preparations of cryoEM buffer-treated sample revealed three distinct forms of E1: intact, intermediate, and empty particles (Fig. 4A). In the EM buffer-treated virus sample, 29% of particles were intact, 65% were intermediate, and 6% were empty (of 2,108), whereas in nontreated sample, the percentages were 95%, 4%, and 1% (of 2,624), respectively. In cryoEM micrographs, we could not distinguish between intact and the intermediate particles by eye, but after image analysis and classification, 70% of all particles were intermediate (23,983 of 34,160) processed from the treated sample's micrographs (Fig. 4B). Thus, the reconstruction of the treated particle described below represents the averaged structure for the most populated viral particle in the treated sample. Two-dimensional averages of the control and treated particles clearly show the density for both the capsid and RNA (Fig. 4C).

Icosahedral reconstruction of the intact E1 virus from the control sample's cryoEM micrographs to 3.5-Å resolution was similar to the published X-ray structure PDB identifier (ID) 1EV1 (48). The atomic model fitted into the intact E1 reconstruction included the lipid factor in the lipid pocket and density for all four capsid proteins, VP1, VP2, VP3, and VP4 (Table 2, Fig. 4D, F, G, and H, and Fig. 5A to C) (48). The root mean square deviation (RMSD) compared to the X-ray structure was 0.77 Å. The intact E1 reconstruction shows icosahedrally averaged RNA density, which has not been reported earlier (Fig. 4F and H; Fig. 5A). The majority of the RNA follows the outline of the capsid and is distributed at a distance of 0 to 10 Å from the inner capsid surface, with the highest density between radii 94 and 113 Å (from the virion center). The RNA has clear connections around the 2-fold axes of symmetry to Trp 38 of VP2 (Fig. 5A). In addition, Arg 13 and Arg 27 of VP1 as well as a poorly resolved VP4 loop contact the RNA density. Similar RNA-capsid interactions involving VP2 Trp 38 and VP1 N terminus have been described in intact rhinovirus particles (30).

In comparison, the 3.6-Å resolution treated particle reconstruction has undergone a 4% expansion (Fig. 4E, I, J, and K). It was possible to model most of the VP1, VP2, and VP3 but none of VP4 in the reconstruction (Table 2 and Fig. 5D to F). The atomic modeling revealed that the capsid expansion occurred through rotation and outwards translation of the capsid proteins VP1, VP2, and VP3. This results in a fenestrated capsid, with prominent holes on the edges of the capsid close to the 2-fold axes of symmetry

FIG 3 Legend (Continued)
and in EM buffer. (F) Effect of faf-BSA and fatty acids on virus uncoating and priming using 5% to 20% sucrose gradient analysis of metabolically labeled ^{35}S E1. Nontreated virus in comparison to fully opened virus (red line; 1 h of incubation with 0.1% faf-BSA NK at 37°C) and fatty acid-rescued virus after addition of 400 μM palmitate (blue). (G) Virus treated for 1 h at 37°C in DPBS in comparison to DPBS supplemented with 1.5 μM faf-BSA (20:1 ratio of faf-BSA to virus hydrophobic pockets, red line), or, in addition to 1.5 μM faf-BSA, with increasing (20:1 and 50:1) molar ratio of palmitate to the faf-BSA (light blue and dark blue lines, respectively).

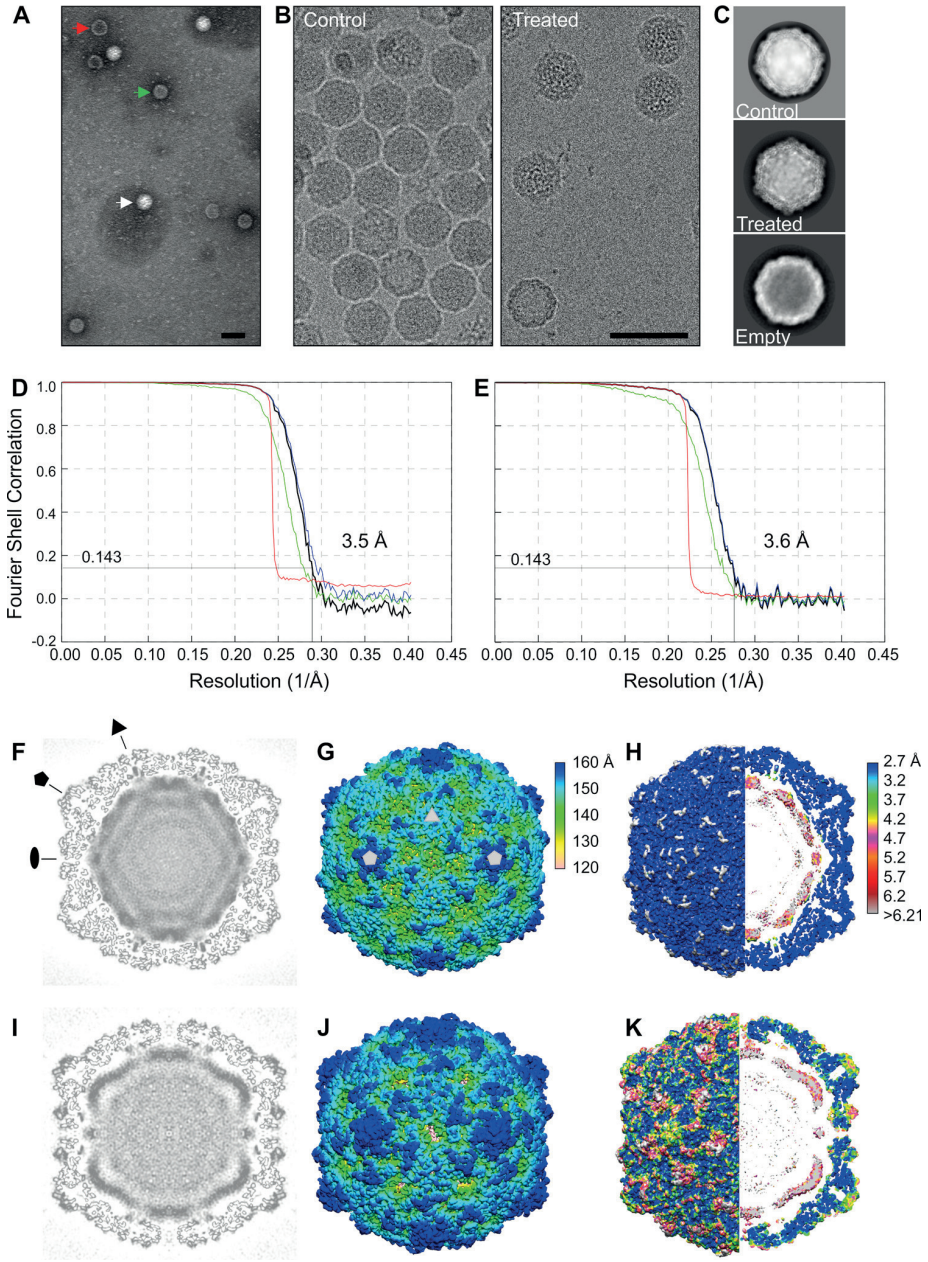

FIG 4 Electron microscopy and cryoEM reconstructions of E1 intact and treated virions. (A) Negative stain of E1 after 1 h treatment at 37°C with 29 mM NaCl, 28 mM K, 0.145 mM $MgCl_2$, 0.0093% faf-BSA. (B) Cryo-electron micrographs of nontreated (control) E1 and E1 after similar treatment to that for panel A. The white arrow indicates an intact virion, the red arrow an empty particle, and the green arrow an intermediate particle. Bars, 50 nm. (C) Example of 2D class averages showing intact (control, $n = 16{,}298$), treated ($n = 2{,}015$), and empty ($n = 212$) class averages, where n is the number of particles contributing to the averages shown. Box size is 496 Å (D) Fourier shell correlation curves for the control E1 reconstruction, giving a resolution of 3.5 Å with a cutoff of 0.143. (E) Fourier shell correlation curves for the treated particle reconstruction giving a resolution of 3.6 Å with a cutoff of 0.143. Corrected (black), unmasked (green), masked (blue), and phase randomized masked (red) maps (71). (F) Control E1 reconstruction central plane. Pentagon, triangle, and oval indicate 5-fold, 3-fold, and 2-fold symmetry axes, respectively. (G) Radially colored isosurface representation of the control E1 reconstruction viewed down a 2-fold axis of symmetry at 1.5 standard deviations (SDs) above the mean. Pentagons and triangle mark 5-fold and 3-fold axes, respectively. Two-fold axis is in the middle between the two marked 5-fold axes. (H) Control E1 colored by local resolution (79). (I) Treated particle reconstruction central plane. (J) Isosurface representation of treated particle viewed down a 2-fold axis of symmetry at 1.5 SDs above the mean. Radially colored according to the color key in panel G. (K) Treated particle colored by local resolution. Resolution colored according to the color key in panel H.

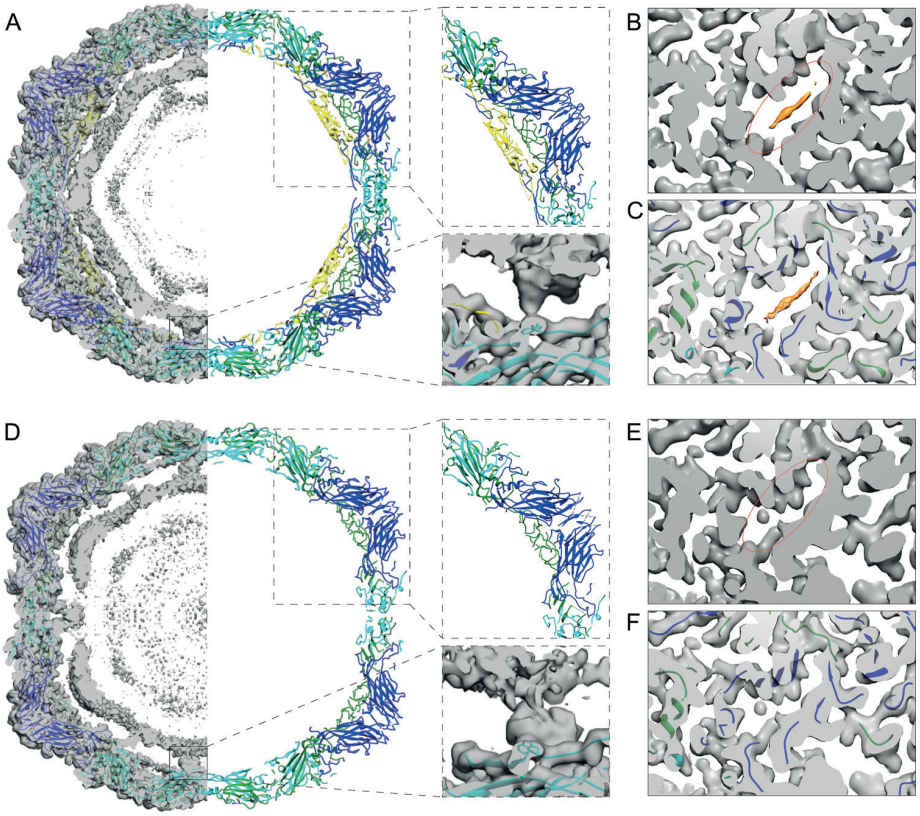

FIG 5 Comparison of reconstructions and atomic models of control and treated E1 virions. (A) Slab of the virion atomic model (1EV1) (48) shown in ribbon, fitted into the control E1 density (left). Most of the capsid density is accounted for by the atomic model, but the inner density from the RNA is not. The upper right inset highlights the structure of one pentamer with VP4. The lower right inset highlights the interaction of the RNA and VP2 Trp 38 next to the 2-fold axis. (B) Section of control E1 reconstruction revealing the pocket and the lipid factor. (C) The same as in panel B with the atomic model fitted. (D) Slab of the treated atomic model (wwPDB deposition ID 6O06) shown in ribbon, fitted into the treated particle density (left). Most of the capsid density is accounted for by the atomic model, but the inner density from the RNA is not. The position of the RNA has moved radially outwards as the capsid expanded, maintaining the 2-fold connections. The upper right inset highlights the structure of one pentamer without VP4 modeled as there was no apparent density for it. The lower right inset highlights the interaction of the RNA and VP2 Trp 38 next to the 2-fold axis. (E) Section of treated particle reconstruction revealing the collapsed pocket and no evident density for the lipid factor. (F) The same as in panel E with the atomic model fitted. For all panels, EM density shown in transparent gray, lipid factor EM density in orange, VP1 (blue ribbon), VP2 (cyan ribbon), VP3 (green ribbon), VP4 (yellow ribbon), lipid factor (orange stick). In panels B and E, orange ovals indicate the corresponding positions of the pocket.

at the VP2 dimer interface, a hallmark of A-particles described for other enteroviruses (Fig. 4J and Fig. 6A and B). The atomic model emphasizes these holes, somewhat artificially, as not all the electron density has been accounted for (Fig. 6B and D). The pocket factor has been released (Fig. 5E and F). The GH loop on VP1, thought to be important in pocket factor release, has moved, collapsing the pocket. The RNA is clearly visible, its average conformation has changed, but it still maintains connections to the capsid via VP2 Trp 38, Glu 40, and Tyr 41 (Fig. 5D). The contacts mediated by the VP1 N termini and VP4 have been lost in the treated particle, but new connections appeared via the N termini of VP3 below the 5-fold vertices. In the control particle, these VP3 termini interact with VP4. Similar RNA-capsid interactions mediated by VP2 Trp 38 and VP3 N termini were seen in expanded rhinovirus particles (30). The averaged RNA still follows the profile of the inner surface of the capsid, but has moved outwards (Fig. 4 to 6), with the highest density between radii 102 and 122 Å. Thus, the RNA is less densely packed in the treated intermediate particle.

Besides the poorly ordered density inside the capsid assigned to viral RNA, the difference map between the control reconstruction and the atomic model of intact E1

TABLE 2 Summary of cryoEM data collection, refinement, and validation statistics

Category	Value	
	Treated E1	Control E1
Data collection		
Voltage (kV)	200	200
Electron exposure (e^{-}/Å^2 × s)	30	30
Pixel size (Å)	1.24	1.24
No. of micrographs	1,246	979
Reconstruction		
No. of particles	14,615	45,309
B factor (Å^2)	−70	−70
FSC[a] threshold	0.143	0.143
Resolution (Å)	3.6	3.5
Model building (aa)[b]		
VP1 (full protein, 281 aa)	55–130 and 137–280	1–281
VP2 (full protein, 261 aa)	12–54 and 58–261	7–261
VP3 (full protein, 239 aa)	3–174 and 184–237	1–239
VP4 (full protein, 68 aa)	none	1–14 and 22–68
Model validation		
MolProbity score (percentile)	1.25/100th[c]	1.08/100th[d]
Ramachandran outliers (%)	4.3	2.06
Poor rotamers (%)	1.7	1.24
Clash score	0	0

[a]FSC, Fourier shell correlation.
[b]aa, amino acid.
[c]N = 342, 3.25 Å to 3.85 Å.
[d]N = 27,675, 0 Å to 99 Å.

showed only a small unassigned density in the capsid protein region at the 3-fold axes of symmetry (Fig. 6C). This unassigned density could be attributed to six unmodeled residues of the VP2 N terminus (Fig. 6C, red arrows in the inset). The difference map between the treated particle reconstruction and atomic model revealed a less-well-ordered lower resolution density near the 2-fold axes spanning the capsid from the interior to the exterior and at the 5-fold axes on the particle surface (Fig. 6D). The first modeled residue of the VP1 N terminus (Asn 55) lies in close proximity to the unassigned density near the 2-fold axis inside the particle; therefore, the unassigned density could be the VP1 N termini now traversing the capsid and exposed on the surface of the treated capsid similarly to the interpretation for expanded particles of other enteroviruses (Fig. 6D, red arrows in the inset) (20, 26, 49). In addition, part of this poorly ordered density seen on the exterior could be attributed to a flexible VP3 loop (residues Thr 175 to Asp 183). The poorly defined density seen at the 5-fold axes on the capsid surface is most likely attributed to disordered loops in VP1 (residues Thr 131 to Asn 136). Although VP4 could not be modeled in the density, its partial presence in the treated sample was confirmed by autoradiography (Fig. 7). Moreover, the treated virus sample showed approximately 2 logs lower infectivity (decrease from 8.23×10^{11} to 1.01×10^{10}), confirming our previously published data for the E1 uncoating intermediate particle (14). Hence, VP4 could contribute to the poorly ordered density on the inside of the capsid close to the vertices, attributed primarily to RNA, as well as to the density spanning the capsid. In corroboration of this finding, the presence of a tiny amount of VP4 was recently reported in A-particles of enterovirus D68 induced by acid treatment (49).

DISCUSSION

We showed previously that during entry into cells, E1 undergoes structural changes that were first discovered as an increased permeability to the small molecule dye, SYBR green II, and Cs-ions (14). Here, we showed by cryoEM that temperature-dependent structural changes, under physiological conditions, involved expansion of the virus

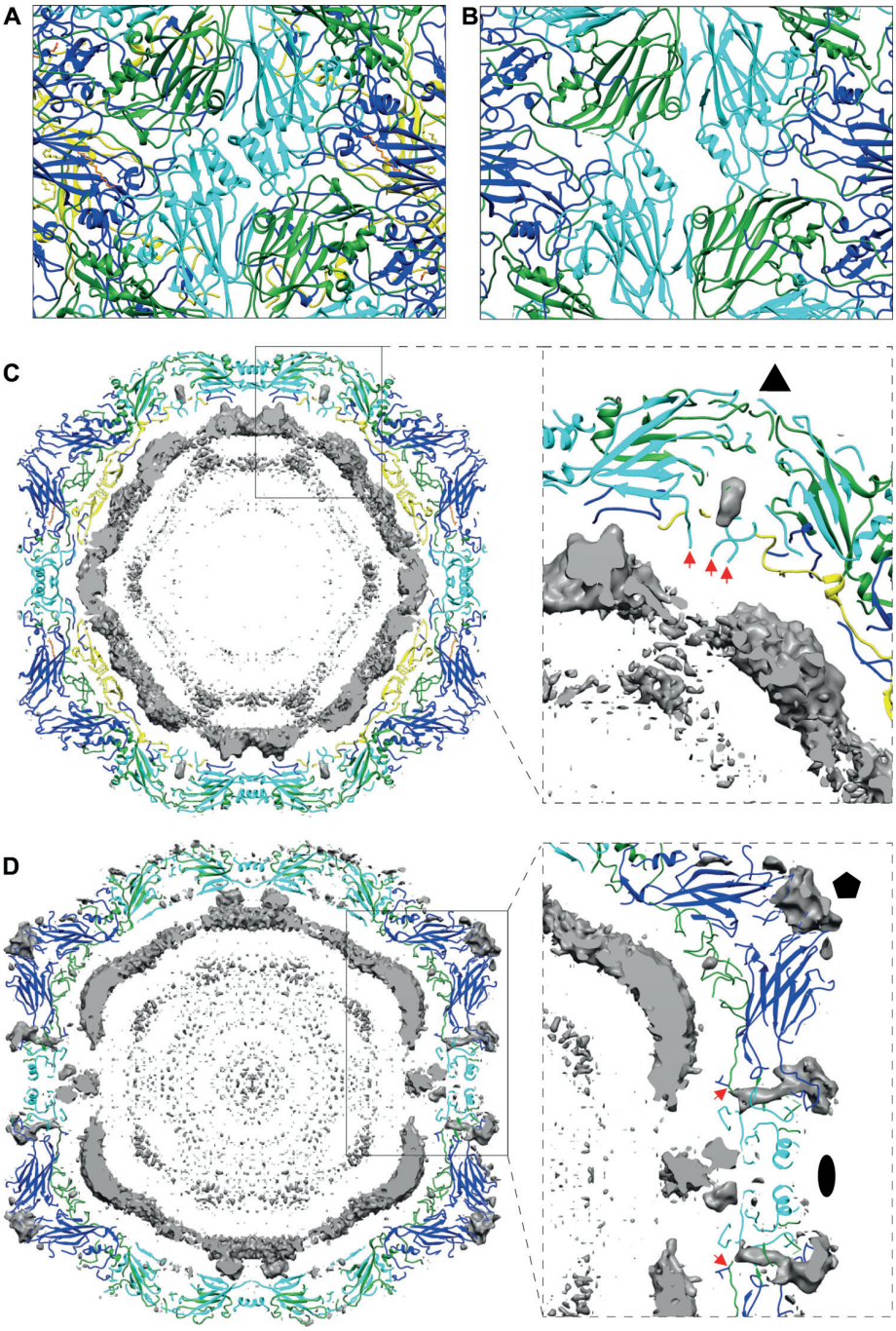

FIG 6 Treated particle expansion and unmodeled cryoEM density. (A) Atomic model of control E1 seen along 2-fold axis. (B) Atomic model of the treated intermediate virion seen along 2-fold axis showing opening between two VP2 helices. (C) Unmodeled cryoEM density of control E1 (gray isosurface). Inset shows unmodeled density at the 3-fold axis. Red arrows indicate N termini of VP2 (Cys 7) in the vicinity of unmodeled density blob. Triangle indicates 3-fold symmetry axis. (D) Unmodeled cryoEM density of the treated virion (gray isosurface). Inset shows unmodeled density spanning the capsid near 2-fold axis. Red arrows indicate N termini of VP1 (Asn 55) in the vicinity of the unmodeled density spanning the capsid. Pentagon and oval indicate 5-fold and 2-fold symmetry axes, respectively. For panels A to D: VP1 (blue), VP2 (cyan), VP3 (green), VP4 (yellow), lipid factor (orange).

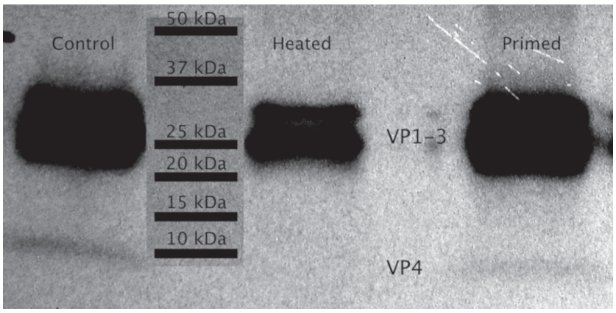

FIG 7 Autoradiography observation of ^{35}S-labeled VP4 protein. Metabolically labeled E1, nontreated, heated to 50°C for 10 min, and EM buffer-treated sample.

particle, loosening of the genome packing, loss of the lipid factor, and formation of larger openings at the VP2 dimer interface, explaining the increased permeability to the small molecular dye and the resistance to RNase treatment observed previously (14). We also showed by spectroscopy that serum priming of coxsackievirus B3 and coxsackievirus A9 caused similar changes in permeability to that of E1, suggesting that also other enteroviruses behave similarly (Fig. 1F).

Our *in vitro* experiments demonstrated two important factors in the serum and extracellular space affecting the integrity and the dynamics of E1 virion at 37°C, albumin and fatty acids, one of the most abundant components in the serum and interstitial fluids. Albumin concentration in serum has been reported as 640 μM (46) and the albumin-bound fatty acids concentration ranging from 200 to 700 μM in serum (50). As mentioned before, albumin serves as the major fatty acid carrier in the blood, with two to three high-affinity and four to five intermediate-affinity binding sites for fatty acids (46). Also, the fatty acid binding capacities of BSA and faf-BSA have been measured to be around 4.8 mol and 7 mol per mol albumin, respectively (51). The measurements further showed that BSA is approximately 50% occupied by serum fatty acids, meaning that roughly 50% of the fatty acid binding capacity is still left (51). Furthermore, both Penn et al. (51) and van der Vusse (46) showed that bovine and human albumin have very similar fatty acid binding capacities, making bovine albumin a good surrogate for human albumin. These data provide further support that under physiological conditions, BSA is not saturated with fatty acids. Thus, the most likely explanation for the increased intermediate particle formation at low fatty acid concentration is the partitioning of the fatty acid moiety from the capsid into a more hydrophobic environment, such as into the fatty acid binding sites on the albumin. Higher temperature will result in higher mobility of the fatty acid. Furthermore, the fatty acid saturation level of albumin has a great effect on capsid stability. This was demonstrated by the prevention of virus expansion and RNA release using increasing concentrations of palmitate in comparison to albumin (Fig. 3E and F). Considering the observed molar excess of fatty acids required to prevent the formation of an albumin-induced intermediate particle (Fig. 3F), and the approximately 1:1 ratio of albumin and fatty acids observed in serum, it seems probable that under physiological conditions, the albumin present outside the cells starts the uncoating process. The ability of faf-BSA to induce echovirus A-particle formation was previously shown using a radioactive gradient; however, the nature of this process was not studied further (21). Our results here explain the mechanism by which faf-BSA induces uncoating in enteroviruses, such as echoviruses and coxsackieviruses. Moreover, we suggest that the loss of the pocket factor likely precedes receptor binding, promoting the formation of an infectious intermediate particle already in the extracellular space.

The expansion of E1 capsid does not affect the receptor, α_2I-domain, binding site (14, 52). However, the expansion does cause changes in the amino acid composition exposed on the capsid surface, such as the exposure of the VP1 N terminus, which may

also give rise to new secondary receptor binding sites. If some lipid factors would still be bound to the capsid in the endosome initially, they could well be exchanged into the hydrophobic environment of the endosomal membrane that would extract the lipid factor from the capsid. In support of this hypothesis, albumin readily donates fatty acids to other fatty acid binding proteins in the vicinity of the plasma membrane. Furthermore, the binding and release of the lipid factor in enteroviruses is known to be a dynamic process (53, 54). A potential endosomal membrane protein that could help to sequester the lipid factor is the lipid-modifying enzyme PLA2G16 (55). It is thought to affect the insertion of VP4 into the endosomal membrane but could potentially help to sequester the lipid factor too (56).

The next and final step in picornavirus uncoating is the RNA release. Accumulated results on CVA9 and E1 uncoating show that it starts as early as 15 to 30 min postinfection, and the extent of uncoating increases strongly until 1 to 2 h postinfection (57, 58). However, the first signs of replication, including negative- and positive-strand RNA production, occur as late as 2 h postinfection (59). This suggests that the ambient endosomal ion conditions develop gradually to better promote the uncoating and the final RNA release into the cytoplasm. Current information on the intraendosomal ionic changes over time suggests that the sodium and calcium concentrations in endosomes decrease during their maturation and potassium concentration rises relative to the extracellular values (39). Our results demonstrated that a combination of low sodium and calcium and elevated potassium in the presence of a physiological magnesium concentration was able to trigger the uncoating process; however, it was more rapid in the presence of albumin (Fig. 3B and D). Furthermore, in addition to the formation of the uncoating intermediate, the right combination of ions led to more efficient RNA release (Fig. 2A) that could be further increased with faf-BSA (Fig. 3E, fluorescence data not shown). In the lack of thorough absolute ion concentration measurements inside the endosomes, the present study may underestimate the complexity and actual combination of the ions present. No ions have been resolved in the X-ray structure of E1, and so we cannot directly interpret the effects of the ions on the capsid or the RNA stability. However, both K^+ and Mg^{2+} ions can stabilize RNA tertiary structures (60). Thus, we hypothesize that changes in these ions may contribute to the expansion of the RNA, providing an additional force to promote conformational change in the capsid and eventual release of the RNA in the endosome. Changes in the Ca^{2+} and Na^+ ion concentrations probably affect the protein stability, through electrostatic interactions. Ca^{2+} has been shown to be important for the capsid stability of many viruses (24, 40–44).

The RNA-capsid interactions were resolved in structures of A-particles published for several enteroviruses, such as enterovirus 71, coxsackievirus A16, and rhinovirus 2, suggesting their importance in assisting RNA release (20, 30, 31). The genome is unique within the capsid; nevertheless, in some picornaviruses, the RNA is so well ordered that individual bases can be identified, ranging from one base to several (61–66). Here, the icosahedral reconstructions also showed for the first time details of the RNA, though not resolved to the atomic level, inside the intact E1 particle and in the uncoating intermediate structure. The RNA has a high density in proximity to the intact capsid, which suggests high occupancy, and the probable interaction of the RNA with both the ordered capsid proteins (notably with VP1, VP4, and VP2 shown in Fig. 5A) and their disordered termini (67). Trp 38 in VP2, a highly conserved residue in picornaviruses, points toward ordered RNA (61–66). This interaction between the RNA and capsid is directly adjacent to the major fenestrations that appear in the treated capsid, where the RNA has moved radially outwards, maintaining this specific interaction (Fig. 5D). Interestingly, this RNA-capsid interaction is in proximity to the N terminus of VP1 that appears to be extruded from the treated capsid, similarly to the VP1 in expanded poliovirus, coxsackievirus A16, and enterovirus D68 (20, 26, 49). VP4 could not be identified in the reconstruction, suggesting that it is no longer icosahedrally ordered or the occupancy is much reduced as suggested also by autoradiography. This implies that the RNA interaction with the capsid via VP4 under the vertices was significantly

altered compared to the intact particle (Fig. 5). VP4 may have collapsed into the density attributed to RNA that is still prominent below the VP3 annulus at the vertices (Fig. 4 and 5). Changes in the RNA packaging density and its interaction with the capsid proteins, along with the expansion of the particle, are probably also responsible for the increase in permeability to dye.

Altogether, our results suggest that based on the dynamic nature of albumin-mediated fatty acid binding and the fact that both albumin and fatty acids are present outside cells, the majority of the enterovirus particles may reside in a triggered, intermediate, metastable state before entering cells. According to our results, the albumin-triggered intermediate state is likely to lead to more-efficient RNA release when it is further affected by the ambient concentrations of monovalent and divalent cations in endosomes.

MATERIALS AND METHODS

E1 production and purification. E1 was produced and purified as described earlier (14). Confluent 5-layer bottles of green monkey kidney (GMK) cells, obtained from the American Type Culture Collection (ATCC), were infected with E1 (Farouk strain; ATCC) for 16 to 20 h at 37°C with 5% CO_2. After infection, the cells and media were collected and lysed with three freeze-thaw cycles. The lysate was pelleted by centrifugation with a JA-10 rotor (6,080 rpm, 30 min, 4°C), after which, the supernatant was precipitated for 16 to 20 h at 4°C using polyethylene glycol 6000 (Sigma-Aldrich, St. Louis, MO, USA) (8% [wt/vol]), and NaCl (2.2%[wt/vol]). The precipitated supernatant was then centrifuged with a JA-10 rotor (8,000 rpm, 45 min, 4°C), and the resulting pellet was dissolved in R buffer (10 mM Tris-HCl [pH 7.5], 200 mM $MgCl_2$, 10% [wt/vol] glycerol). For disrupting the remaining cellular membranes, 0.3% (wt/vol) sodium deoxycholate (Sigma-Aldrich) and 0.6% (vol/vol) Nonidet P-40 (Sigma-Aldrich) were mixed with the supernatant and incubated for 30 min on ice. The remaining debris was pelleted by centrifuging in a TX-200 rotor (4,700 rpm, 15 min, 4°C), and the resulting supernatant was loaded on top of 10-ml linear 10% to 40% (wt/vol) sucrose gradients in R buffer. The gradients were ultracentrifuged in an SW-41 rotor (30,000 rpm, 3 h, 4°C) and fractioned into 500-μl aliquots. The optical density at 260 nm of each fraction was measured with a NanoDrop 1000 spectrophotometer (Thermo Scientific, Waltham, MA, USA) to identify fractions containing virus. These fractions were dialyzed against 2 mM $MgCl_2$-phosphate-buffered saline (PBS-$MgCl_2$) in a Spectra/Por Micro Float-A-Lyzer with Biotech cellulose ester membranes and 300-kDa cutoff (Spectrum Laboratories Inc., USA) at 4°C. Finally, the viruses were pelleted by ultracentrifugation using a 70-Ti rotor (35,000 rpm, 2 h, 4°C) and resuspended in PBS-$MgCl_2$. Several purified virus batches were used, ranging between 0.5 and 1.3 mg/ml and 1×10^{11} and 1×10^{12} PFU/ml.

^{35}S E1 production and purification. ^{35}S-labeled E1 for gradient analysis was produced in GMK cells as described earlier (14). Semiconfluent cell culture bottles were washed at 37°C for 15 min with PBS and infected with E1 (Farouk strain; ATCC) using low-methionine-cysteine medium supplemented with 1% fetal bovine serum (FBS) for 3 h. After this, the medium was changed into the above-mentioned medium supplemented with 50 μCi/ml of [^{35}S]methionine-cysteine, and the infection was allowed to proceed for 16 to 24 h until nearly all of the cells were detached. The cells were lysed via 3 freeze-thaw cycles, and the cell debris was pelleted using a TX-200 rotor (4,000 rpm for 15 min, 4°C). The supernatant was further treated with 0.3% (wt/vol) sodium deoxycholate and 0.6% (vol/vol) Nonidet P-40 for 30 min on ice, and the supernatant was further cleared by centrifugation (TX-200, 4,700 rpm, 15 min, 4°C). The supernatant was loaded onto the top of a 2-ml 40% sucrose cushion at 4°C. The cushions were ultracentrifuged at 30,000 rpm (SW-41) for 2.5 h at 4°C, after which the liquid above the cushion and one 500-μl fraction from the cushion were discarded and the three next 500-μl fractions were collected. These fractions were diluted in PBS-$MgCl_2$; the virus was pelleted by centrifuging at 35,000 rpm (70-Ti) for 2 to 3 h at 4°C, after which the pellet was resuspended in 1.5 ml of PBS-$MgCl_2$ and the different virus populations were further separated in a 5% to 20% sucrose gradient in R buffer via gradient centrifugation (35,000 rpm, SW-41, 2 h, 4°C). The virus-containing fractions were identified via liquid scintillation counting (Perkin Elmer, Waltham, MA, USA). The three fractions containing the largest amount of intact virus particles were again collected and pelleted as above. The resulting pellet was dissolved in 400 μl of PBS-$MgCl_2$, divided into smaller aliquots, and stored at −80°C after determination of cpm/μl of the ^{35}S E1 stock.

CVB3 and CVA9 production and purification. CVB3 (ATCC Nancy strain) and CVA9 (ATCC Griggs strain) were purified similarly to E1, except they were separated in 5% to 20% sucrose gradients. From the gradient, fractions 1 to 10 were discarded and 11 to 20 collected. The collected fractions were diluted with PBS-$MgCl_2$ to a final volume of 25 ml and concentrated as described for E1.

Endpoint dilution assay. The endpoint dilution infection assay was performed as described earlier (68). Briefly, GMK cells were cultured in 10% serum-containing MEM and infected with E1 in a dilution series in the presence of 1% serum. Typically, after 3 days of infection at 37°C, the 96-well plate was stained with 50 μl of crystal violet stain (8.3 mM crystal violet, 45 mM $CaCl_2$, 10% ethanol, 18.5% formalin, and 35 mM Tris base) for 10 min. The 50% tissue culture infective dose ($TCID_{50}$) was determined by calculating the numbers of infected and uninfected wells for the eight replicates in one 96-well plate at each dilution. PFU/ml was calculated by multiplying the $TCID_{50}$/ml value by 0.7 according to the Poisson distribution estimation.

Real-time fluorescence uncoating measurements. The measurements were performed using a PerkinElmer 2030 Multilabel Reader Victor X4 with F485 lamp filter and F535 emission filter and 1 s

counting time. In each measurement, 1 μg of nonlabeled virus (corresponding to 0.77 to 2 μl of PBS-$MgCl_2$, depending on the stock concentration) was treated in 100 μl of the buffer described for each experiment in a single well of a 96-well plate (Sarstedt, Nümbrecht, Germany) in the presence of 10× SYBR green II fluorescent dye. The composition of the buffers is presented in Table 1. All of the buffers were neutral in pH ranging between 7.18 and 7.44. Where indicated, RNase A was added to the wells at a final concentration of 10 μg ml^{-1}. By adding RNase to the assay, we distinguished between the fluorescence originating from the porous intermediate particles, i.e., from RNA inside the virus capsid (protected from the RNase activity), and the fluorescence of RNA released from the particles (sensitive to RNase treatment) indicating the presence of empty particles. Intact virion is inaccessible to the dye and thus gives a low fluorescence signal (14). For each virus treatment, a corresponding blank well with all other factors except virus was also measured, and the fluorescence was subtracted to eliminate fluorescence originating from other factors than the virus. Each well was measured either every minute or every other minute for a 3-h time period at 37°C if not otherwise stated. The plate was prepared on ice, from where it was placed into a preheated measurement chamber. The results were processed and plotted using Microsoft Excel. The error bars in the figures represent the standard errors of the means from a minimum of five technical replicates from at least two separate biological replicates. In all graphs, the amount of fluorescence is normalized to the end fluorescence value of the control, 3-h DPBS treatment.

Gradient analysis. One microliter (approximately 10,000 to 80,000 cpm) of ^{35}S E1 together with 1 μg of nonradioactive E1 was treated for 1 h at 37°C in 100 μl of the relevant buffer. The samples were then cooled on ice and loaded onto a cooled 10-ml linear 5% to 20% sucrose gradient. The gradients were centrifuged using an SW-41 rotor (35,000 rpm, 2 h, 4°C), and 500-μl fractions were collected and mixed with scintillation cocktail (Ultima Gold MW; Perkin Elmer). The samples were analyzed using Tri-Carb 2910 TR (Perkin Elmer) and plotted in Excel. Every treatment was repeated at least once, and similar effects were observed.

In the albumin-virus-fatty acid ratio experiment, the molarity of E1 was calculated using molecular weight estimation of 8 MDa for E1, which resulted in 1.25 nM E1 solution with 1 μg of virus in 100 μl of buffer. According to this, 1,200 times higher faf-BSA (Sigma-Aldrich, in double-distilled water [ddH_2O]) concentration (1.5 μM, 1,200 albumins per virus) was used for a 20:1 ratio of albumin molecules to virus pocket factors, and 120 times higher concentration was used for a 2:1 ratio; 17 times higher concentration was used for 2:1 ratio between the albumin's high- to medium-affinity fatty acid binding sites (7 per albumin) versus virus pocket factors (60 per virus). Palmitate (Sigma-Aldrich) from a 15.2 mM stock in 50% methanol (MeOH) was added at either a 20:1 or 50:1 ratio into the 1.5 μM faf-BSA solution.

EM sample preparation, imaging, particle processing, and model building. Virus sample for cryoEM and negative staining was prepared as follows. Purified E1 in PBS-$MgCl_2$ buffer at a concentration of 1.27 μg/μl was mixed with 20 mM NaCl, 30 mM K^+, and 0.01% faf-BSA buffer giving a final concentration of 0.1 μg/μl virus, 29 mM NaCl, 28 mM K^+, 0.145 mM $MgCl_2$, and 0.0093% faf-BSA (EM buffer) and incubated for 1 h at 37°C. The uncoating intermediate formation was confirmed by spectroscopy measurement (Fig. 3E). Control samples were prepared from purified E1 in PBS-$MgCl_2$.

Butvar-coated copper grids were glow discharged (EMS/SC7620 Mini sputter coater), after which the virus sample was added and incubated for 15 s. The excess virus was blotted away, and the grids were negatively stained using phosphotungstic acid (H_2O, pH 7.4) for 60 s; the excess stain was blotted away. The samples were stored overnight at room temperature (RT) before imaging with a JEM-1400 (JEOL) transmission electron microscope (80 kV, Olympus SIS Quemesa bottom-mounted 11 Megapixel charge-couple-device [CCD] camera, ×12,000 to ×40,000 magnification).

Sample volumes of 3 μl of control or EM buffer-treated E1 particle were applied to glow-discharged Quantifoil holey carbon R2/2 grids and vitrified using a custom-made manual plunger. The vitrified samples were imaged on a 200-kV Talos Arctica microscope equipped with a Falcon III direct electron detector at a nominal ×120,000 magnification corresponding to a calibrated pixel size of 1.24 Å. Each exposure was 47.8 s long and collected as a movie containing 30 frames with an accumulated dose of 30 e/$Å^2$ using Thermo Fisher Scientific's automatic data acquisition software.

Dose-fractionated image stacks were aligned using MotionCor2 (69). The contrast transfer function parameters for each micrograph were estimated using Gctf (70). Images containing drift or astigmatism were discarded. Particle selection, two-dimensional (2D) classification, initial model generation, and three-dimensional (3D) classification were performed using RELION 2.1 (71). Final 3D refinement followed by sharpening (B-factor, −70 $Å^2$) of 45,309 intact particles from control sample (~45% of total particles) resulted in a 3.5-Å resolution map. After applying the same procedure to 14,615 uncoating intermediate particles from treated sample (~59% of total particles), a 3.6-Å resolution map was generated.

Model building. A crystal structure of the E1 virion (PDB ID 1EV1) served as an initial starting model for the intact E1 particle (48). An initial atomic model for the uncoating intermediate particle was generated using the I-TASSER server (72) based on the crystal structure of the CVA16 uncoating intermediate (PDB ID 4JGY) (20, 73). The atomic coordinates of the initial models were docked manually into the electron density maps using UCSF Chimera and further optimized using the "Fit in Map" command (74). In the case of the intact particle, one residue (Cys 7) was added to the VP2 N terminus of 1EV1 model using Coot 0.8.8, and the fit was further optimized using molecular dynamics flexible fitting (MDFF) software used along with NAMD and VMD (69–72, 75). A scale factor of 1 was used to weigh the contribution of the cryoEM map to the overall potential function used in MDFF. Simulations included 10,000 steps of minimization and 100,000 steps of molecular dynamics under implicit solvent conditions with secondary structure restraints in place. The atomic model of the uncoating intermediate particle was refined in Coot 0.8.8, and this served as an input for MDFF, NAMD, and VMD software

(75–78). Simulations with scale factor of 1 included 20,000 steps of minimization and 100,000 steps of molecular dynamics under implicit solvent conditions with secondary structure restraints in place. To minimize atom clashes in the atomic model processed in MDFF, seven asymmetric units were simultaneously refined in MDFF using the same secondary structure restraints as above. To analyze unassigned density in intact or treated virion reconstruction, the atomic model was converted to 3.5-(intact) or 3.6-Å (treated) resolution electron density map using the "molmap" command in UCSF Chimera. The map generated for the accounted density was then subtracted from the reconstruction using the "vop subtract" command in UCSF Chimera. The treated particle expansion was estimated by measuring the particle diameter between the 5-fold vertices in intact and treated virions.

Gel separation of viral proteins and autoradiography. One microgram of nonradioactive E1 with 1 μl of ^{35}S E1 (approximately 10,000 to 80,000 cpm) was treated for 1 h at 37°C in EM buffer. Nontreated virus was used as a VP4 detachment negative control, and virus incubated for 10 min at 50°C was used as a positive control. Samples were dialyzed against 1 liter of PBS-$MgCl_2$ for 40 min using a Slide-A-Lyzer mini dialysis device with 10-kDa cutoff (Thermo Fisher Scientific) to remove the possibly detached VP4 from the samples. The samples were boiled for 10 min with the sample buffer and ran in a 4% to 20% gradient gel (MINI-PROTEAN TGX precast gel; Bio-Rad Laboratories, Inc., Hercules, CA, USA). Precision plus protein standard 10 to 250 kDa (Bio-Rad Laboratories, Inc., Hercules, CA, USA) was used to distinguish the molecular weights. The gel was fixed in 30% methanol with 10% acetic acid and treated with autoradiography enhancer (Enlightning; Perkin Elmer). The gel was dried at 70°C for 2 h (Gel dryer 583; Bio-Rad Laboratories, Inc., Hercules, CA, USA) and subjected to autoradiography. Protein bands were analyzed using ImageJ gel analyzer tool.

Data availability. The final density maps have been deposited in the Electron Microscopy Databank (EMDB; https://www.ebi.ac.uk/pdbe/emdb/) with accession codes EMD-4903 (control E1) and EMD-0565 (expanded E1). The atomic models have been deposited in the Protein Data Bank (and Worldwide Protein Data Bank [wwPDB]) with accession codes 6RJF (control E1) and 6O06 (expanded E1). The raw data have been deposited in the EMPIAR database (https://www.ebi.ac.uk/pdbe/emdb/empiar/) with deposition EMPIAR-10284.

ACKNOWLEDGMENTS

We thank Benita Löflund and Pasi Laurinmäki (University of Helsinki), as well as Instruct-FI, the Biocenter Finland National cryo-electron microscopy unit, HILiFE-Institute of Biotechnology, and the CSC-IT Center for Science Ltd., for providing technical assistance and facilities to carry out the work. We also thank Tino Kantoluoto (University of Jyväskylä) for virus production and purification.

This work was supported by the Academy of Finland (275199 and 315950 to S.J.B.; 257125 to V.M.), the Sigrid Juselius Foundation (S.J.B.), and Jane and Aatos Erkko foundation (V.M.).

V.M., V.R., A.D., and S.J.B. conceptualized the study. M.P., A.D., V.R., S.J.B., and V.M. curated data. M.P., V.R., M.L., A.D., S.J.B., and V.M. developed the methodology. V.R. and A.D. validated the data. V.R. and A.D. visualized the data. V.R., M.L., A.D., S.J.B., and V.M. wrote the manuscript. V.M. and S.J.B. acquired funding. A.D., S.J.B., and V.M. supervised the study. S.J.B. and V.M. served as project administrators.

REFERENCES

1. Kahrs CR, Chuda K, Tapia G, Stene LC, Marild K, Rasmussen T, Ronningen KS, Lundin Kea Kramna L, Cinek O, Stordal K. 2019. Enterovirus as trigger of coeliac disease: nested case-control study within prospective birth cohort. BMJ 364:l231. https://doi.org/10.1136/bmj.l231.
2. Roivainen M, Klingel K. 2009. Role of enteroviruses in the pathogenesis of type 1 diabetes. Diabetologia 52:995–996. https://doi.org/10.1007/s00125-009-1332-9.
3. Laitinen OH, Honkanen H, Pakkanen O, Oikarinen S, Hankaniemi MM, Huhtala H, Ruokoranta T, Lecouturier V, Andre P, Harju R, Virtanen SM, Lehtonen J, Almond JW, Simell T, Simell O, Ilonen J, Veijola R, Knip M, Hyoty H. 2014. Coxsackievirus B1 is associated with induction of beta-cell autoimmunity that portends type 1 diabetes. Diabetes 63:446–455. https://doi.org/10.2337/db13-0619.
4. Sioofy-Khojine A-B, Lehtonen J, Nurminen N, Laitinen OH, Oikarinen S, Huhtala H, Pakkanen O, Ruokoranta T, Hankaniemi MM, Toppari J, Vähä-Mäkilä M, Ilonen J, Veijola R, Knip M, Hyöty H. 2018. Coxsackievirus B1 infections are associated with the initiation of insulin-driven autoimmunity that progresses to type 1 diabetes. Diabetologia 61:1193–1202. https://doi.org/10.1007/s00125-018-4561-y.
5. Nurani G, Lindqvist B, Casasnovas JM. 2003. Receptor priming of major group human rhinoviruses for uncoating and entry at mild low-pH environments. J Virol 77:11985–11991. https://doi.org/10.1128/jvi.77.22.11985-11991.2003.
6. Brabec M, Baravalle G, Blaas D, Fuchs R. 2003. Conformational changes, plasma membrane penetration, and infection by human rhinovirus type 2: role of receptors and low pH. J Virol 77:5370–5377. https://doi.org/10.1128/JVI.77.9.5370-5377.2003.
7. Karjalainen M, Kakkonen E, Upla P, Paloranta H, Kankaanpaa P, Liberali P, Renkema GH, Hyypia T, Heino J, Marjomaki V. 2008. A Raft-derived, Pak1-regulated entry participates in alpha2beta1 integrin-dependent sorting to caveosomes. Mol Biol Cell 19:2857–2869. https://doi.org/10.1091/mbc.e07-10-1094.
8. Karjalainen M, Rintanen N, Lehkonen M, Kallio K, Maki A, Hellstrom K, Siljamaki V, Upla P, Marjomaki V. 2011. Echovirus 1 infection depends on biogenesis of novel multivesicular bodies. Cell Microbiol 13:1975–1995. https://doi.org/10.1111/j.1462-5822.2011.01685.x.
9. Marjomaki V, Pietiainen V, Matilainen H, Upla P, Ivaska J, Nissinen L, Reunanen H, Huttunen P, Hyypia T, Heino J. 2002. Internalization of echovirus 1 in caveolae. J Virol 76:1856–1865. https://doi.org/10.1128/jvi.76.4.1856-1865.2002.
10. Heikkila O, Susi P, Tevaluoto T, Harma H, Marjomaki V, Hyypia T, Kiljunen S. 2010. Internalization of coxsackievirus A9 is mediated by β2-

microglobulin, dynamin, and Arf6 but not by caveolin-1 or clathrin. J Virol 84:3666–3681. https://doi.org/10.1128/JVI.01340-09.
11. Soonsawad P, Paavolainen L, Upla P, Weerachatyanukul W, Rintanen N, Espinoza J, McNerney G, Marjomaki V, Cheng RH. 2014. Permeability changes of integrin-containing multivesicular structures triggered by picornavirus entry. PLoS One 9:e108948. https://doi.org/10.1371/journal.pone.0108948.
12. Huttunen M, Waris M, Kajander R, Hyypia T, Marjomaki V. 2014. Coxsackievirus A9 infects cells via nonacidic multivesicular bodies. J Virol 88:5138–5151. https://doi.org/10.1128/JVI.03275-13.
13. Marjomaki V, Turkki P, Huttunen M. 2015. Infectious entry pathway of enterovirus B species. Viruses 7:6387–6399. https://doi.org/10.3390/v7122945.
14. Myllynen M, Kazmertsuk A, Marjomaki V. 2016. A novel open and infectious form of echovirus 1. J Virol 90:6759–6770. https://doi.org/10.1128/JVI.00342-16.
15. Tuthill TJ, Groppelli E, Hogle JM, Rowlands DJ. 2010. Picornaviruses. Curr Top Microbiol Immunol 343:43–89. https://doi.org/10.1007/82_2010_37.
16. Casasnovas JM, Springer TA. 1994. Pathway of rhinovirus disruption by soluble intercellular adhesion molecule 1 (ICAM-1): an intermediate in which ICAM-1 is bound and RNA is released. J Virol 68:5882–5889.
17. Kaplan G, Freistadt MS, Racaniello VR. 1990. Neutralization of poliovirus by cell receptors expressed in insect cells. J Virol 64:4697–4702.
18. Prchla E, Kuechler E, Blaas D, Fuchs R. 1994. Uncoating of human rhinovirus serotype 2 from late endosomes. J Virol 68:3713–3723.
19. Curry S, Chow M, Hogle JM. 1996. The poliovirus 135S particle is infectious. J Virol 70:7125–7131.
20. Ren J, Wang X, Hu Z, Gao Q, Sun Y, Li X, Porta C, Walter TS, Gilbert RJ, Zhao Y, Axford D, Williams M, McAuley K, Rowlands DJ, Yin W, Wang J, Stuart DI, Rao Z, Fry EE. 2013. Picornavirus uncoating intermediate captured in atomic detail. Nat Commun 4:1929. https://doi.org/10.1038/ncomms2889.
21. Ward T, Powell RM, Chaudhry Y, Meredith J, Almond JW, Kraus W, Nelsen-Salz B, Eggers HJ, Evans DJ. 2000. Fatty acid-depleted albumin induces the formation of echovirus A particles. J Virol 74:3410–3412. https://doi.org/10.1128/jvi.74.7.3410-3412.2000.
22. Lonberg-Holm K, Gosser LB, Shimshick EJ. 1976. Interaction of liposomes with subviral particles of poliovirus type 2 and rhinovirus type 2. J Virol 19:746–749.
23. Cords CE, James CG, McLaren LC. 1975. Alteration of capsid proteins of coxsackievirus A13 by low ionic concentrations. J Virol 15:244–252.
24. Wetz K, Kucinski T. 1991. Influence of different ionic and pH environments on structural alterations of poliovirus and their possible relation to virus uncoating. J Gen Virol 72:2541–2544. https://doi.org/10.1099/0022-1317-72-10-2541.
25. Ward T, Powell RM, Evans DJ, Almond JW. 1999. Serum albumin inhibits echovirus 7 uncoating. J Gen Virol 80:283–290. https://doi.org/10.1099/0022-1317-80-2-283.
26. Butan C, Filman DJ, Hogle JM. 2014. Cryo-electron microscopy reconstruction shows poliovirus 135S particles poised for membrane interaction and RNA release. J Virol 88:1758–1770. https://doi.org/10.1128/JVI.01949-13.
27. Lin J, Cheng N, Hogle JM, Steven AC, Belnap DM. 2013. Conformational shift of a major poliovirus antigen confirmed by immuno-cryogenic electron microscopy. J Immunol 191:884–891. https://doi.org/10.4049/jimmunol.1202014.
28. Lee H, Shingler KL, Organtini LJ, Ashley RE, Makhov AM, Conway JF, Hafenstein S. 2016. The novel asymmetric entry intermediate of a picornavirus captured with nanodiscs. Sci Adv 2:e1501929. https://doi.org/10.1126/sciadv.1501929.
29. Organtini LJ, Makhov AM, Conway JF, Hafenstein S, Carson SD. 2014. Kinetic and structural analysis of coxsackievirus B3 receptor interactions and formation of the A-particle. J Virol 88:5755–5765. https://doi.org/10.1128/JVI.00299-14.
30. Pickl-Herk A, Luque D, Vives-Adrian L, Querol-Audi J, Garriga D, Trus BL, Verdaguer N, Blaas D, Caston JR. 2013. Uncoating of common cold virus is preceded by RNA switching as determined by X-ray and cryo-EM analyses of the subviral A-particle. Proc Natl Acad Sci U S A 110:20063–20068. https://doi.org/10.1073/pnas.1312128110.
31. Shingler KL, Yoder JL, Carnegie MS, Ashley RE, Makhov AM, Conway JF, Hafenstein S. 2013. The enterovirus 71 A-particle forms a gateway to allow genome release: a cryoEM study of picornavirus uncoating. PLoS Pathog 9:e1003240. https://doi.org/10.1371/journal.ppat.1003240.
32. Strauss M, Filman DJ, Belnap DM, Cheng N, Noel RT, Hogle JM. 2015. Nectin-like interactions between poliovirus and its receptor trigger conformational changes associated with cell entry. J Virol 89:4143–4157. https://doi.org/10.1128/JVI.03101-14.
33. Lin J, Lee LY, Roivainen M, Filman DJ, Hogle JM, Belnap DM. 2012. Structure of the Fab-labeled "breathing" state of native poliovirus. J Virol 86:5959–5962. https://doi.org/10.1128/JVI.05990-11.
34. Gerasimenko JV, Tepikin AV, Petersen OH, Gerasimenko OV. 1998. Calcium uptake via endocytosis with rapid release from acidifying endosomes. Curr Biol 8:1335–1338. https://doi.org/10.1016/S0960-9822(07)00565-9.
35. Christensen KA, Myers JT, Swanson JA. 2002. pH-dependent regulation of lysosomal calcium in macrophages. J Cell Sci 115:599–607.
36. Weinert S, Jabs S, Supanchart C, Schweizer M, Gimber N, Richter M, Rademann J, Stauber T, Kornak U, Jentsch TJ. 2010. Lysosomal pathology and osteopetrosis upon loss of H^+-driven lysosomal Cl^- accumulation. Science 328:1401–1403. https://doi.org/10.1126/science.1188072.
37. Hara-Chikuma M, Yang B, Sonawane ND, Sasaki S, Uchida S, Verkman AS. 2005. ClC-3 chloride channels facilitate endosomal acidification and chloride accumulation. J Biol Chem 280:1241–1247. https://doi.org/10.1074/jbc.M407030200.
38. Steinberg BE, Huynh KK, Brodovitch A, Jabs S, Stauber T, Jentsch TJ, Grinstein S. 2010. A cation counterflux supports lysosomal acidification. J Cell Biol 189:1171–1186. https://doi.org/10.1083/jcb.200911083.
39. Scott CC, Gruenberg J. 2011. Ion flux and the function of endosomes and lysosomes: pH is just the start: the flux of ions across endosomal membranes influences endosome function not only through regulation of the luminal pH. Bioessays 33:103–110. https://doi.org/10.1002/bies.201000108.
40. Pfeiffer P, Herzog M, Hirth L. 1976. RNA viruses: stabilization of brome mosaic virus. Philos Trans R Soc Lond B Biol Sci 276:99–107. https://doi.org/10.1098/rstb.1976.0100.
41. Hull R. 1978. The stabilization of the particles of turnip rosette virus. III. Divalent cations. Virology 89:418–422. https://doi.org/10.1016/0042-6822(78)90184-8.
42. Bishop NE, Anderson DA. 1997. Early interactions of hepatitis A virus with cultured cells: viral elution and the effect of pH and calcium ions. Arch Virol 142:2161–2178. https://doi.org/10.1007/s007050050233.
43. Kivela HM, Mannisto RH, Kalkkinen N, Bamford DH. 1999. Purification and protein composition of PM2, the first lipid-containing bacterial virus to be isolated. Virology 262:364–374. https://doi.org/10.1006/viro.1999.9838.
44. Sherman MB, Guenther RH, Tama F, Sit TL, Brooks CL, Mikhailov AM, Orlova EV, Baker TS, Lommel SA. 2006. Removal of divalent cations induces structural transitions in *Red clover necrotic mosaic virus*, revealing a potential mechanism for RNA release. J Virol 80:10395–10406. https://doi.org/10.1128/JVI.01137-06.
45. Speir JA, Munshi S, Wang G, Baker TS, Johnson JE. 1995. Structures of the native and swollen forms of cowpea chlorotic mottle virus determined by X-ray crystallography and cryo-electron microscopy. Structure 3:63–78. https://doi.org/10.1016/S0969-2126(01)00135-6.
46. van der Vusse GJ. 2009. Albumin as fatty acid transporter. Drug Metab Pharmacokinet 24:300–307. https://doi.org/10.2133/dmpk.24.300.
47. Smyth M, Pettitt T, Symonds A, Martin J. 2003. Identification of the pocket factors in a picornavirus. Arch Virol 148:1225–1233. https://doi.org/10.1007/s00705-002-0974-4.
48. Filman DJ, Wien MW, Cunningham JA, Bergelson JM, Hogle JM. 1998. Structure determination of echovirus 1. Acta Crystallogr D Biol Crystallogr 54:1261–1272. https://doi.org/10.1107/s0907444998002790.
49. Liu Y, Sheng J, van Vliet ALW, Buda G, van Kuppeveld FJM, Rossmann MG. 2018. Molecular basis for the acid-initiated uncoating of human enterovirus D68. Proc Natl Acad Sci U S A 115:E12209–E12217. https://doi.org/10.1073/pnas.1803347115.
50. Abdelmagid SA, Clarke SE, Nielsen DE, Badawi A, El-Sohemy A, Mutch DM, Ma DW. 2015. Comprehensive profiling of plasma fatty acid concentrations in young healthy Canadian adults. PLoS One 10:e0116195. https://doi.org/10.1371/journal.pone.0116195.
51. Penn AH, Dubick MA, Torres Filho IP. 2017. Fatty acid saturation of albumin used in resuscitation fluids modulates cell damage in shock: *in vitro* results using a novel technique to measure fatty acid binding capacity. Shock 48:449–458. https://doi.org/10.1097/SHK.0000000000000865.
52. Xing L, Huhtala M, Pietiainen V, Kapyla J, Vuorinen K, Marjomaki V, Heino J, Johnson MS, Hyypia T, Cheng RH. 2004. Structural and functional analysis of integrin $_{alpha2}$I domain interaction with echovirus 1. J Biol Chem 279:11632–11638. https://doi.org/10.1074/jbc.M312441200.

53. Trigatti BL, Gerber GE. 1995. A direct role for serum albumin in the cellular uptake of long-chain fatty acids. Biochem J 308:155–159. https://doi.org/10.1042/bj3080155.
54. Martikainen M, Salorinne K, Lahtinen T, Malola S, Permi P, Hakkinen H, Marjomaki V. 2015. Hydrophobic pocket targeting probes for enteroviruses. Nanoscale 7:17457–17467. https://doi.org/10.1039/C5NR04139B.
55. Staring J, von Castelmur E, Blomen VA, van den Hengel LG, Brockmann M, Baggen J, Thibaut HJ, Nieuwenhuis J, Janssen H, van Kuppeveld FJ, Perrakis A, Carette JE, Brummelkamp TR. 2017. PLA2G16 represents a switch between entry and clearance of *Picornaviridae*. Nature 541:412–416. https://doi.org/10.1038/nature21032.
56. Baggen J, Thibaut HJ, Strating JRPM, van Kuppeveld FJM. 2018. The life cycle of non-polio enteroviruses and how to target it. Nat Rev Microbiol 16:368–381. https://doi.org/10.1038/s41579-018-0005-4.
57. Siljamaki E, Rintanen N, Kirsi M, Upla P, Wang W, Karjalainen M, Ikonen E, Marjomaki V. 2013. Cholesterol dependence of collagen and echovirus 1 trafficking along the novel alpha2beta1 integrin internalization pathway. PLoS One 8:e55465. https://doi.org/10.1371/journal.pone.0055465.
58. Huttunen M, Turkki P, Maki A, Paavolainen L, Ruusuvuori P, Marjomaki V. 2017. Echovirus 1 internalization negatively regulates epidermal growth factor receptor downregulation. Cell Microbiol 19:e12671. https://doi.org/10.1111/cmi.12671.
59. Upla P, Marjomaki V, Nissinen L, Nylund C, Waris M, Hyypia T, Heino J. 2008. Calpain 1 and 2 are required for RNA replication of echovirus 1. J Virol 82:1581–1590. https://doi.org/10.1128/JVI.01375-07.
60. Draper DE. 2004. A guide to ions and RNA structure. RNA 10:335–343. https://doi.org/10.1261/rna.5205404.
61. Hendry E, Hatanaka H, Fry E, Smyth M, Tate J, Stanway G, Santti J, Maaronen M, Hyypia T, Stuart D. 1999. The crystal structure of coxsackievirus A9: new insights into the uncoating mechanisms of enteroviruses. Structure 7:1527–1538. https://doi.org/10.1016/S0969-2126(00)88343-4.
62. Muckelbauer JK, Kremer M, Minor I, Diana G, Dutko FJ, Groarke J, Pevear DC, Rossmann MG. 1995. The structure of coxsackievirus B3 at 3.5 Å resolution. Structure 3:653–667. https://doi.org/10.1016/S0969-2126(01)00201-5.
63. Arnold E, Rossmann MG. 1990. Analysis of the structure of a common cold virus, human rhinovirus 14, refined at a resolution of 3.0 Å. J Mol Biol 211:763–801. https://doi.org/10.1016/0022-2836(90)90076-X.
64. Hadfield AT, Lee W, Zhao R, Oliveira MA, Minor I, Rueckert RR, Rossmann MG. 1997. The refined structure of human rhinovirus 16 at 2.15 Å resolution: implications for the viral life cycle. Structure 5:427–441. https://doi.org/10.1016/S0969-2126(97)00199-8.
65. Kalynych S, Palkova L, Plevka P. 2016. The structure of human parechovirus 1 reveals an association of the RNA genome with the capsid. J Virol 90:1377–1386. https://doi.org/10.1128/JVI.02346-15.
66. Domanska A, Flatt JW, Jukonen JJJ, Geraets JA, Butcher SJ. 2019. A 2.8-angstrom-resolution cryo-electron microscopy structure of human parechovirus 3 in complex with Fab from a neutralizing antibody. J Virol 93:e01597-18. https://doi.org/10.1128/JVI.01597-18.
67. Shakeel S, Evans JD, Hazelbaker M, Kao CC, Vaughan RC, Butcher SJ. 2018. Intrinsically disordered N termini in human parechovirus 1 capsid proteins bind encapsidated RNA. Sci Rep 8:5820. https://doi.org/10.1038/s41598-018-23552-7.
68. Schmidtke M, Schnittler U, Jahn B, Dahse H, Stelzner A. 2001. A rapid assay for evaluation of antiviral activity against coxsackie virus B3, influenza virus A, and herpes simplex virus type 1. J Virol Methods 95:133–143. https://doi.org/10.1016/S0166-0934(01)00305-6.
69. Zheng SQ, Palovcak E, Armache JP, Verba KA, Cheng Y, Agard DA. 2017. MotionCor2: anisotropic correction of beam-induced motion for improved cryo-electron microscopy. Nat Methods 14:331–332. https://doi.org/10.1038/nmeth.4193.
70. Zhang K. 2016. Gctf: Real-time CTF determination and correction. J Struct Biol 193:1–12. https://doi.org/10.1016/j.jsb.2015.11.003.
71. Scheres SH. 2012. RELION: implementation of a Bayesian approach to cryo-EM structure determination. J Struct Biol 180:519–530. https://doi.org/10.1016/j.jsb.2012.09.006.
72. Yang J, Yan R, Roy A, Xu D, Poisson J, Zhang Y. 2015. The I-TASSER Suite: protein structure and function prediction. Nat Methods 12:7–8. https://doi.org/10.1038/nmeth.3213.
73. Roy A, Kucukural A, Zhang Y. 2010. I-TASSER: a unified platform for automated protein structure and function prediction. Nat Protoc 5:725–738. https://doi.org/10.1038/nprot.2010.5.
74. Pettersen EF, Goddard TD, Huang CC, Couch GS, Greenblatt DM, Meng EC, Ferrin TE. 2004. UCSF Chimera–a visualization system for exploratory research and analysis. J Comput Chem 25:1605–1612. https://doi.org/10.1002/jcc.20084.
75. Emsley P, Lohkamp B, Scott WG, Cowtan K. 2010. Features and development of Coot. Acta Crystallogr D Biol Crystallogr 66:486–501. https://doi.org/10.1107/S0907444910007493.
76. Humphrey W, Dalke A, Schulten K. 1996. VMD: visual molecular dynamics. J Mol Graph 14:33. https://doi.org/10.1016/0263-7855(96)00018-5.
77. Phillips JC, Braun R, Wang W, Gumbart J, Tajkhorshid E, Villa E, Chipot C, Skeel RD, Kale L, Schulten K. 2005. Scalable molecular dynamics with NAMD. J Comput Chem 26:1781–1802. https://doi.org/10.1002/jcc.20289.
78. Trabuco LG, Villa E, Mitra K, Frank J, Schulten K. 2008. Flexible fitting of atomic structures into electron microscopy maps using molecular dynamics. Structure 16:673–683. https://doi.org/10.1016/j.str.2008.03.005.
79. Kucukelbir A, Sigworth FJ, Tagare HD. 2014. Quantifying the local resolution of cryo-EM density maps. Nat Methods 11:63–65. https://doi.org/10.1038/nmeth.2727.

IA

REAL-TIME FLUORESCENCE MEASUREMENT OF ENTEROVIRUS UNCOATING

by

Ruokolainen V., Laajala M. & Marjomäki V. 2020

Bio-protocol 10 (7) e3582

https://doi.org/10.21769/BioProtoc.3582

bio-protocol www.bio-protocol.org/e3582 Bio-protocol 10(07): e3582. DOI:10.21769/BioProtoc.3582

Real-time Fluorescence Measurement of Enterovirus Uncoating

Visa Ruokolainen, Mira Laajala and Varpu Marjomäki*

[1]Department of Biological and Environmental Science, Nanoscience Center, University of Jyväskylä, Jyväskylä, Finland
*For correspondence: varpu.s.marjomaki@jyu.fi

[Abstract] Viruses need to open, *i.e.*, uncoat, in order to release their genomes for efficient replication and translation. Especially for non-enveloped viruses, such as enteroviruses, the cues leading to uncoating are less well known. The status of the virus has previously been observed mainly by transmission electron microscopy using negative staining, cryo electron microscopy, X-ray crystallography or gradient separation (reviewed in Tuthill *et al.*, 2010, Myllynen *et al.*, 2016, Ruokolainen *et al.*, 2019). However, monitoring of uncoating has been limited by the lack of methods detecting dynamic changes of the virions. Here, we present a real-time fluorescence based protocol, which detects the viral genome (RNA) during various stages of uncoating *in vitro*, while RNA is still inside the particle that has been expanded before the actual RNA release, and when the RNA has been totally released from the viral particle. Our method allows to explore how various molecular factors may promote or inhibit virus uncoating.

Keywords: Picornavirus, Enterovirus, Uncoating, Genome, RNA, RNase, SYBR Green II, Fluorescence spectroscopy

[Background] In our previous study, we found that infectious intermediate echovirus 1 particle allows SYBR Green II, a RNA intercalating dye, to enter the virus particle (Myllynen *et al.*, 2016). This can be observed as an increase of fluorescence and the recorded fluorescence is not susceptible to RNase digestion (Myllynen *et al.*, 2016). Using this information, we developed a real-time method to monitor virus opening using the SYBR Green II dye and RNase in fluorescence spectroscopy. We could follow the fenestration of the particles in real-time at +37 °C, or other temperature of interest, in a 96-well plate format by adding SYBR Green II and factors triggering the uncoating, and observing the increase of SYBR Green II fluorescence. Addition of RNase into parallel wells allowed us to monitor the extent of RNA release from the virions, as RNase readily degrades RNA from the solution, but not from inside of the virion (RNAse cannot enter through the small fenestrations inside to the virus particle, Myllynen *et al.*, 2016). In case of intact virus particles, only very low amount of fluorescence was observed. As an example, in our previous study, a DPBS solution supplemented with 0.01% fatty acid free BSA produced high amounts of intermediate echovirus 1 particles. For more details see the original publication (Ruokolainen *et al.*, 2019).

Bio-protocol 10(07): e3582.
DOI:10.21769/BioProtoc.3582

Materials and Reagents

1. Pipette tips
2. Sarstedt 96-well plate (Sarstedt, catalog number: 83.3924) (or similar)
3. 1.5 ml tubes
4. Purified virus stock (1 µg of virus per measured well; stored at -80 °C)
   Purification of enteroviruses can be done using either 5-20% or 10-40% sucrose gradient and is described in detail in the original publication (Ruokolainen *et al.*, 2019). Also, CsCl purification may be used but it was observed by us to have more variation from batch-to-batch than sucrose purified virus. The protocol has been tested and observed to work with echovirus 1 and coxsackieviruses A9 and B3 suggesting its wide applicability for enteroviruses and probably for picornaviruses in general.
5. Buffer/solution of your interest
   In our paper we used a wide spectrum of concentrations of different ions and albumin to study the virus priming and opening. As an example, DPBS solution supplemented with 0.01% BSA resulted in high amount of intermediate virus particles.
6. SYBR Green II RNA gel stain (Invitrogen; ThermoFisher Scientific, catalog number S7564; stored at -20 °C)
7. RNase A, 10 mg/ml (ThermoFisher Scientific catalog number EN0531; stored at -20 °C)
8. 150 mM NaCl solution
9. Ice

Equipment

1. Pipette with a volume range including 100 µl
2. 8-channel multipipette with a volume range including 50 µl, or similar (optional)
3. Perkin Elmer 2030 Multilabel Reader Victor X4 (or similar fluorescence plate reader with suitable filter options)

Software

1. Perkin Elmer 2030 Manager
2. Microsoft Excel

Procedure

A. Sample preparation
   1. Place the 96-well plate on ice to cool down.

Bio-protocol 10(07): e3582.
DOI:10.21769/BioProtoc.3582

Note: You can use a metal plate on top of ice to make the surface even and the plate easy to handle.

2. Cool down the solution(s) of interest on ice.
3. Make 1:10 dilution from the 10,000x SYBR Green II stock solution. You can use ddH_2O or the solution of interest to make the dilution. If the solution of interest is very exactly defined, then preferably use it for the dilution to keep the conditions unchanged (as ddH_2O will change/dilute the solution). Avoid exposing the SYBR Green II to bright light.
4. Pipette 450 µl of the solution of interest into two 1.5 ml tubes. You can have many different solutions of interest in one 96-well plate measurement. *i.e.*, many pairs of 1.5 ml tubes. Up to seven different solutions of interest can be applied into one 96-well plate (see Figure 1 for example).

	1	2	3	4	5	6	7	8	9	10	11	12
A	x	x	x	x	x	x	x	x	x	x	x	x
B	x	Solution 1 +virus			-virus	S.1 +RNase +virus			-virus	S.2 +virus		x
C	x	-"-	-virus	2 +RNase +virus			-virus	3 +virus			-virus	x
D	x	3 +RNase +virus			-virus	4+virus			-virus	4+RNase+virus		x
E	x	-"-	-virus	5+virus			-virus	5+RNase+virus			-virus	x
F	x	6+virus			-virus	6+RNase+virus			-virus	7+virus		x
G	x	-"-	-virus	7+RNase+virus			-virus	x	x	x	x	x
H	x	x	x	x	x	x	x	x	x	x	x	x

Figure 1. Example of 96-well plate with 7 different solutions of interest (highlighted with different colors) and three replicates of virus with a background control without virus, all measured with and without RNase. Rows A and H, and columns 1 and 12 are left empty.

5. Add 4.5 µl of the previously diluted SYBR Green II into both 1.5 ml tubes.
6. Add 4.5 µl of the RNase A into one of the 1.5 ml tube in a final concentration of 10 µg/ml. Preferably use high concentrated stock to negate the buffer effect to the solution of interest. We use pre-diluted 1 mg/ml RNase stock in 150 mM NaCl, *i.e.*, 1 µl of RNase in 100 µl of solution of interest. Add 4.5 µl of 150 mM NaCl solution without RNase A into the other tube to keep the ion concentrations identical.
7. Mix the 1.5 ml tubes well and pipette 100 µl into four adjacent wells of the 96-well plate. Keep the plate on ice. Do not use rows A and H and columns 1 and 12 since the proximity of the plate edge might affect the measurement. See Figure 1 for an example. Avoid bubbles. Easiest way to avoid them is to use reverse pipetting for mixing and placing the liquid into the wells. In reverse pipetting, press the pipette cylinder all the way down before taking the adjusted volume inside the tip, resulting in extra volume inside the tip when mixing the solution. Then the volume only up to the first step is pipetted out in the well before sucking in the next volume *etc.* (For further details, see for example Good Laboratory Pipetting Guide https://assets.thermofisher.com/TFS-

Bio-protocol 10(07): e3582.
DOI:10.21769/BioProtoc.3582

Assets/LSG/brochures/D16542.pdf.)

8. Add 1 µg of virus into each of the three first wells of a solution and leave the fourth well without the virus to measure the background fluorescence of the solution. Somewhat lower virus amount, at least down to 0.5 µg, may also be applicable. However, if the solution of interest contains molecules that cause background fluorescence (such as BSA in our case) the signal-to-noise ratio might be low and the results less reliable. Also, preferably use a concentrated virus stock so that adding of the virus in a buffer will not change the chemical concentrations too much. On the other hand, too concentrated stock may add to the pipetting error. Optimal virus stock concentration would be around 1 µg/µl, *i.e.*, 1 µl of the virus stock would be added per well.
9. Mix the wells. Avoid bubbles. Easiest way is to use 8-channel multipipette and reverse pipetting.
10. Keep the plate on ice, cover with aluminium folio and transfer to the fluorescence plate reader.
11. Sample preparation in short:
    a. Take 450 µl of solution of interest in two 1.5 ml tubes, tube A and tube B. Keep the tubes on ice.
    b. Add 4.5 µl of pre-diluted 1,000x SYBR Green II in both tubes A and B.
    c. Add 4.5 µl of RNase A from 1 mg/ml stock only into tube B to a final concentration of 10 µg/ml.
    d. Mix both tubes carefully and transfer 100 µl of the solution into four adjacent wells from each tube, *i.e.*, 8 wells in total.
    e. Pipette 1 µg of virus into 3 first wells transferred from tube A and leave the fourth well without virus. Do the same for the wells transferred from tube B that has the RNase A.
    f. Mix well and avoid air bubbles. Protect from light, keep on ice and transfer to the measurement device.

B. Fluorescence measurement

1. Prepare a measuring protocol using appropriate filters to measure SYBR Green II. With the Perkin Elmer 2030 Multilabel Reader Victor X4 use CW-Lamp Filter F485 and emission filter F535. Use CW-Lamp energy of 14,592 (or similar value around 15,000) and counting time of 1 second. Use measurement height with “user defined” -option of 13 mm and Plate type of “Generic 8x12 size plate”. Save the protocol for later use.
2. Mark the wells to measure, measure each plate 90 times (Using 90 repeats and two-minute gap between the repeats results in total of 3-hour measurement. To use some other total measuring time adjust the field of “measure each plate” accordingly) and delay between repeats 0 s. Pre-run the protocol and time how long one round of measurements takes. To measure each well every two min, subtract the time taken by one round of measurements from 120 s and place the result into “delay between repeats” -field. For example, if the time to measure the wells in your experiment takes 30 s, subtract this from 120 s and place the resulting 90 s into “delay between repeats”. In this way the plate reader waits 90 s after the first round of measurements before starting to take the next ones and, as a result, every well is measured exactly every 2 min. Note,

Bio-protocol 10(07): e3582.
DOI:10.21769/BioProtoc.3582

that when changing the amount of wells in your measurement, the “delay between repeats” needs to be adjusted accordingly.

3. Pre-heat the plate reader to +37 °C or to any other temperature you wish to measure in. The plate reader takes some time to heat up, so do this before starting to prepare the samples and the plate.
4. Place the previously prepared plate inside the plate reader with the lid on, but without the aluminium folio.
5. Start the protocol.

C. Data handling

1. Export the data into Excel.
2. Subtract the fluorescence background of each solution at each time point from the fluorescence of the same solution with the virus. Do this for all three replicates.
3. Calculate average of the three replicates. Calculate the standard deviation and the standard error of the mean.
4. Plot the data into a graph.

Data analysis

After plotting the graphs, first of all the results with the same solution with and without RNase should be compared. Fluorescence without the RNase presents the fluorescence originating from the empty and expanded particles. Fluorescence with the RNase presents the fluorescence originating from the expanded particles and the difference between the conditions with and without RNase originates from the empty capsids. Also, a measurement in virus storage buffer, or in another stabile environment for the virus, should be performed to verify the stability status of the unmodified virus, which should result in low amount of fluorescence. After comparing the measurements with and without RNase in one solution, one can also compare the results between different solutions. At least the proportion of different virus states can be compared. See Figure 2 as an example of measurements monitoring stable virus (only small increase in fluorescence), virus priming (increased fluorescence and only small decrease of signal with RNase treatment) and virus opening (increased fluorescence but loss of fluorescence after RNase addition).

When comparing the absolute fluorescence values, one must remember that the fluorescence potency of SYBR Green II might be somewhat affected by the surrounding conditions. In order to verify the proportional share of different states of the virions, other methods are recommended such as negative staining with TEM or cryo-EM.

Bio-protocol 10(07): e3582.
DOI:10.21769/BioProtoc.3582

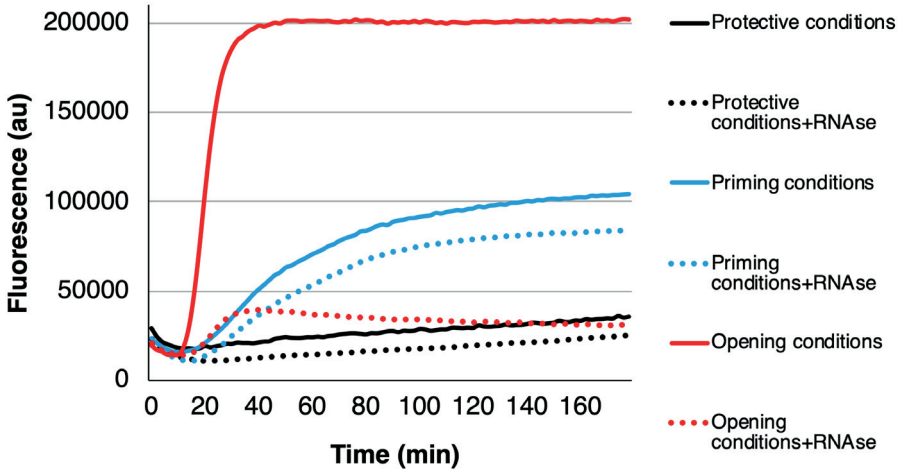

Figure 2. Example of three cases: protective conditions where the virus stays more or less unchanged (black curves), priming conditions where the virus mainly converts to primed and expanded intermediate form (blue curves), and opening conditions where the virus releases its RNA (red curves). For each condition, the fluorescence below the dotted line originates from the expanded particles since the RNase cannot enter inside the primed or intact particles, and the fluorescence from between the solid and dotted lines originates from the externalized genomes as the RNase abolishes the fluorescence.

Notes

Depending on the reproducibility of your virus purification, different batches of purified viruses might show different degree of virus priming and opening. Especially, we observed CsCl purified virus batches to have more variability than sucrose purified. Unpurified culture supernatants contain several contaminants that probably add into background fluorescence and lower the quality of the outcome and they might have also too low a virus concentration. For the reasons mentioned above, always verify the usability of a new batch of virus with some well known controls.

Acknowledgments

We acknowledge Jane and Aatos Erkko foundation and doctoral school of University of Jyväskylä for funding and the authors of the original paper (Ruokolainen *et al.*, 2019) for contributing to the work where the protocol was introduced. We also want thank all the Marjomäki group members for contributing to the production and purification of different enteroviruses used in the work.

Competing interests

There are no competing interests by the authors of this article.

Bio-protocol 10(07): e3582.
DOI:10.21769/BioProtoc.3582

References

1. Myllynen, M., Kazmertsuk, A. and Marjomäki, V. (2016). A novel open and infectious form of echovirus 1. *J Virol* 90(15): 6759-6770.
2. Ruokolainen, V., Domanska, A., Laajala, M., Pelliccia, M., Butcher, S. J. and Marjomaki, V. (2019). Extracellular albumin and endosomal ions prime enterovirus particles for uncoating that can be prevented by fatty acid saturation. *J Virol* 93(17).
3. Tuthill, T. J., Groppelli, E., Hogle, J.M. and Rowlands, D. J. (2010). Picornaviruses. In: Johnson, J. (Ed.). In: *Cell Entry by Non-Enveloped Viruses.* Current Topics in Microbiology and Immunology, vol 343. Springer, Berlin, Heidelberg.

II

ALBUMIN AND CATIONIC IONS CAN SEPERATELY PRIME COXSACKIEVIRUS A9 FOR UNCOATING

by

Domanska A., Ruokolainen V., Plavec Z., Löflund B., Soliymani R.,
Butcher S. J. & Marjomäki V

Request a copy from the author.

III

DEVELOPMENT OF FUNCTIONALIZED SYBR GREEN II RELATED CYANINE DYES FOR VIRAL RNA DETECTION

by

Saarnio V. K., Salorinne K., Ruokolainen V., Nilsson J. R., Tero T-R., Oikarinen S., Wilhelmsson L. M., Lahtinen T. M. & Marjomäki V. 2020

Dyes and Pigments. 177, 108282

https://doi.org/10.1016/j.dyepig.2020.108282

Dyes and Pigments 177 (2020) 108282

Contents lists available at ScienceDirect

Dyes and Pigments

journal homepage: http://www.elsevier.com/locate/dyepig

Development of functionalized SYBR green II related cyanine dyes for viral RNA detection

Ville K. Saarnio [a], Kirsi Salorinne [a], Visa P. Ruokolainen [b], Jesper R. Nilsson [c], Tiia-Riikka Tero [a], Sami Oikarinen [d], L. Marcus Wilhelmsson [c], Tanja M. Lahtinen [a,*], Varpu S. Marjomäki [b,**]

[a] Department of Chemistry, Nanoscience Center, Finland
[b] Department of Cell and Molecular Biology, Nanoscience Center, University of Jyväskylä, Jyväskylä, FI-40500, Finland
[c] Department of Chemistry and Chemical Engineering, Chemistry and Biochemistry, Chalmers University of Technology, Gothenburg, SE-41296, Sweden
[d] Faculty of Medicine and Life Sciences, University of Tampere, Tampere, FI-33014, Finland

ARTICLE INFO

Keywords:
Cyanines
Nucleic acids
Fluorescent probes
RNA recognition
Host-guest systems
Viruses

ABSTRACT

Fluorescent probes for sensing nucleic acids have found widespread use in the field of cell and molecular biology. However, probes combined with potential for post-synthetic conjugation, *e.g.* for intra-endosomal measurements of RNA, are unavailable. Herein we developed cyanine dyes that can be conjugated to viral capsid or other targets. First, we solved the crystal structure of SYBR Green II. The structural elucidation of this commonly used RNA probe provided the basis for synthesizing similar molecules with much desired function for post-synthetic conjugation. To address this need, cyanine dyes were prepared using an alternative synthesis protocol. All studied compounds showed considerable brightness upon binding to nucleic acids. However, regardless of the common chromophore on the dyes, the observed fluorescence emission intensities varied significantly, where methyl-substituted dye **1** gave values higher than SYBR Green II, whereas compounds **2**–**5** containing undecyl spacers had lower values. Studying the structure-activity relationship revealed the longer alkyl chains to induce slight perturbation in dye intercalation, as well as demand larger binding area on the nucleic acid lattice, explaining these differences. To study the potential biological use of the dyes, the RNA genome of enterovirus echovirus 1 was studied *in vitro* with the probes. A novel method employing the low binding space requirement of **1** was developed to determine the single-to-double-stranded RNA ratio of a sample, whereas compound **4** was covalently bound to the viral capsid and used successfully to monitor the viral RNA release from within the capsid. The presented results open new possibilities for preparation and use of SYBR Green-based nucleic acid probes to further apply these compounds for increasingly demanding targeting in biological contexts.

1. Introduction

Many fluorescent probes for sensing nucleic acids are available nowadays. However, targeting possibilities for excluding interfering background signal from the molecules of interest remain suboptimal. For example, tools for sensing viral RNA from the background DNA/RNA present in a cellular environment are lacking. For such detection, a combination of light-up upon target binding and control over localization is desired. Cyanine dyes are defined as an organic molecule containing two nitrogen substituted heterocycles sharing a cationic charge through a polymethine bridge [1]. They are usually prepared with classical cyanine condensation reactions between two quaternary amine salts [2]. Among their widespread applications, one of particular interest is their use as fluorescent probes [3]. For example, the Cy-family of symmetrical cyanine dyes is widely employed in different biological applications [4]. Most of these compounds have molar absorptivities in the magnitude of 10^4–10^5 $cm^{-1}M^{-1}$, with different compounds covering the whole visible light spectrum [2]. However, arguably the most important application of these compounds as fluorophores has been the use of unsymmetrical dyes for detection of nucleic acids through non-covalent binding, exhibiting an up to 1000-fold increase in fluorescence intensity upon binding [1]. A well-studied example from such dyes exhibiting this behavior is the thiazole orange (TO), consisting of monomethine bridged benzothiazolium and quinolinium units [5]. TO

* Corresponding author.
** Corresponding author.
E-mail addresses: tanja.m.lahtinen@jyu.fi (T.M. Lahtinen), varpu.s.marjomaki@jyu.fi (V.S. Marjomäki).

https://doi.org/10.1016/j.dyepig.2020.108282
Received 15 November 2019; Received in revised form 17 January 2020; Accepted 13 February 2020
Available online 15 February 2020

together with oxazole yellow (YO) and their homodimers (TOTO and YOYO) have served as a foundation for continuous development of these dyes [6–10]. The research on these dyes has also led to a wide range of commercially available nucleic acid stains [11]. Important and widely used commercial fluorophores include SYBR Green I, SYBR Green II, SYBR Safe, SYBR Gold and PicoGreen. While the chemical structures of PicoGreen [12], SYBR Safe [13] and SYBR Green I [12] have been reported, many routinely used compounds are still unknown [11]. A common descriptor for these dyes is their ability to interact with DNA and RNA, by intercalation [14].

Intercalators bind to double-stranded nucleic acids by assuming a planar conformation and inserting between stacked basepairs, forming π-π interactions with the target [14]. The reason for the great fluorescence enhancement is thought to be the result of restriction of the torsional motion of the molecule [15]. The group of Geddes [16,17] has shown that both PicoGreen and SYBR Green I form a similar complex with dsDNA, in which the aromatic quinolinium core unit intercalates into the dsDNA, while the benzothiazolium unit, carrying a localized positive charge enhances the binding affinity by providing additional electrostatic interactions with the DNA backbone. In addition, the dimethylaminopropyl side chains are positioned in the minor groove of the DNA for added stability of the complex [16,17]. However, knowledge on this family of dyes is mostly based on very few examples. Thus, understanding the structural and binding properties of the dye molecules is highly important when studying their binding and interaction with RNA or DNA. It is also crucial for future development of more selective, efficient and versatile dyes that enable the study of more complex biological systems, such as viruses and their mode of action in living cells.

The development of cyanine dyes for selective binding to nucleic acids has enabled the quantification of RNA or DNA content in various biological samples, and inspired their use as fluorescent probes in cell and molecular biology [18]. Nowadays, visualization of nucleic acids in electrophoresis gels using such dyes is performed routinely in cell and molecular biology laboratories [19]. Additionally, recent developments have enabled increasingly selective detection of different base content or secondary structure of nucleic acids [20,21]. However, imaging of larger macromolecular assemblies containing nucleic acids, such as RNA-containing viruses upon internalization into cells, is more challenging due to lower number of viruses in endosomes against a high background of messenger and transfer RNA in the cytoplasm. In addition, dynamic imaging of virus opening in cellular vesicles, a key step during infection, is problematic due to difficulties in targeting the dye to the same structures exclusively. The presently available dyes such as SYBR Green II are hydrophobic and easily cross all cellular membranes thus labeling all RNA in the cell. For successful imaging of *e.g.* virus particles in endosomes, one needs to have a nucleic acid detecting dye which can be conjugated to the virus or a suitable solid support to be endocytosed to the same structures, and not leaking to the cytoplasm. In addition, an optimal dye should also be highly specific for nucleic acids over other contaminating background material, sufficiently high in brightness for imaging by microscopy techniques, and low in cytotoxicity when working with living cells.

The aim of this work was to create cyanine dyes that can be covalently bound to the target material, such as virus capsids or nanoparticles for targeted RNA detection in microscopy imaging. As a basis for this, we used the widely employed RNA probe SYBR Green II after resolving its previously unknown chemical structure. Hence, the dyes synthesized in this work are all 2-thiol substituted and carry an oxazole moiety. A new synthetic pathway to produce similar such dyes was developed and five new compounds (**1**–**5**) were made. The rationale behind the use of a longer 11 carbon chain was to minimalize steric hindrance after conjugation. Spectroscopic evaluation of these dyes gave plausible explanations to the differences in brightness and revealed new information on the structure-activity relationships of these types of compounds. As a proof of principal, two of the most promising compounds **1** and **4** were applied in our case study, to probe the RNA genome of echovirus 1 (EV1), in novel ways impossible to implement with SYBR Green II.

2. Results and discussion

2.1. Synthesis and structural properties

The synthetic pathway designed and used to produce molecules is presented in Scheme 1. First the 2-quinolone **6** was chlorinated using phosphorus oxychloride [22] in order to produce chloroiminium ion **7**. To avoid any undesired side reactions with the thiols, the solvents were evaporated before the next step. For the nucleophilic substitution of the chlorine, the thiol was added together with triethylamine and mixed for 4–6 days at room temperature in dry dichloromethane. After this, the cyanine condensation was carried out as described by Karlsson *et al.* in order to obtain the desired products [8]. Despite the efforts made to avoid reactions with the methyl thiolate, compound **1** was obtained as a side product from each synthesis due to the active thiolate from benzoxazole **9**. The intermediates and products were separated with flash column chromatography and gave MeS **1** with 10%–15% and the other dyes with 10%–37% yields. Individual yields and synthetic details are presented in the SI. From compound **3** the NHS-ester **4** was synthesized with N-hydroxysuccinimide (NHS) using Steglich esterification [23]. As the carboxylic acid moiety **3** proved very difficult to work with due to apparent impurities in the product, the methyl ester **5** was produced in an identical manner using methanol instead of NHS.

The presented synthesis procedure is straightforward, giving 2-thiol substituted cyanine dyes in three steps. Although a limited number of derivatives were made, the synthesis should be applicable with any other thiol, provided the compound is not sensitive to the basic conditions of the cyanine condensation. The yields of desired products could be improved by for example employing a stronger base in the nucleophilic substitution step to further promote thiolate formation. The substitution of the leaving group could be used as an advantage by manipulating the benzoxazole **9** to already contain the desired arm moiety. The structures of the synthesized dyes and the commercial ones used as comparison are presented in Fig. 1.

While the structures of SYBR Green I and PicoGreen are known from literature, the structure of SYBR Green II was here elucidated through X-ray crystallography, together with MeS **1** (Fig. 2a and b). The only difference in structure between the MeS dye **1** and SYBR Green II is the different pendant arm on the molecule. Comparing the crystal structure of SYBR Green II (Fig. 2c and d) to SYBR Green I and PicoGreen, the thiazole moiety is replaced with an oxazole and the 2-substituent is a thiol instead of a tertiary amine. As a result, SYBR Green I and PicoGreen have two propyl chains attached to the chromophore whereas SYBR Green II only has a 2-(dimethylamino)-ethyl group as the single "arm" on the molecule. The crystallographic details of the two compounds are summarized in Tables S1–S3. Dyes **2**–**5** did not crystallize in similar conditions, presumably due to the long alkyl chains hindering the crystal lattice formation. The functional group of the pendant arm affects the charge of the molecule. At slightly acidic pH, the *N*-2-(dimethylamino)-ethylthiolate arm of SYBR Green II can take on an additional positive charge by protonation of the amino group. This significantly improves the water solubility of the dye in comparison to the MeS dye **1**, as observed in the UV–vis measurements presented below.

2.2. Chromophore and binding properties

The structure of the chromophore unit of SYBR Green I related compounds is known from literature, and we discovered the structure of SYBR Green II to differ only by two hetero atoms (Fig. 1). These minor structural differences lead to a hypsochromic shift in the absorption of SYBR Green II compared to SYBR Green I, as shown in Fig. 3. The novel dyes presented in this work display absorption spectra that are similar to

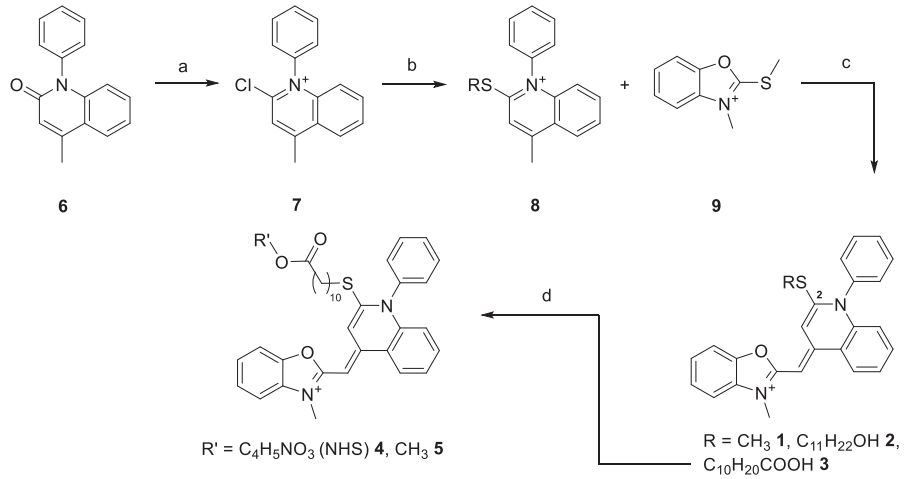

Scheme 1. Synthesis scheme for SYBR Green II related compounds. Reagents: a) $POCl_3$, 1,2-DCE, Δ; b) HSR (R = $C_{11}H_{22}OH$, $C_{10}H_{20}COOH$), Et_3N, DCM c) Et_3N, DCM d) DCC, DMAP and methanol or N-hydroxysuccinimide.

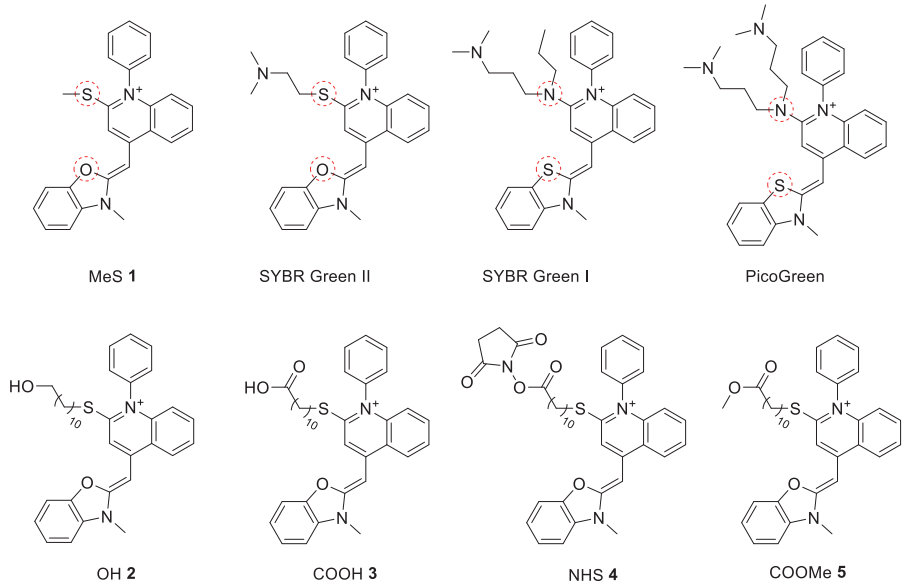

Fig. 1. Structures of the synthesized dyes (**1**–**5**). The structures of SYBR Green I, SYBR Green II and PicoGreen are shown for reference. The structural differences on the chromophores of the commercial dyes and MeS **1** are highlighted. (For interpretation of the references to color in this figure legend, the reader is referred to the Web version of this article.)

each other and to that of SYBR Green II. The differences in spectral characteristics can thus be attributed to the differences in the indoline (S *vs.* O) and the arm-binding hetero atom (N *vs.* S) shown with red circles in Fig. 1. Given the structural similarity, it would be expected that these molecules have molar absorptivities similar to that of SYBR Green II. Initial attempts to determine the molar absorptivity for the synthesized molecules (**1**–**5**) in TE buffer did, however, result in significantly different values for each dye. This is explained by the formation of aggregates (most likely H-type) and was particularly notable for the dyes aimed for biofunctionalization (**2**–**5**), as evidenced by scattering and hypsochromically shifted shoulders in the absorption spectra caused by H-aggregates (see Figs. S8–S12). The problem of aggregation was circumvented by changing the solvent to DCM (Table 1).

While the absorption characteristics of different dyes greatly impact their brightness, it is equally important to evaluate the binding properties of said dyes. One way to gain insight on the orientation of molecules in a ligand-substrate interaction is to employ flow-oriented linear dichroism (LD). A short introduction to the method is presented in the SI page 7. To determine the binding mode to double-stranded DNA and investigate if the attachment of an alkyl-linker to the ligands affects the binding characteristics, LD was measured on the synthesized dyes. The alkyl-containing compounds, MeS **1**, OH **2**, NHS **4**, and COOMe **5** (see Fig. 1 for structures) were included in the LD-analysis. LD^r at 260 nm for a sample containing only DNA ($\theta = 90°$ for DNA bases in B-form duplex) was used to determine the orientation factor (found to be $S = 0.017$, Fig. 4). When studying the samples containing both DNA and ligand, using identical shear flow orientation conditions as for only DNA, a distinct negative LD band corresponding to the lowest energy electronic transition (centered at 484 nm, Fig. 4, middle panel) was observed for MeS **1**, OH **2**, and NHS **4**. For COOMe **5**, only a very weak overall LD signal was observed, also appearing as a negative band in the 480 nm region (data not shown). The weak LD signal for **5** is likely

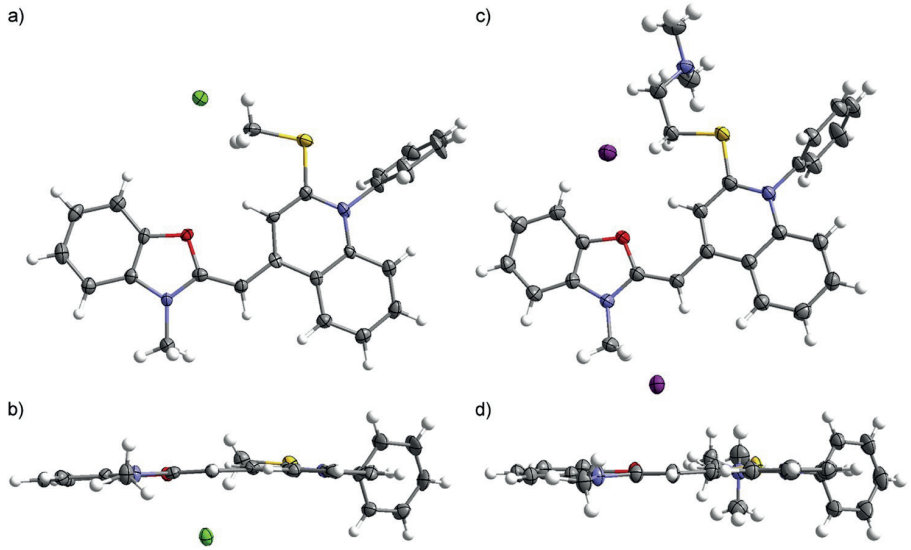

Fig. 2. Ortep drawing at 50% probability level of the crystal structure of MeS dye **1** shown from a) top and b) side views, and of SYBR Green II shown from c) top and d) side views. Element colors: carbon = grey, hydrogen = white, oxygen = red, nitrogen = blue, sulfur = yellow, chlorine = green and iodine = purple. (For interpretation of the references to color in this figure legend, the reader is referred to the Web version of this article.)

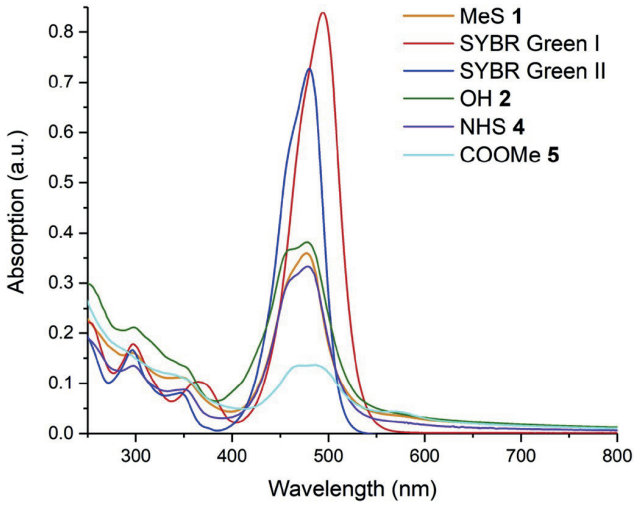

Fig. 3. UV–vis spectrum of MeS **1**, OH **2**, NHS **4** and COOMe **5** measured in TE Buffer at 19.6 μM concentration together with SYBR Green I and SYBR Green II at 1:1000 dilution from their respective stock solutions. (For interpretation of the references to color in this figure legend, the reader is referred to the Web version of this article.)

Table 1
Molar absorptivity measured in TE buffer and DCM at their lowest energy absorption maxima (*ca.* 478 nm) derived from Figs. S26 and S27.

Solvent	MeS **1**	OH **2**	NHS **4**	COOMe **5**	
TE buffer	19.2 ± 0.6	22.0 ± 0.5	18.5±0.2	7.9 ± 0.5	× 10^3 $cm^{-1}mol^{-1}$
Dichloromethane	31.1 ± 0.3	38.8 ± 0.5	30.3 ± 0.9	11.6 ± 0.4	

caused by poor compound solubility and aggregation in the aqueous solution, as evidenced by significant scattering in the isotropic absorption, hampering the evaluation of COOMe **5** under these experimental conditions. For MeS **1**, OH **2**, and NHS **4** LD^r at 484 nm, where the dye is the sole chromophore (with a transition dipole moment assumed to be in the plane of the essentially coplanar benzoxazolium and quinolinium heterocycles), was used to evaluate the binding angles relative to the DNA long axis. These were determined to be 86°, 70°, and 69° for MeS **1**, OH **2**, and NHS **4**, respectively. The calculated binding angles, in combination with the exclusively negative LD spectra, suggest DNA-binding by intercalation for the three analyzed compounds. It is noteworthy that OH **2** and NHS **4** (both having the alkyl linker) exhibit similar binding angles, yet lower than that of MeS **1**. This suggests that the binding mode of OH **2** and NHS **4** to DNA, although of evident intercalation character, is slightly affected by the presence of the attached linkers. From the

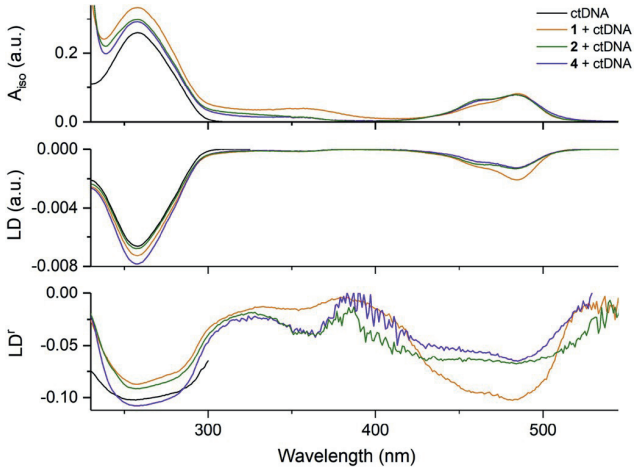

Fig. 4. Absorption and LD spectra of DNA in TE buffer with and without ligand. Concentration of DNA and ligand (where present) were 100 μM and 0.5 μM, respectively. DNA only (black line), DNA + MeS **1** (orange line), DNA + NHS **4** (violet line) and DNA + OH **2** (olive line). Top panel: Isotropic absorption. Middle panel: Linear dichroism. Bottom panel: Reduced linear dichroism (LD^r). Note that the difference in optical path length of the LD Couette cell (1 mm) and the cuvette used to determine A_{iso} (4 mm) was considered when calculating LD^r, *i.e.* $LD^r = 4 \times LD/A_{iso}$. (For interpretation of the references to color in this figure legend, the reader is referred to the Web version of this article.)

differences in binding angles it is conceivable that the linker participates in the binding by associating to one of the grooves of the DNA duplex, causing a slight displacement (tilt) of the ligand between the stacked bases and possibly also a slight distortion from exact coplanarity of the benzoxazolium and quinolinium moieties. This notion of a slight change in binding mode is further supported by the observed differences in binding constants and binding site size as described below. Understanding the impact the linking arms have on the nucleic acid binding modes of these dyes, before putting them into use in biological applications, is imperative.

For all synthesized compounds and SYBR Green II, the emission maximum wavelength was very close to 505 nm (Fig. 5), leading to compounds containing similar Stokes shifts in comparison to SYBR Green I. The emission maxima, when bound to fully double-stranded DNA remain the same, but as the portion of single-stranded nucleic acid is enhanced, increasing bathochromic shifts are also observed. This was observed as a small bathochromic shift to 515 nm when binding to cellular RNA (rRNA), while the fully linear 50 base ssDNA (liDNA) exhibits a significant shift to *ca.* 560 nm, as shown in Figs. S13–S18. Similar to the commercial dyes, the fluorescence of the synthesized dyes in solution without DNA was negligible, presumably due to non-radiative relaxation pathways (such as the rotation of the N-phenyl ring). Upon intercalation the fluorescence increases over a thousand-fold with SYBR Green I and similar enhancements are observed with the dyes prepared here (**1**–**5**). It is evident that higher intensity of emission was obtained for MeS **1** compared to SYBR Green II for all four types of nucleic acids used (see Fig. 6, Figs. S19, S20, and S22). These nucleic acids included rRNA, calf thymus DNA (ctDNA), bacterial double-stranded plasmid DNA (λDNA), liDNA and self-pairing hairpin forming 50 base ssDNA (hpDNA). SYBR Green I emits most strongly, but noticeably as the binding DNA gets more sterically demanding, the intensity difference compared to MeS dye **1** starts to diminish. This is clearly observed when moving from fully double-stranded DNA to rRNA, but the difference between SYBR Green I and MeS **1** gets significantly lower, when moving from ctDNA to hpDNA. The emission spectra of the dyes upon binding to liDNA (Fig. S13-S18, and S21) shows a large bathochromic shift compared to binding to the other nucleic acids but the intensity of this fluorescence remains small. The dyes containing longer 2-substituents seem to exhibit this characteristic more strongly, possibly indicating a different type of binding mode than intercalation that contributes to the lower energy emission. This suggestion is further supported by the divergence in intercalation angle observed for dyes **2** and **4** in the LD experiments. The emission intensities of thiol-substituted dyes stay proportional between each other with the different nucleic acids, whereas SYBR Green I experiences dramatic loss in emission when it is measured with nucleic acids that are not fully double-stranded. The fluorescence intensities of the long alkyl chain-containing dyes **2**, **4**, and **5** are significantly lower compared to the MeS dye **1**, yet still sufficiently bright to be applicable for the biological systems of interest here. In order to better understand the dye-nucleic acid interactions that lead to these differences in emission intensities with probes containing the same aromatic unit, a detailed analysis of fluorescence titration data was conducted, presented below.

Titration experiments conducted at pH 7.6 with each of the nucleic acids and plotting the highest values of emission intensity as the concentration increases gave binding isotherms for the interaction with dsDNA, displayed in Fig. 6 for ctDNA and Figs. S19–S22 for the other nucleic acids studied here. From this data it is possible to determine the binding constant to double-stranded DNA according to the methods employed by Dragan *et al.* for SYBR Green I [17] and PicoGreen [16]. In short, the theoretical expression for DNA-ligand interactions, McGhee von Hippel equation [24] for non-cooperative binding of ligands can be used to gain deeper insight into interactions between dyes and double-stranded nucleic acids:

$$v/L = K_a(1\text{-}nv)^n / (1\text{-}nv + v)^{n-1} \quad (1)$$

where v is binding density of ligands in DNA, L is unbound ligands, K_a is the binding constant for complex formation and n is the size of the binding site of ligand in base pairs. The formation of supramolecular complex between the dye and dsDNA is an equilibrium reaction as shown in equation (2):

$$\text{Dye} + \text{dsDNA} \rightleftarrows [\text{Dye:dsDNA}] \quad (2)$$

that can be described with the McGhee and Von Hippel equation [24]. From the binding isotherms, it is possible to express the fraction of dye molecules bound to DNA (θ) with the fraction of fluorescence observed (F) compared to fluorescence from 100% binding (F_b) as shown in equation (3):

$$\theta \approx F/F_b. \quad (3)$$

The F_b was obtained from titration of dyes to high excess of DNA and the resulting linear behavior (Fig. S23). Equation (3) ignores the effect of non-bound dye to the fluorescence, which is reasonable as its contribution is negligible in all cases presented here.

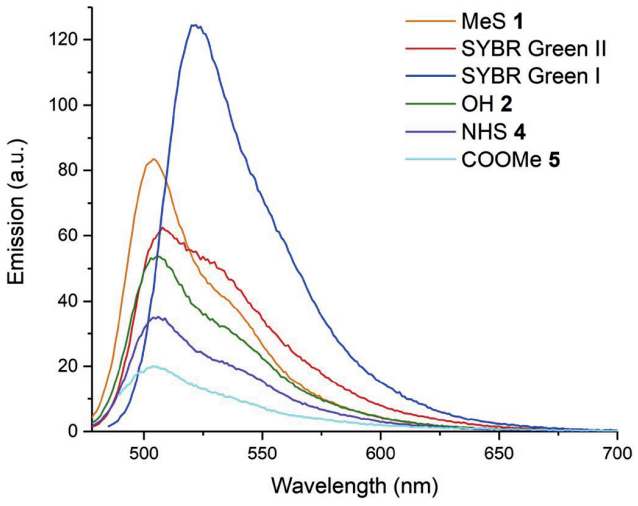

Fig. 5. Fluorescence spectra of the tested cyanine dyes measured in TE buffer with 0.52 μM ctDNA at 21 °C. A 1:200 000 dilution from each stock was made corresponding 0.1 μM concentration except for COOMe **5** 1.0 μM was used.

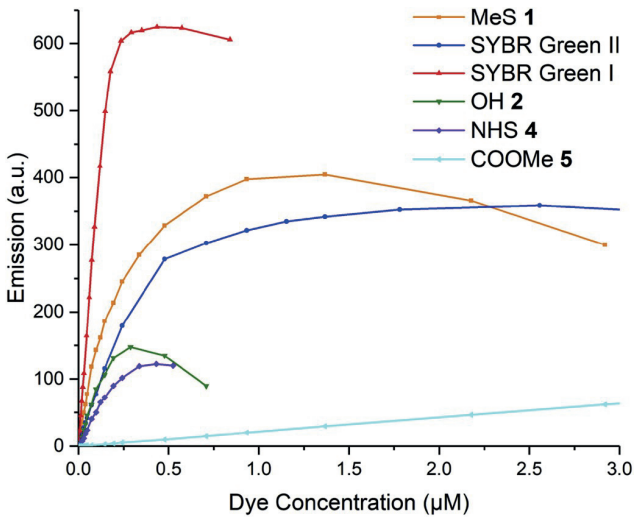

Fig. 6. Binding isotherms from titrations of different dyes in 0.52 μM ctDNA in TE buffer at 21 °C.

Table 2
Summarized ctDNA binding parameters attained from fluorescence spectroscopy titrations. Fluorescence quantum yields were derived from Fig. S28.

Dye	Binding constant K_a (10^6 M^{-1})	Binding site size n (bp)	Gibbs free energy ΔG (kJ/mol)	Fluorescence quantum yield Φ
MeS **1**	3.9 ± 0.1	2.2 ± 0.03	−37	0.60
SYBR Green II	15 ± 2	2.8 ± 0.5	−40	0.36 [25]
SYBR Green I	5.9 ± 0.05	3.2 ± 0.11	−38	0.80 [26]
OH **2**	2.8 ± 0.4	3.4 ± 0.3	−36	0.47
NHS **4**	1.3 ± 0.06	3.2 ± 0.15	−34	0.63

Using θ it is possible to determine the concentration of free molecules in solution (L) according to equation (4)

$$L = (1 - \theta)c \tag{4}$$

and binding density (v) of bound dye molecules

$$v = \theta c/c_{DNA}, \tag{5}$$

where c is the concentration of the dye and c_{DNA} is the concentration of the nucleic acid in solution. Processing the generated data according to equations (3)–(5) gives the Scatchard plots shown in Fig. 7, Fig. S24 and S25, where a fit to equation (1) was done in order to get the binding constant and the binding site size for individual dye molecules expressed in base pairs. The data for ctDNA from this procedure is summarized in Table 2.

The binding affinity seems to increase as the arm moiety on the molecules gets longer, suggesting a positive effect of hydrophobic interactions between the nucleic acid groove and the dye arm in binding with λDNA (Table S4). However, as can be seen in Fig. 8, this also causes an increase in the size demanded by an individual molecule. The fit done on known values for different dyes indicates a linear dependence between binding site size and the arm length. The outlier in the series, OH **2** is the only molecule with an extended, completely linear 2-substituent and because of this, might be able to insert more completely to the dsDNA lattice. The results of binding site size acquired from ctDNA and λDNA are highly similar for the dyes with shorter "arm" lengths, but discrepancies appear for OH **2** and NHS **4**. Reasons for the better accommodation of long-armed dyes with λDNA could be better uniformity and more continuous dsDNA lattice, whereas ctDNA constitutes of a size distribution of dsDNA oligomers (and ssDNA as a side product). The effect is even more pronounced with hpDNA (Table S4), where unrealistic results are acquired because the theory does not account for the finite length of the dsDNA.

The positively charged dimethyl amine groups seem to contribute positively to the binding affinity, as evidenced by significantly higher association constants for SYBR Green I and SYBR Green II. The hydroxyl (OH **2**) and carboxylic acid (COOH **3** and COOMe **5**) groups on the other hand carry a negative partial charge, which could affect the groove binding negatively. An indication of this was given by the lower binding affinity of OH **2** compared to SYBR Green I despite its longer arm moiety, but a clear relationship cannot be established. The carboxylic acid functionalized dye **3** posed significant problems considering the sample purity and heavy aggregation in solution and hence the titration experiments were not successful. The fluorescence of the COOMe-functionalized compound **5** varied linearly with concentration throughout the titration, making determination of the binding constants impossible in the attempted concentration regime. The highest obtained fluorescence intensities for each dye with each nucleic acid are presented in Fig. 9.

The fluorescence quantum yield for MeS dye **1** when bound to ctDNA is 60%, which is comparable to the value of 54% given for SYBR Green II with RNA [25]. The corresponding value for SYBR Green II when bound to ctDNA is 36%. SYBR Green I, on the other hand, shows a higher quantum yield of 80% when bound to ctDNA and combined with its higher molar absorptivity, meaning that the thiazole chromophore with a N-linked arm moiety is brighter of the two [26]. The reason for the lower fluorescence saturation of SYBR Green I with rRNA compared to MeS **1** is most likely due to limitations in the number of binding sites available, as each molecule requires a longer stretch of double-stranded nucleic acid for binding. For SYBR Green II, the difference in fluorescence saturation intensity with rRNA should be a result of different binding site size, as the chromophores are the same in both molecules. Thus, the quality of a nucleic acid binding fluorophore is determined by two factors. First, the brightness of the bound chromophore plays a crucial role but, equally important are the parameters affiliated with the binding. With a longer arm on the molecule, the strength of binding

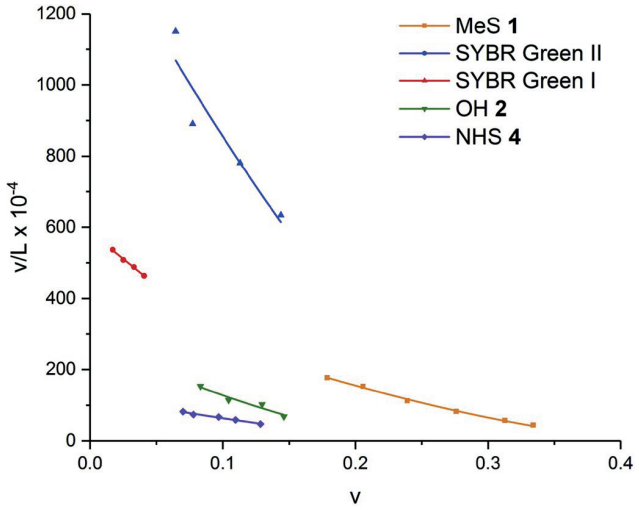

Fig. 7. Scatchard plot for cyanine dyes binding to ctDNA based on the data from Fig. 6 and Fig. S23 and fitting based on McGhee von Hippel equation (1).

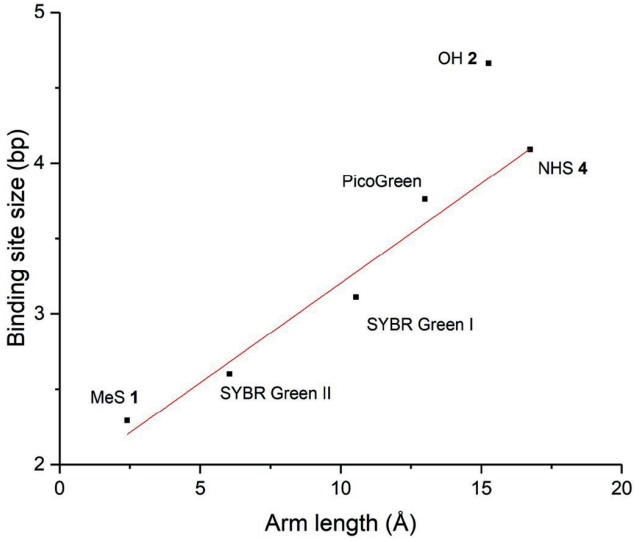

Fig. 8. Relationship between the length of the arm moiety on a molecule and corresponding binding site size in binding to λDNA (Table S4).

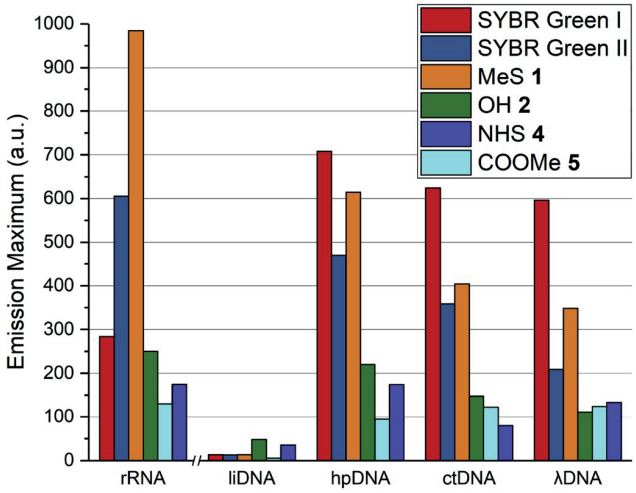

Fig. 9. Highest fluorescence values achieved from titrations with different nucleic acids. All the DNA samples were measured using the same settings on the spectrophotometer. All samples were measured in constant nucleic acid concentration in TE buffer at 21 °C and aliquots of respective dye were added until highest value of emission was reached. rRNA = cellular RNA, liDNA = 50 base linear ssDNA, hpDNA = 50 base self-pairing DNA, ctDNA = calf thymus DNA and λDNA = bacterial GLP-GPI plasmid DNA.

increases but in turn so does the size of the binding site. However, packing the probes too tightly on the double-stranded nucleic acids leads to homo-quenching between dye molecules. This means a careful balance exists between maximizing the number of probes bound to a nucleic acid without inducing such proximity between individual probes that leads to quenching. With this information, rational design can be used to synthesize probes that bind to nucleic acids with high affinity, such as SYBR Green I, or probes with slightly lower affinity but higher brightness as an effect of increased number of molecules bound to the target at maximum load, such as MeS **1**.

As the structures show, the differences between SYBR Green I and SYBR Green II are found in the different hetero atom on the 2-quinoline and 3-indole positions together with the linking arm of the molecules. Surprisingly, for our synthesized dyes, this leads to a significant decrease in the brightness of the chromophore, with the molar absorptivity decreasing by almost a half and the fluorescence quantum yield by 10%–20% compared to SYBR Green I. For the molecules synthesized in this work, this leads to a brightness that is ~40% of that of SYBR Green I. Although the chromophore of SYBR Green I has a higher brightness in nucleic acid contexts, the emission intensity of SYBR Green II is higher, when binding to rRNA. Importantly, compound **1** reaches even higher intensity when associating to rRNA. This can be explained by the characteristics of the complex formation across different dyes and especially the sizes of the binding site, (n) as shown in Table 2. While a single molecule of SYBR Green I occupies (in average) 3.1 base pairs on the dsDNA lattice, the length of lattice required by SYBR Green II and MeS dye **1** is only 2.8 and 2.2 base pairs, respectively. With lower available binding sites for the dyes, MeS **1** is the better nucleic acid probe as it makes better use of the limited binding sites. As proposed by the group of Geddes [16,17] the higher binding affinity comes as an effect of the arm moiety as the alkyl chains settle along the groove. This is something that we also observed here from the high binding constant value of compounds **2** and **4** with λDNA. Additionally, the cationic charge of the dimethylamine group in the arm of SYBR Green I and SYBR Green II adds an electrostatic component to the interaction and also increases the water solubility of the dyes. The synthesized products carry only one positive charge, which is insufficient for solubilizing the compounds and thus results in aggregation in aqueous solutions, as observed by scattering and aggregation in UV–vis absorption. This should be taken into account in future work by either replacing the arm with a more hydrophilic molecule, such as ethyl glycol, or increasing the charge of the chromophore. Despite the drawbacks in solubility and increased binding site size, the biofunctionalized dyes **2** and **4** are still potent fluorophores. To show this, we evaluated the use of MeS **1** and NHS **4** in *in vitro* experiments on a viral genomic sample, Echovirus 1 RNA, as shown in the following section.

2.3. Case study: echovirus 1 genomic RNA

Viral RNA, as well as cellular RNA, typically forms secondary structures, which is the basis of fluorescence emission upon binding of the dyes synthesized in this work. Presently, there are very few RNA/DNA detecting molecules that could be used to detect viral genome release in cellular vesicles. Therefore, in this study, we aimed at developing RNA binding dyes that can be targeted to cellular vesicles by conjugating to carrier materials that are internalized to vesicles.

In order to prove that MeS **1** is able to detect viral RNA, we first tested the compound with a conventional method to detect RNA released from enterovirus echovirus 1 particles, namely a PaSTRy assay [27]. In this method, the viral genome is released from its capsid by gradually increasing the temperature to 90 °C. Melting temperature is measured to describe the stability of the virus and, for example, to test if drugs stabilize or destabilize the viruses. In the melting curve of virus particles, upon opening of the virus the emission values rapidly rose until about 60 °C, due to the release of viral RNA followed from capsid opening, after which the emission values then started to decrease again, as the rising temperature dissociates the dye-nucleic acid complex (Fig. 10). In the measurement, the emission of MeS **1** was significantly higher compared to that of SYBR Green II. This result further supports the observation that MeS **1** provides higher emission intensities compared to SYBR Green II (with sufficiently adjusted concentration). While the improvement in fluorescence intensity with MeS **1** in comparison to SYBR Green II was highly desirable, our initial objective was to develop a similar dye with potential for covalent attachment. To examine the potential of using NHS **4** as such a probe to sense RNA release from the virus capsid, the dye was conjugated to the free lysine residues found on EV1 capsid (see SI for details). NHS **4** conjugated on the echovirus 1 capsid surface gave an observable fluorescence peak (Fig. 10), despite being only a fraction in intensity compared to MeS **1**. Such a result was expected because less molecules are present on the

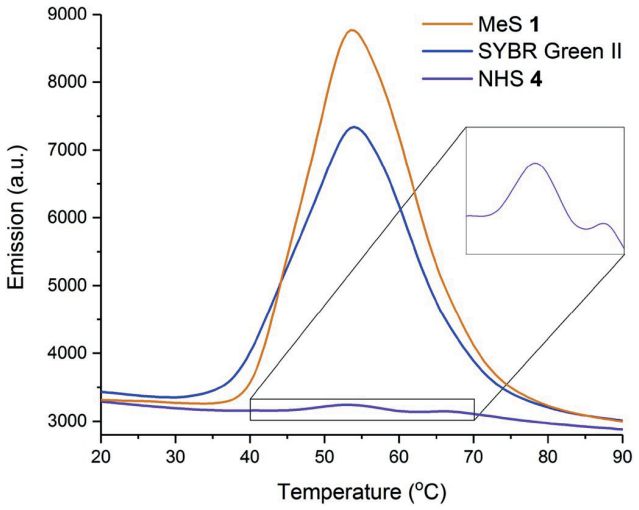

Fig. 10. Thermal assay melting curve of EV1 monitored with SYBR Green II, MeS **1**, as well as NHS **4**-conjugated virus particles. Inset: Magnification of the emission trace of **4**. (For interpretation of the references to color in this figure legend, the reader is referred to the Web version of this article.)

capsid surface compared to dye **1** that is free in solution. However, the long alkyl chain on **4** might contribute to weaker binding in higher temperature as well.

Next, we tested how our compounds detect viral RNA at physiological temperature in a real-time assay that was previously established in our laboratory [28]. Virus, nucleic acid probes and salt solution, that forces opening of the virus particles, were mixed together at 37 °C and fluorescence emission was followed for 3 h in a 96-well plate setup in a spectrofluorometer (Fig. 11). The results showed that the MeS **1** emission increased within 30 min to high values, due to addition of the opening buffer. Similarly, we tested NHS **4** which was directly conjugated to the virus capsid, thus being very close to the RNA in the event of RNA release. NHS **4** conjugated to the virus understandably showed much lower intensities but still detected virus opening at 37 °C. Thus, the two newly synthesized dyes MeS **1** and NHS **4** demonstrated their usability in nucleic acid sensing. While MeS **1** gave a good signal in the experiment, the values of NHS **4** conjugated on the viral particle surface were only 20% that of the former (Fig. 11). This was an expected result, as the amount of dye **4** molecules bound on the viral capsid surface is significantly lower compared to concentration of MeS **1** in solution. Interestingly, at around 20 min the emission of NHS **4** peaked in fluorescence before plateauing to 80% of the peak emission intensity, possibly indicating the moment where majority of the viral RNA is released from the viral particles before diffusing to the total sample volume. While the emission intensity of NHS **4** is lower *in vitro* compared to MeS **1**, it should be noted that the conjugation to the viral capsid means the emission is better localized.

As MeS **1** binding was based on binding to double stranded nucleic acid, we next tested whether we could quantify the portion of RNA that is in double-stranded conformation. Previously, many calculation-based estimations about secondary structures in viral RNA genomes have been made [29,30], but to our best knowledge no empirical studies on the degree of RNA duplex in the viral context have been made before. A method monitor the single-to-double-stranded RNA ratio in solution using PicoGreen has been previously reported [31,32]. However, our method aimed to utilize total fluorescence intensity instead of specific wavelengths or fluorescence lifetimes as the variable.

To evaluate this approach, a 50 base ssRNA template was mixed with excess amount of complementary ssRNA of varying length (15, 30 and 45 bases) and annealing was carried out to achieve base-pairing. Measuring the fluorescence from these samples with SYBR Green I, SYBR Green II, and MeS **1** present, gave four measurement points for each dye-RNA combination, as shown in Fig. 12. While neither of the

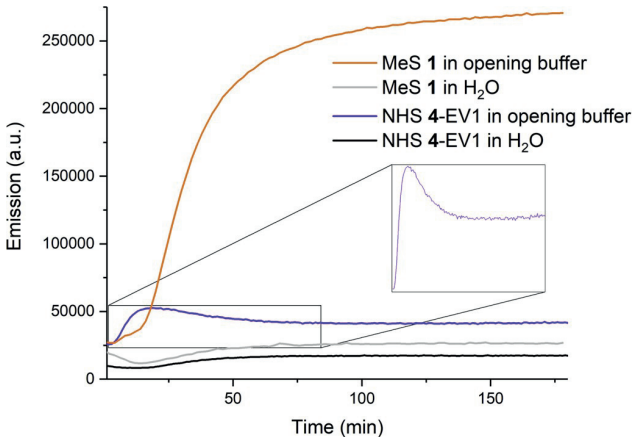

Fig. 11. Emission of MeS **1** and NHS **4**-conjugated EV1 capsid in water and buffer solution (20 mM NaCl, 6 mM KH_2PO_4, 12 mM K_2HPO_4, pH ~7.2) promoting capsid opening for the EV1 at 37 °C. Inset: Magnification of the Y-axis to display NHS **4** curve better.

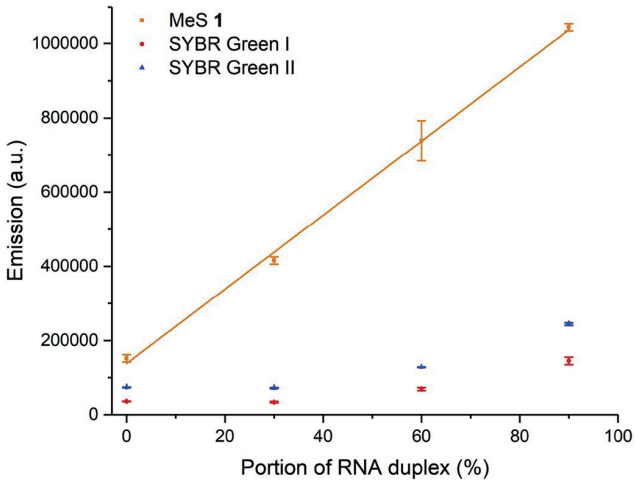

Fig. 12. MeS **1**, SYBR Green I, and SYBR Green II mixed with RNA constructs having varying amounts of double-strand. A 50-mer ssRNA was mixed with equimolar amounts of complementary ssRNA with lengths 15, 30, and 45 bases, respectively. Also shown is a linear fit for compound **1**. Measurements were performed in triplicates at room temperature (21 °C) in water. (For interpretation of the references to color in this figure legend, the reader is referred to the Web version of this article.)

SYBR Green dyes exhibited a linear dependence on RNA duplex, it was possible to construct a linear calibration curve for the MeS **1**. To further test this in practice, we attempted to determine the fraction of double-stranded RNA in released enterovirus EV1 RNA genome. As before, the virus opening was induced by adjusting the salt concentrations and increasing the temperature to 37 °C [28] allowing dyes to intercalate into the viral RNA. After preparing a calibration curve for MeS **1** in the capsid opening conditions, an EV1 sample containing equal amounts of RNA and dye (as applied to construct the calibration curve) was measured over the course of 180 min (Fig. S29). From this, the highest attained emission value was compared to the calibration curve (Fig. 13). This result corresponds to 51% of the viral RNA is in duplex form, which supports previous estimations stating that the viral RNA is expected to have large secondary structures [29,30].

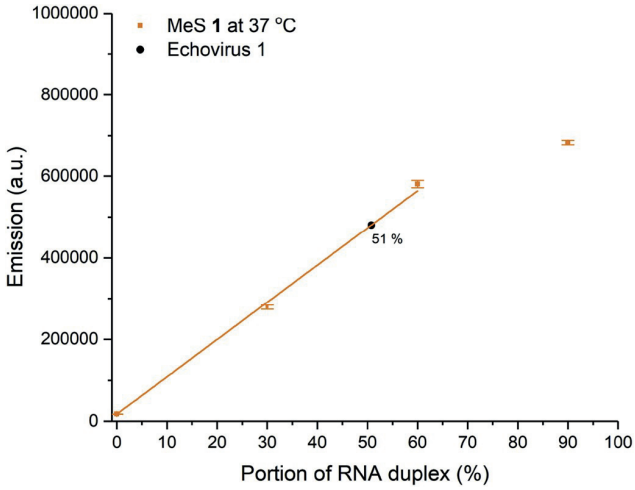

Fig. 13. MeS **1** measured with partially double-stranded RNA oligomers. The emission value from a sample of EV1 containing equal concentration of RNA and MeS **1** (Fig. S29) was inserted to the linear fit to yield the fraction of duplex RNA found in the sample. Measurements were performed in triplicates at 37 °C in 20 mM NaCl, 6 mM KH_2PO_4, 12 mM K_2HPO_4.

As an effect of the increased temperature and/or salt concentrations, the linearity of the calibration curve does not hold with the 45-mer sample, which underlines the importance of careful parametrization of the experiment for achieving reliable results throughout the full range of duplex formation. By increasing the amount of MeS **1** in experiments, the overall emission intensity can be increased to higher values compared to those attainable with SYBR Green II. Additionally, MeS **1** dye is more accommodating in this regard, because of its combined binding site size requirement and affinity for nucleic acid binding, as described in the previous section. Admittedly, similar results could be achieved with SYBR Green I and SYBR Green II, but the lower binding affinity and binding site size make MeS **1** a more universal choice, due to increased ease in adjusting concentrations in the experiments to achieve linearity. With such a calibration curve, the single-to-double-stranded RNA ratio of an unknown sample of equal mass of RNA can be determined. In this work, viral RNA of EV1 was used as an example. Information regarding the state of secondary structure of ssRNA should provide useful insight for the continuously increasing number of studies on RNA.

In conclusion, the two newly synthesized dyes MeS **1** and NHS **4** expand the potential of nucleic acid sensing with SYBR Green related cyanine dyes in two very different ways. While MeS **1** can be used to increase fluorescence emission intensity with RNA samples, its linear response to changes in portion of double-stranded RNA offers an enhanced application as shown above. NHS **4** on the other hand offers new possibilities for better targeting, as shown above by covalently linking the dye on a viral capsid surface. Similar click chemistry can be applied to any primary amine group from antibodies to nanoparticles, opening countless possibilities for refined nucleic acid sensing.

3. Conclusion

The successful crystallization of SYBR Green II led to elucidation of the previously unknown structural characteristics of this well-established RNA marker. Knowledge of the structure of the indole-quinolinium-based cyanine dye enabled us to design a synthesis protocol to easily produce other 2-thiol substituted cyanine dyes at an analytical scale. This procedure was then employed to synthesize dyes **1**–**5** with varying 2-substituents, with the aim to add the potential of post-synthetic conjugation to *e.g.* antibodies or solid support.

The synthesized MeS **1** provides the highest fluorescence intensity when bound to nucleic acids and, importantly, higher in comparison to SYBR Green II, whereas compounds **2**–**5** gave lower values. Detailed studies between the synthesized and commercial dyes suggest that all the compounds are sensitive for nucleic acid sensing but MeS **1** as the smallest molecule takes less space in binding leading to higher overall emission compared to SYBR Green II. This is because the increasing size of the 2-substituent makes single molecules occupy more space on the nucleic acid strand and hence fewer molecules saturate the binding area available, leading to decreased fluorescence. These results offer fundamental understanding on the effects that different substituents might have on such intercalators. Regardless, all the synthesized dyes **1**–**5** exhibited considerable brightness.

Importantly, we could show with viral RNA samples that the produced dyes can sensitively detect RNA in biologically relevant assays. The dyes detected virus opening and RNA release *in vitro*: both unconjugated and a functionalized dye conjugated directly to viral particles detected virus opening in our developed real-time assay. This promises that in the future the conjugated dyes can be used to detect uncoating in cellular vesicles *in situ*. Similarly, the NHS-functionalized compound **4** can readily be employed for conjugation to any primary amine, providing added function for detection of nucleic acids with this class of fluorophores. Furthermore, the hydroxyl- and carboxylic acid functionalized dyes **2** and **3** can readily be employed to conjugate these dyes to a solid support or a biomolecule using carbodiimide crosslinking chemistry and thereby preventing dilution effects such as diffusion through cell membranes. Although the brightness of these dyes (**2**–**5**) is lower due to their longer 2-substituents, these functional groups offer the possibility of a localized, non-diffusing source of fluorescence, which can be an attractive option for various microscopy imaging applications.

4. Experimental section

All reagents are commercially available and used as received unless otherwise mentioned. 1,2-dichloroethane (DCE) was distilled over $CaCl_2$ and stored under nitrogen over 3 Å molecular sieves. K_2CO_3 was dried in an oven at 120 °C and stored in a desiccator. SYBR Green I and II were purchased from Invitrogen as a solution in DMSO. Double-stranded bacterial plasmid λDNA (GLP-GPI 0.52 μg/μl) was received from ETH Zurich. Calf thymus (ct) DNA was purchased from Sigma-Aldrich. The 50 base long, single stranded DNAs were purchased from TAG Copenhagen A/S (Fredriksberg, Denmark) with sequences 5′-ACC AAA CTC AAC ACA CGA ACC CAA CGT TGG GTT CGT GTG TTG AGT TTG GT-3′ (hairpin DNA, hpDNA) and 5′-ACC CAC ACA ACC ACA AAC CAC ACC CAA CCC AAA CCC ACA CAC CCA ACA AC-3′ (linear DNA, liDNA) designed to promote hairpin and linear conformation of the oligomers, respectively. Both oligomers were dissolved in ddH_2O and the hpDNA was heated in boiling water bath for 3 min and allowed to cool down prior to use. Single stranded RNA oligomers were purchased from Eurofins Genomics (Ebersberg, Germany) as a 50 base template with sequence 5′-CCC AAC ACA ACC ACC AAC CAC AAA CAA CCC AAA CCC ACA CCA ACA ACA AAC-3′ and three complementary U/G strands of 15, 30 and 45 bases in length from the 3′ end (5′-UGU UGG UGU GGG UUU GGG UUG UUU GUG GUU GGU GGU UGU GUU GGG-3′). Cellular RNA (rRNA) was harvested from adenocarcinomic human alveolar basal epithelial cells (A549). The extraction was conducted using High Pure Viral RNA kit from Roche (Indianapolis, USA) following the instructions provided by the manufacturer. The concentration and purity of the extracted RNA was measured using Thermo Scientific NanoDrop One UV–vis spectrophotometer.

^{1}H, ^{13}C and 2D NMR (HSQC and HMBC) spectra were recorded with Bruker Avance 500 MHz and Bruker Avance 300 MHz spectrometers and chemical shifts were calibrated to the residual proton or carbon resonance of the solvent. Accurate HRMS spectra were measured with Micromass LCT ESI-TOF mass spectrometer using Leucine Enkephalin as the internal calibration. Atomic coordinates and structure factors for the reported crystal structures have been deposited with the Cambridge Crystallographic Data Centre (CCDC) under accession numbers 1482404 (SYBR Green II) and 1482405 (MeS **1**).

For comprehensive synthetic and experimental details please see the Supporting Information.

CRediT authorship contribution statement

Ville K. Saarnio: Writing - original draft, Data curation, Formal analysis, Investigation. **Kirsi Salorinne:** Formal analysis, Investigation. **Visa P. Ruokolainen:** Writing - original draft, Data curation, Formal analysis, Investigation. **Jesper R. Nilsson:** Data curation, Formal analysis, Investigation, Writing - original draft. **Tiia-Riikka Tero:** Data curation, Formal analysis, Investigation. **Sami Oikarinen:** Formal analysis. **L. Marcus Wilhelmsson:** Writing - original draft, Funding acquisition. **Tanja M. Lahtinen:** Writing - original draft, Formal analysis. **Varpu S. Marjomäki:** Writing - original draft, Funding acquisition, Project administration.

Acknowledgements

This work was supported by the Academy of Finland [266492 to T.-R.T and V.S., and 257125 to V.M.]; Jane and Aatos Erkko Foundation [Novel probes for discovering anti-virals to V.S., T.L., and V.M.]; and the Swedish Foundation for Strategic Research [IRC15-0065 for J.R.N., and L.M.W.]. GLP-GPI plasmid was obtained as a kind gift from Lucas

Pelkmans from ETH Zurich.

Appendix A. Supplementary data

Supplementary data to this article can be found online at https://doi.org/10.1016/j.dyepig.2020.108282.

References

[1] Bruce A. Armitage. Cyanine dye–nucleic acid interactions. In: Strekowski L, editor. Top. Heterocycl. Chem.. fourteenth ed. Pittsburgh: Springer; 2008. p. 11–29. https://doi.org/10.1007/7081_2007_109.

[2] Mojzych M, Maged H. Synthesis of cyanine dyes. Top. Heterocycl. Chem.. Springer; 2008. p. 1–9.

[3] Shindy HA. Fundamentals in the chemistry of cyanine dyes: a review. Dyes Pigments 2017;145:505–13. https://doi.org/10.1016/j.dyepig.2017.06.029.

[4] Choyke PL, Alford R, Simpson HM, Duberman J, Craig Hill G, Ogawa M, et al. Toxicity of organic fluorophores used in molecular imaging: literature review. Mol Imag 2009;8:341–54. https://doi.org/10.2310/7290.2009.00031.

[5] Lee LG, Chen C, Chiu LA. Thiazole orange: a new dye for reticulocyte analysis. Cytometry 1986;7:508–17. https://doi.org/10.1002/cyto.990070603.

[6] Vasilev AA, Kandinska MI, Stoyanov SS, Yordanova SB, Sucunza D, Vaquero JJ, et al. Halogen-containing thiazole orange analogues - new fluorogenic DNA stains. Beilstein J Org Chem 2017;13:2902–14. https://doi.org/10.3762/bjoc.13.283.

[7] Guo RJ, Yan JW, Chen S Bin, Gu LQ, Huang ZS, Tan JH. A simple structural modification to thiazole orange to improve the selective detection of G-quadruplexes. Dyes Pigments 2016;126:76–85. https://doi.org/10.1016/j.dyepig.2015.11.010.

[8] Karlsson HJ, Bergqvist MH, Lincoln P, Westman G. Syntheses and DNA-binding studies of a series of unsymmetrical cyanine dyes: structural influence on the degree of minor groove binding to natural DNA. Bioorg Med Chem 2004;12:2369–84. https://doi.org/10.1016/j.bmc.2004.02.006.

[9] Deligeorgiev TG, Gadjev NI, Vasilev AA, Maximova VA, Timcheva II, Katerinopoulos HE, et al. Synthesis and properties of novel asymmetric monomethine cyanine dyes as non-covalent labels for nucleic acids. Dyes Pigments 2007;75:466–73. https://doi.org/10.1016/j.dyepig.2006.06.023.

[10] Shank NI, Pham HH, Waggoner AS, Armitage BA. Twisted cyanines: a non-planar fluorogenic dye with superior photostability and its use in a protein-based fluoromodule. J Am Chem Soc 2013;135:242–51. https://doi.org/10.1021/ja308629w.

[11] Invitrogen. The molecular probes handbook: a guide to fluorescent probes and labeling technologies. Life Technologies Corporation; 2010.

[12] Zipper H, Brunner H, Bernhagen J, Vitzthum F. Investigations on DNA intercalation and surface binding by SYBR Green I, its structure determination and methodological implications. Nucleic Acids Res 2004;32:e103. https://doi.org/10.1093/nar/gnh101.

[13] Evenson WE, Boden LM, Muzikar KA, Oleary DJ. 1H and 13C NMR assignments for the cyanine dyes SYBR safe and thiazole orange. J Org Chem 2012;77:10967–71. https://doi.org/10.1021/jo3021659.

[14] Ihmels H, Otto D. Intercalation of Organic dye molecules into double-stranded DNA - general principles and recent developments. Top Curr Chem 2005;258:161–204. https://doi.org/10.1007/b135804.

[15] Karunakaran V, Pérez Lustres JL, Zhao L, Ernsting NP, Seitz O. Large dynamic Stokes shift of DNA intercalation dye Thiazole Orange has contribution from a high-frequency mode. J Am Chem Soc 2006;128:2954–62. https://doi.org/10.1021/ja056862n.

[16] Dragan AI, Casas-Finet JR, Bishop ES, Strouse RJ, Schenerman MA, Geddes CD. Characterization of PicoGreen interaction with dsDNA and the origin of its fluorescence enhancement upon binding. Biophys J 2010;99:3010–9. https://doi.org/10.1016/j.bpj.2010.09.012.

[17] Geddes CD, Dragan AI, Casas-Finet JR, Schenerman MA, McGivney JB, Strouse RJ, et al. SYBR green I: fluorescence properties and interaction with DNA. J Fluoresc 2012;22:1189–99. https://doi.org/10.1007/s10895-012-1059-8.

[18] Fei X, Gu Y. Progress in modifications and applications of fluorescent dye probe. Prog Nat Sci 2009;19:1–7. https://doi.org/10.1016/j.pnsc.2008.06.004.

[19] Jin X, Yue S, Singer VL, Jones LJ, Beaudet MP, Cheung C-Y, et al. Characterization of SYBR Gold nucleic acid gel stain: a dye optimized for use with 300-nm ultraviolet transilluminators. Anal Biochem 2003;288:278–88. https://doi.org/10.1006/abio.1998.3067.

[20] Crnolatac I, Rogan I, Majić B, Tomić S, Deligeorgiev T, Horvat G, et al. Small molecule probes finely differentiate between various ds- and ss-DNA and RNA by fluorescence, CD and NMR response. Anal Chim Acta 2016;940:128–35. https://doi.org/10.1016/j.aca.2016.08.021.

[21] Das AK, Ihmels H, Kölsch S. Diphenylaminostyryl-substituted quinolizinium derivatives as fluorescent light-up probes for duplex and quadruplex DNA. Photochem Photobiol Sci 2019;18:1373–81. https://doi.org/10.1039/c9pp00096h.

[22] Ying L. Nucleic acid detections and methods of their use. 2013. 2013/0137875.

[23] Neises B, Steglich W. Simple method for the esterification of carboxylic acids. Angew Chem Int Ed 1978;17:522–4.

[24] McGhee JD, von Hippel PH. Theoretical aspects of DNA-protein interactions: Co-operative and non-co-operative binding of large ligands to a one-dimensional homogeneous lattice. J Mol Biol 1974;86:469–89. https://doi.org/10.1016/0022-2836(74)90031-X.

[25] Molecular probes. SYBR ® green II RNA gel stain product information sheet, vols. 1–3; 2001.

[26] Invitrogen. SYBR ® green I nucleic acid gel stain product information sheet, vols. 1–5; 2006.

[27] Martikainen M, Salorinne K, Lahtinen T, Malola S, Permi P, Häkkinen H, et al. Hydrophobic pocket targeting probes for enteroviruses. Nanoscale 2015:17457–67. https://doi.org/10.1039/c5nr04139b.

[28] Ruokolainen V, Domanska A, Laajala M, Pelliccia M, Butcher SJ, Marjomäki V. Extracellular albumin and endosomal ions prime enterovirus particles for uncoating that can be prevented by fatty acid saturation. J Virol 2019. https://doi.org/10.1128/jvi.00599-19.

[29] Simmonds P, Tuplin A, Evans DJ. Detection of genome-scale ordered RNA structure (GORS) in genomes of positive-stranded RNA viruses: implications for virus-evolution and host persistence. Bioinformatics 2004;10:1337–51. https://doi.org/10.1261/rna.7640104.

[30] Davis M, Sagan SM, Pezacki JP, Evans DJ, Simmonds P. Bioinformatic and physical characterizations of genome-scale ordered RNA structure in Mammalian RNA viruses. J Virol 2008;82:11824–36. https://doi.org/10.1128/jvi.01078-08.

[31] Cosa G, Focsaneanu KS, McLean JRN, Scaiano JC. Direct determination of single-to-double stranded DNA ratio in solution applying time-resolved fluorescence measurements of dye-DNA complexes. Chem Commun 2000;8:689–90. https://doi.org/10.1039/b000473l.

[32] Beach L, Schweitzer C, Scaiano JC. Direct determination of single-to-double stranded DNA ratio in solution using steady-state fluorescence measurements. Org Biomol Chem 2003;1:450–1. https://doi.org/10.1039/b209284k.